Atoms in the lowest Landau level of a synthetic erbium quantum Hall system

Dissertation
zur
Erlangung des Doktorgrades (Dr. rer. nat.)
der
Mathematisch-Naturwissenschaftlichen Fakultät
der
Rheinischen Friedrich-Wilhelms-Universität Bonn

von
Roberto Vittorio Röll
aus
Solingen

Bonn, 2022

Angefertigt mit Genehmigung der Mathematisch-Naturwissenschaftlichen Fakultät der Rheinischen Friedrich-Wilhelms-Universität Bonn

1. Gutachter: Prof. Dr. Martin Weitz
2. Gutachter: Prof. Dr. Simon Stellmer

Tag der Promotion: 20.10.2022
Erscheinungsjahr: 2022

Contents

1 Introduction **3**

2 Properties of atomic erbium **7**

2.1 Electronic ground state . . . 8
  2.1.1 Zeeman splitting . . . 9
2.2 Relevant transitions . . . 9

3 Bose-Einstein condensation of erbium atoms **11**

3.1 Overview of the experimental apparatus . . . 12
  3.1.1 Effusion cell . . . 12
  3.1.2 Pre-cooling . . . 13
  3.1.3 Main chamber . . . 14
  3.1.4 Magnetic field coils . . . 14
  3.1.5 Magneto-optical trap . . . 15
  3.1.6 Optical-dipole trap . . . 16
  3.1.7 Absorption imaging . . . 17
3.2 Bose-Einstein condensation . . . 18

4 Electrons in magnetic fields - the Hall effect **21**

4.1 Classical Hall effect . . . 21
4.2 Landau Gauge . . . 23
  4.2.1 Degeneracy . . . 24
4.3 Quantum Hall effect . . . 24
  4.3.1 The velocity of the electrons . . . 26
  4.3.2 Edge effects . . . 26
  4.3.3 Local Chern Marker . . . 27

5 Artificial gauge fields with ultracold atoms **31**

5.1 Spin-orbit coupling . . . 32
  5.1.1 Artificial gauge fields - Synthetic dimensions . . . 33
  5.1.2 Spin-orbit coupling for erbium atoms . . . 33
5.2 From SOC to artificial Landau levels with erbium . . . 37
5.3 Dispersion relations . . . 39
  5.3.1 Edge - Bulk border . . . 43
5.4 Synthetic Hall mobility . . . 44
5.5 Local Chern marker of the synthetic system . . . 45

6 Experimental realisation of artificial gauge fields with ultracold erbium atoms 47
6.1 841 nm Laser setup 47
6.2 Optical Raman Setup at vacuum chamber 47
6.3 841 nm - Transition 48
  6.3.1 Spectroscopy 48
  6.3.2 Frequency stabilisation of the Titan:Saphir laser 50
  6.3.3 Magnetic field 52
6.4 Sample preparation 52
6.5 Effective coupling strength 53
6.6 Dispersion relations - Group velocities 54
  6.6.1 Experimental procedure 54
  6.6.2 Velocity measurements 59
6.7 Cyclotron Orbits 63
6.8 Synthetic Hall mobility 67
6.9 Local Chern Marker 68
6.10 Chiral edge currents 69

7 Conclusion and outlook 73

A Spin orbit coupled Hamiltonian for erbium 75

B Uncoupled atomic dispersion relation 81

C Velocity filter 83

Bibliography 85

Abstract

This thesis presents results on an experimental realisation of a synthetic Landau like system using ultracold erbium atoms in a two-dimensional quantum Hall ribbon geometry. The scheme used to realise artificial magnetic fields is based on spin-orbit coupling and uses a synthetic dimension encoded in the 13 internal Zeeman states of the erbium atom in its electronic ground state. The spin-orbit coupling is realised by two-photon Raman transitions and effectively creates unique pairs between the internal Zeeman state of atoms and its external momentum state. Therefore the atom's momentum is bound to a specific position in the synthetic dimension and the spin-orbit coupling can be interpreted as a vector potential in the Hamiltonian. The spatial dependence of the vector potential required to generate artificial magnetic fields is realised by the momentum dependence of the position in the synthetic dimension, or in other words the internal Zeeman state.

The experimental apparatus is introduced and the main properties are presented. The creation of a Bose-Einstein condensate, which lies at the very heart of this experiment, is introduced. The main properties of the experiment are presented as well as characterising measurements.

The basic theory behind the quantum Hall effect for a two-dimensional electron gas subject to a perpendicular real magnetic field is introduced and characteristic observables are derived to create a basic understanding of the underlying physics before the transition to synthetic magnetic fields is introduced.

Spin-orbit coupling is introduced in its use within the scope of this thesis by presenting the underlying theory following earlier work where another atomic species, dysprosium, was used. The implemented scheme allows for a system which follows a Landau like dispersion relation with clear distinct behaviour for the inner bulk region and outer edge regions. The behaviour of the bulk and the edge mode indicates the non-trivial topology of the system. Measurements including dispersion relations and excitation into higher energy bands are performed and show the expected and distinct behaviour of atoms in the bulk and near the edges respectively. The equivalent to closed cyclotron orbits is observed inside the bulk region, whereas skipping orbits are observed for edge regions.

In addition to the observation of flat dispersion relations and cyclotron orbits the mobility and a local Chern marker are determined. It will be shown that the mobility of the synthetic system follows the behaviour of a real quantum Hall system. The local Chern marker is determined to have a value close to the value expected for a Landau system with infinite size in the bulk region. This shows that the synthetic dimension with its 13 positions is large enough to observe a clear difference between bulk and edge behaviour.

The last section presents first measurements of a chiral edge current in a system of the size, which is presented in this thesis.

CHAPTER 1

Introduction

Quantum Hall physics is at the core of research of matter with non-trivial topological order. The bulk of such systems have a non-vanishing Chern number, and in addition there are topological protected edge states. For two-dimensional electron gases in solid state systems subject to strong magnetic fields, both the integer and the fractional quantum Hall effect have been observed. To begin with the quantum Hall effect was first predicted in 1975 by T. Ando, Y. Matsumoto and Y. Uemura [1] and first observations were made in 1978 by Jun-ichi Wakabayashi and Shinji Kawaji [2]. Klaus von Klitzig discovered in 1980 that the quantisation of the integer quantum Hall effect is exact [3, 4], which awarded him the Nobel Prize in 1985. The Klitzing constant $R_K = h/e^2$, which corresponds to the quantisation of the integer quantum Hall effect, was used as definition for the electrical resistance Ohm. Hence, it was part of the SI unit system until it was redefined in 2019 [5]. The fractional quantum Hall effect, in which the resistivity takes certain fractional values of the Klitzing constant, was first discovered in 1982 by D. C. Tsui, H. L. Stoermer and A. C. Gossard [6]. R. B. Laughlin H. L. Stoermer and D. C. Tsui received the Nobel Prize in 1998 [7]. Whereas the Integer quantum Hall effect is well understood, some specific fractional numbers in the fractional quantum Hall effect still are not understood. Therefore, the field of quantum Hall physics is a growing topic since its discovery.

The underlying difference between the fractional and the integer quantum Hall effect is that in the former the electrons are interacting and underlie many body physics, whereas the interaction is suppressed in the latter. Investigating fractional quantum Hall physics with electrons in solid state systems is challenging due to the need for ultra clean two-dimensional samples and strong magnetic fields of tens of Tesla. To create magnetic fields of this order of magnitude, superconducting materials are required. Even high temperature superconductors need to be cooled by liquid nitrogen [8].

A different potential experimental system to observe fractional quantum Hall physics are ultracold atom systems. These weakly interacting systems are experimentally very well controlled, and in genereal allow for critical confrontations of theory prediction with experimental results. The recent rapid advances in ultracold atoms physics have their foundations in the realisation of the laser [9, 10] which opened the way to many experimental techniques, e.g. optical cooling, which is used today on a daily basis in many laboratories around the world. Optical cooling describes the process of atoms being slowed down by near resonant laser light and optical light fields allow to trap atoms. First realisations in the 1980s were rewarded with the Nobel Prize in 1997 for Steven Chu, Claude Cohen-Tannoudji, and William D. Phillips [11, 12]. With more elaborate cooling techniques including magneto-optical traps [13, 14] and optical-dipole traps which use the optical gradient force [15–18] temperatures in the sub-Kelvin regime were achieved and the era of cold atom system began. Decreasing temperatures allowed to create a degenerate quantum gas in its ground state known as Bose-Einstein condensate. Such a state can be described by a single macroscopic wave function. The first Bose-Einstein condensates were observed by two groups [19, 20] in 1995 and rewarded with the Nobel Prize in 2001 [21, 22]. A Bose-Einstein condensate describes a state of matter or photons in which the particles macroscopically occupy the ground state of the system. The underlying statistics of Bose-Einstein condensation was derived in 1924 from Satyendra Nath Bose who wrote a letter to Albert Einstein about this statistic. Einstein translated the letter from English to German and published it for Satyendra Nath Bose in 1924 [23]. Einstein extended the idea from initially only photons to bosons in general and published the theory of Bose-Einstein statistics [24]. The Bose-Einstein-statistics is not restricted to matter which led in 2010 to the first observation of a Bose-Einstein condensate out of light by our group [25, 26]. Bose-Einstein condensates are of great interest since the macroscopic occupation of the ground state can serve as starting point for a wide class of other investigations.

A highly active research area is the use of ultra cold atomic systems to mimic charged particles in strong magnetic fields and therefore explore quantum physics with non trivial topology, e.g. quantum Hall physics.

Here, the main obstacle is the lack of the Lorentz force due to the charge neutrality of atoms. Without the Lorentz force quantum Hall physics is non existent. Therefore, many experiments aim at creating a Lorentz like force for neutral atoms by creating artificial magnetic fields. Even though different approaches are proposed the underlying principle of all approaches aim at imprinting a non trivial phase on the atoms. This phase can then be identified with the Aharonov-Bohm phase. The Aharonov-Bohm phase is the phase acquired by a charged particle propagating through an electromagnetic vector potential. A phase is acquired even if both, magnetic and electric field, are zero for the particles position [27].

The probably most intuitive idea which has been realised is to stir a cloud of cold atoms [28–32]. The resulting Coriolis force can be interpreted as a Lorentz force. The force is directly proportional to the rotation frequency which is a well controllable parameter. However, the force is limited by the simple fact that for large rotational frequencies the atoms fly out of the trapping potential and are subject to additional heating. Hence, the magnitude of the effective artificial magnetic field is also restricted.

Another proposal is to directly imprint a non-trivial phase onto the atoms by moving the atoms through a two-dimensional optical lattice [33–36]. Atoms moving on a closed circle through the lattice acquire an effective phase, which is then interpreted as an Aharonov-Bohm phase. The realisation of artificial gauge fields for neutral atoms allowed to investigate Hofstadter physics in ultracold atomic system [37–41].

Two other schemes rely on the implementation of spin-orbit coupling, in which an external momentum state of the atoms is coupled to a specific internal Zeeman state. An electron in a magnetic field will have its dispersion relation modified. By introducing spin-orbit coupling the dispersion relation of the atoms is already different to the uncoupled free atoms. However, in order to create synthetic magnetic fields there need to be some spatial dependence. One way of realising the spatial dependence is by making the spin-orbit coupling strength position dependent by an external real magnetic field gradient. This has been successfully realised by the group of Ian Spielman with rubidium atoms [42]. Celi et al. proposed a different approach: The internal Zeeman state is interpreted as an effective position. The fixed momentum - Zeeman state pairs gives a position dependent momentum state [43].

In recent experimental work, integer quantum Hall physics has been realised in a two-dimensional system formed by one synthetic and one real space dimension, the former formed by the Zeeman levels of dysprosium atoms. The present thesis directly builds upon this work by Chalopin et al [44, 45].

In the experiments described in this thesis, integer quantum Hall physics based on synthetic dimensions is demonstrated with a different atomic system, atomic erbium, with the synthetic dimension encoded in the 13 Zeeman levels of the electronic ground state of this atoms. In a system with high a enough number of Zeeman levels to allow for distinct bulk and edge behaviour, a chiral edge current is experimentally observed.

The thesis basically contains two main parts. The first part, including chapter 2 and 3, introduces erbium and important properties are given. The routine to create a Bose-Einstein condensate is explained briefly and the needed experimental setups are introduced alongside. Having the underlying physical principles and the corresponding experimental setup together provides a basic but good understanding of the Bose-Einstein condensate preparation which is required for further measurements.

The second part of the thesis, starting with chapter 4, starts by giving an introduction of electrons in external magnetic fields. The presented theory is limited to the here relevant parts but external sources are given where appropriate. Naturally, the following chapter will give the underlying theory concerning the theory of how to create artificial magnetic fields for the in this thesis realised synthetic dimension approach. Chapter 5 also includes the mapping from the spin-orbit coupled system to the real quantum Hall system described in the Landau gauge.

The final chapter 6 starts by introducing and explaining the setup needed for spin-orbit coupling followed by a description of the experimental routine to prepare the Bose-Einstein condensate in a state which is suitable for the following experiments. The spin-orbit coupled system is characterised by velocity measurements for different effective coupling strengths. An equivalent to cyclotron orbits will be investigated to show the non trivial topology of the system. These measurements are underlined by mobility and local Chern marker measurements, the latter showing a clear quantum behaviour. Finally, a measurement of a chiral edge current is presented. The thesis concludes with an outlook.

CHAPTER 2

Properties of atomic erbium

Erbium is a rare earth element (atomic number 68, mass of 167.26 u) and part of the lanthanide atoms. It exists in 6 stable isotopes. Erbium was first mentioned in 1843 by C.G. Mosander who extracted erbium oxide from gadolinite [46]. The first pure erbium oxide was produced in 1934 by Heinrich Bommer and Wilhelm Klemm [47]. Nowadays erbium is often used in optical applications. Erbium doped fibre amplifiers are used in telecommunication technology to amplify optical signals and make long range transmission possible [48, 49]. Other applications are found in medicine, which uses Erbium-Yttrium-Aluminium-Garnet (Er:YAG) laser. The wavelength of 2 940 nm is highly absorbed by water and therefore by human tissue, which allows for energy deposition in shallow tissue [50]. Er:YAG laser also find their use in dentistry [51]. For research in the field of cold atom physics, erbium is interesting due to the highly dipolar character of theses atoms and its rich spectrum of Feshbach resonances, which provides an additional control parameter [52]. Erbium shows dipole-dipole interactions whose strength can be controlled by external magnetic fields by scanning through the Feshbach resonances. Alkali atoms show only contact interaction.

For the experiment presented in this thesis atomic erbium, more precisely the ^{168}Er bosonic isotope with its relative high abundance [47] and favourable scattering properties [52], was chosen. The available optical transitions in erbium atoms are suited for the planned experiments. Narrow line transitions allow for high relative detunings whereas the absolute difference in wavelength is small and can be easily achieved with acousto optical modulators. The mass of ^{168}Er is $167.932368\,u$ with u the atomic mass unit [53]. Erbium has two electrons missing in the inner 4f shell, which results in a rich energy spectrum, see fig. 2.1. Even though a rich energy spectrum comes with disadvantages, e.g. several decay channels for excited states to name one, the advantages surpass the drawbacks. Erbium shows a non vanishing orbital angular momentum of $L = 5$ in its electronic ground state given by $1s^2 2s^2 2p^6 3s^2 3p^6 3d^{10} 4s^2 4p^6 4d^{10} 5s^2 5p^6 4f^{12} 6s^2 =$ [Xe] $4f^{12}6s^2$ which allows for optical manipulation in the gross structure with large expected coherence times. Larger optical detunings compared to alkali atoms in which optical manipulation takes place in the fine structure splitting can be used. A drawback for the here presented experiment caused by the non vanishing orbital angular momentum is the relatively high magnetic moment of $\approx 7\mu_B$ with μ_B the Bohr magneton which makes optical transitions in erbium highly sensitive to magnetic stray fields. Another suitable atom species would be dysprosium which has been used successfully by other groups, e.g. [54–56]. Dysprosium has similar properties as erbium and is also part of the lanthanide group. However, dysprosium has an even higher magnetic moment of $\approx 10\mu_B$.

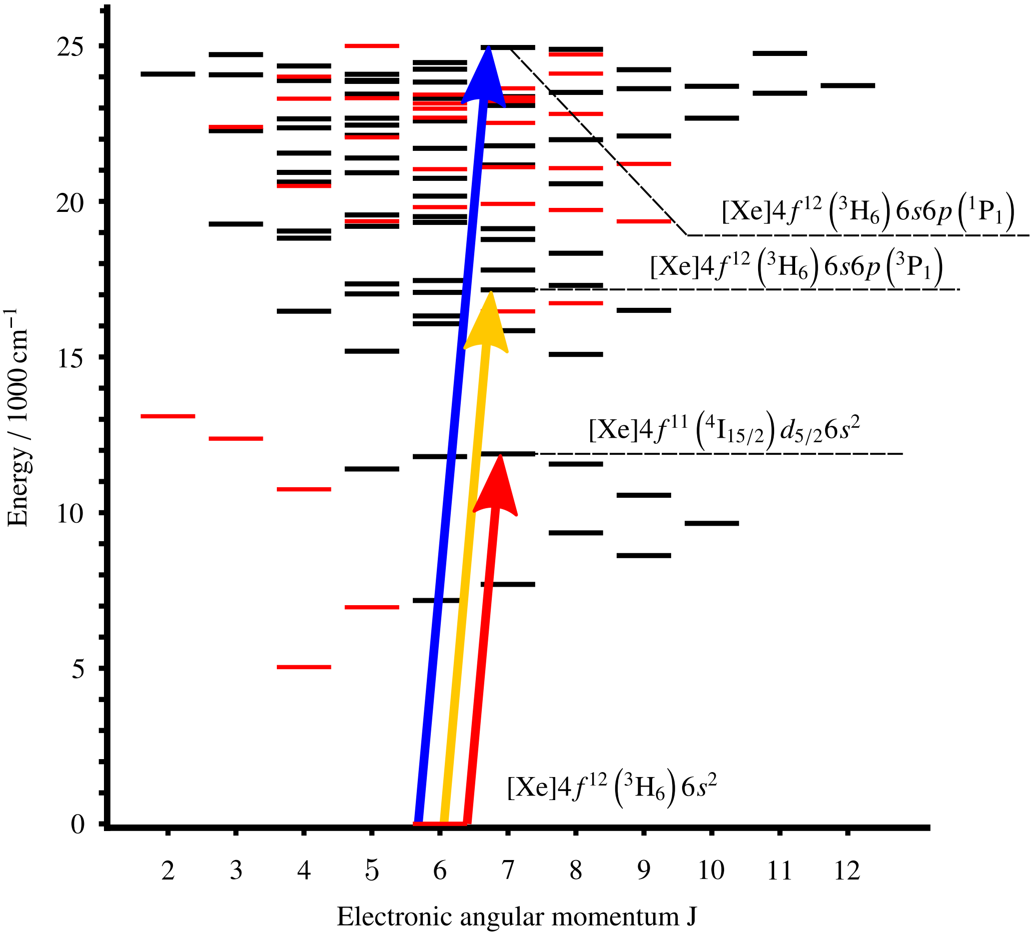

Figure 2.1: Energy level scheme up to a wave number of 25 000 cm^{-1}. The arrows show the relevant transitions for this thesis with their corresponding electronic states and are introduced in section 2.2. The blue arrow corresponds to the transition near a wavelength of 401 nm, the yellow arrow to the transition near a wavelength of 583 nm and the red arrow to the transition near a wavelength of 841 nm. Figure taken and modified from [57]

2.1 Electronic ground state

Using the Madelung rule the 6s orbital is filled prior to the 4f orbital which leaves two missing electrons in the 4f orbital. Erbium, as other lanthanide atoms, is an exception of jj-coupling and JJ-coupling has to be used to describe the electronic state in which part of the electrons couple via LS-coupling to $\vec{J}_1$ and the rest of the electrons couple to $\vec{J}_2$ [58]. The total angular momentum then couples to $\vec{J} = \vec{J}_1 + \vec{J}_2$. In erbium the inner shells including the 4f shell couples to $\vec{J}_1$ and the outer shells couple to $\vec{J}_2$. Due to the completely filled 6s shell and therefore vanishing contribution to the electronic ground state, the electronic ground state is determined by the inner shells and reads $^3H_6$.

Excited states with an electron lifted out of the 6s shell are described by the coupling of the $^3H_6$ state to the state of the two outer electrons. The relevant excited states are given with the corresponding transitions described in the following sub sections.

2.1.1 Zeeman splitting

A central aspect for the work in this thesis is the Zeeman splitting of erbium. The in chapter 5.1 introduced spin-orbit coupling, which is based on optical Raman coupling couples different ground states via a two photon process. To lift the degeneracy of the $J = 6$ ground state of erbium into its $2J + 1$ energy levels the Zeeman effect is used. For external magnetic fields below 50 G, as used in the work of this thesis, the Zeeman splitting is linear and has a slope of $1.628879\,\mathrm{MHz\,G^{-1}}$ [52].

2.2 Relevant transitions

In this thesis three optical transitions are relevant. The transition near a wavelength of 401 nm with a linewidth of about 30 MHz is used for pre-cooling the atoms and for absorption imaging. A narrow line transition with a linewidth of about 190 kHz near 583 nm is used for the magneto-optical trap. Another narrow line transition near 841 nm with a linewidth of about 8 kHz is used to realise optical Raman transitions.

Transition near 401 nm

The transition near the wavelength of 400.91 nm, from here on referred to as 401 nm transition, is used for optical cooling in the Zeeman slower and the transversal cooling, see section 3.1.2. It is also used for the absorption imaging system. In this transition one of the electrons in the 6*s* orbit is lifted into the 6*p* orbit. The 6*s*- and 6*p*-electron then couple to a $^1\mathrm{P}_1$ state. The 401 nm transition has a natural linewidth of 29.7 MHz, which results in a strong optical force. Therefore, it is suitable to pre-cool the atoms below the trapping velocity of the realised magneto-optical trap. An early version of this experiment used the 401 nm transition also for the magneto-optical trap. However, due to the large Doppler temperature T_D of 714 µK for the 401 nm transition it was not possible to load sufficient atoms in a far detuned optical dipole trap to allow for a further cooling to a Bose-Einstein condensate [59].

Transition near 583 nm

The transition near the wavelength of 582.84 nm, from here on referred to as 583 nm transition, is used for the magneto-optical trap. In this transition one of the electrons in the 6*s* orbit is lifted into the 6*p* orbit. The 6*s*- and 6*p*-electron then couple to a $^3\mathrm{P}_1$ state. Due to the narrow natural linewidth of 190 kHz the Doppler temperature is as low as 4.6 µK. This transition was successfully used for a magneto-optical trap by [52, 60, 61] and later adapted at the here presented experiment [62]. The low Doppler temperature is an ideal starting point to load atoms in an optical-dipole trap, which will be presented in the next chapter.

Transition near 841 nm

The transition near the wavelength of 841.22 nm, from here on referred to as 841 nm transition, is used for an optical Raman manipulation. The linewidth of 8 kHz allows for a large relative detuning whereas the absolute wavelength difference is comparably small and can be realised with acousto optical modulators. In this transition one of the electrons in the 4*f* orbit is lifted into the 5*d* orbit. The inner shell then couples to a $^4\mathrm{I}_{15/2}$ state.

Table 2.1: Parameters of the used transitions in this experiment. Properties cited from [52], [63], [64] and [65].

Wavelength in vacuum		400.91 nm	582.84 nm	841.22 nm
scattering rate in $\frac{1}{\mathrm{s}}$	γ	1.87×10^{8}	1.17×10^{6}	5.0×10^{4}
lifetime in ns	$\tau = \frac{1}{\gamma}$	5.4	857	20 000
natural linewidth in MHz	$\Delta\nu = \frac{\gamma}{2\pi}$	29.7	0.19	8.0×10^{-3}
saturation intensity in $\frac{\mathrm{mW}}{\mathrm{cm}^2}$	$I_\mathrm{S} = \frac{\pi h c \gamma}{3\lambda^3}$	60.4	0.12	1.8×10^{-3}
Doppler temperature in µK	$T_\mathrm{D} = \frac{\hbar\gamma}{2k_\mathrm{B}}$	714.2	4.5	0.19
Doppler velocity in $10^{-3}\,\frac{\mathrm{m}}{\mathrm{s}}$	$v_\mathrm{D} = \sqrt{\frac{k_\mathrm{B} T_\mathrm{D}}{m}}$	267	21	3.1
recoil temperature in nK	$T_\mathrm{r} = \frac{\hbar^2 k^2}{2mk_\mathrm{B}}$	717	339	80.5
recoil velocity in $10^{-3}\,\frac{\mathrm{m}}{\mathrm{s}}$	$v_\mathrm{r} = \frac{\hbar k}{m}$	5.9	4.1	2.8

CHAPTER 3

Bose-Einstein condensation of erbium atoms

The work presented here starts with the preparation of a Bose-Einstein condensate (BEC) with erbium atoms. The first erbium BEC was realised by the group around Prof. Francesca Ferlaino in Innsbruck in 2012 [66] followed by the second Erbium BEC using a similar scheme by our group at the end of 2015 and published in 2016 [62]. The experimental realisation will be introduced briefly by presenting the different experimental stages. Even though details have changed throughout the years, the basic principle stayed the same and more detailed descriptions of the preparation of the BEC can be found in [62, 67–69]. Changes in the method of preparing a BEC have no influence on the later presented artificial gauge fields.

Free atoms are created by an effusion cell, which makes a Zeeman slower necessary to pre-cool, or in other words decelerate, the atoms. The pre-cooled atoms are then captured in a magneto-optical trap (MOT) before loaded into an optical-dipole trap (ODT), realised by two crossed laser beams. Inside the ODT the atoms are evaporatively cooled to reach quantum degeneracy. The preparation time of a single BEC at the time of the measurements presented in this thesis was about 50 s. The loading of the MOT took about 20 s followed by the forced evaporative cooling of about 15 s. Further 15 s were necessary to synchronise with the magnetic fields of a fellow experiment, in which strong magnetic fields are ramped. The synchronisation made sure, that the critical measurements were performed while the magnetic field from the neighbouring group was held constant. Details on atom cooling and trapping can be found in [70] whereas details on Bose-Einstein condensation in [71].

3.1 Overview of the experimental apparatus

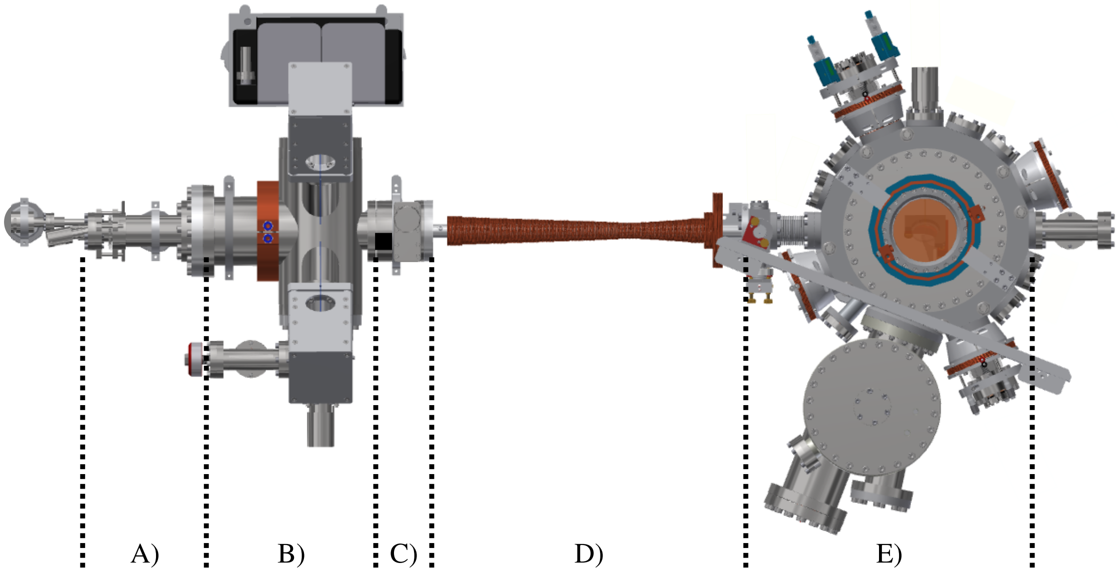

Figure 3.1: Overview of the vacuum system. A) Effusion cell B) Transversal cooling C) Oven shutter and valve D) Zeeman slower E) Main chamber. The technical drawing was kindly provided by the “Feinmechanik-Werkstatt des Instituts für Angewandte Physik”.

The presentation of the experimental apparatus will be restricted to the vacuum system and the attached magnetic and optical setups. The vacuum system can be divided into four sections: The effusion cell, the transversal cooling chamber, the Zeeman slower and the main chamber. The atoms leave the effusion cell into the transversal cooling chamber. A valve behind the transversal cooling chamber allows to separate the effusion cell and the transversal cooling chamber from the following Zeeman slower and the main chamber. A separation into two smaller vacuum chambers allows to refill the effusion cell with erbium much faster since the reestablishing of the vacuum takes less time. After the Zeeman slower the atoms enter the main chamber in which the optical trapping is realised.

The ultra high vacuum is produced by two ion getter pumps. The pressure inside the transversal cooling chamber is about 1×10^{-8} mbar and inside the main chamber about 1×10^{-10} mbar. A titan sublimation pump can be used to further reduce the pressure.

3.1.1 Effusion cell

The effusion cell is a “Dual-Filament Effusionszelle DFC-40-10-WK-2B” commercially available from CreaTec Fischer & Co. GmbH. The crucible located inside the effusion cell is depicted in fig. 3.2. The whole crucible is made from tantalum, which withstands the required high temperature above 1 200 °C. Tantalum shows inertness to chemical reactions, which is required to prevent the forming of low-melting alloys with erbium, which can potentially destroy the effusion cell. The crucible consists of two regions, the evaporation cell and the hot lip, which can be heated separately. The evaporation cell holds the solid erbium and is heated to a temperature of ≈ 1 200 °C [1] to evaporate free erbium atoms, which can enter the hot-lip region through a pipe of 3 mm diameter. The pipe has a length of 30 mm and is the first measure to restrict the atomic beam's convergence angle. The hot lip is heated to ≈ 1 300 °C to prevent the atoms from condensing at the pinholes of 3 mm diameter through which the atoms enter the pre-cooling chamber. From the Maxwell-Boltzmann distribution the mean velocity of the atoms leaving the oven can be estimated to be around 430 m s^{-1}.

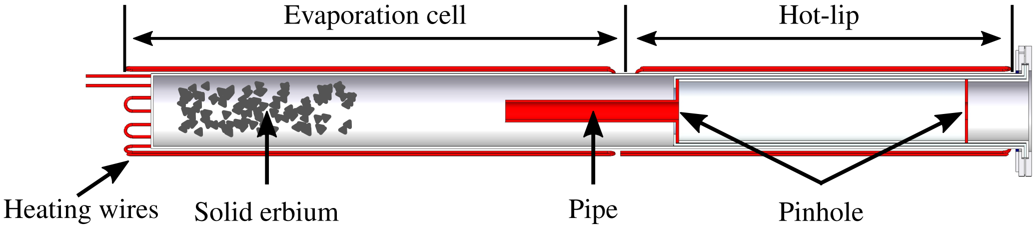

Figure 3.2: Overview of the crucible located on the inside of the effusion cell. The evaporation cell hold the solid erbium and is heated to ≈ 1 200 °C. The hot-lip consists of pinholes to create an atomic beam. A higher temperature in the hot-lip region prevents erbium from accumulating on the pinholes. The technical drawing was kindly provided by CreaTec Fischer & Co. GmbH.

3.1.2 Pre-cooling

Pre-cooling of the atoms is necessary since the trapping velocity of the MOT (≈ 2.2 m s^{-1}) [67] is much lower than the average velocity of the atoms leaving the oven (≈ 430 m s^{-1}). The pre-cooling consists out of two stages, which cools the atomic beam in two-dimensions: a transversal cooling stage and a Zeeman slower. Both systems use light frequency stabilised near the 401 nm transition and the effect of optical cooling to reduce the velocity of the atoms by a momentum transfer from the photons of the laser beam onto the atoms [70].

Transversal cooling

The transversal cooling (see fig. 3.3 left) reduces the transversal velocity distribution by irradiating the atomic beam by two counter propagating laser beam pairs. The laser beam pairs are realised using a single beam, which is guided two times through the atomic beam before it is reflected and guided back through the atomic beam twice. The laser beam profile has been chosen elliptically to increase the overlap of atomic beam and laser beam. The exact frequency of the light has been chosen by means of the maximum atom number trapped by the MOT and has not been further quantified. The transversal cooling stage enhances the collimation of the atomic beam, which increases the number of trapped atoms in the MOT by a factor 3.

The transversal cooling stage is followed by a pinhole with a diameter of 10 mm which cuts out higher transversal velocities and a shutter which allows for blocking the atomic beam. An older setup used a mechanical shutter directly behind the effusion cell which resulted in metallic erbium accumulating in the mechanical mechanism of the shutter. The shutter then frequently got stuck and needed repair. The new

---

[1] The melting point of erbium is 1 529 °C.

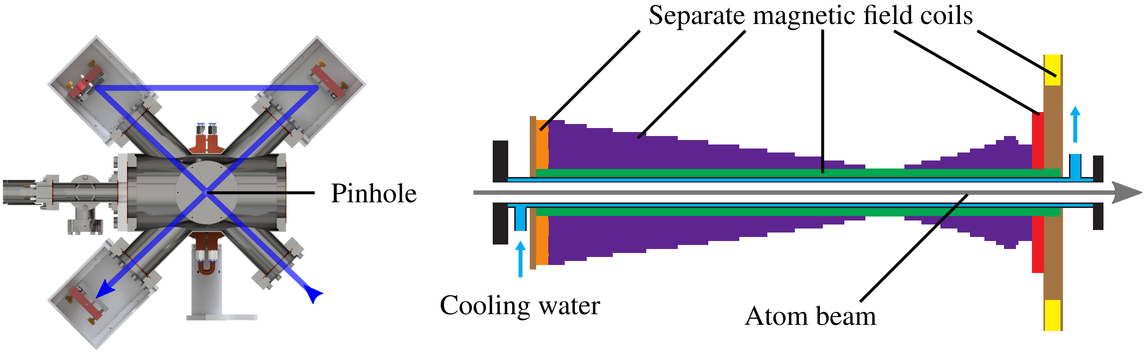

Figure 3.3: Left: technical drawing of the transversal cooling stage. The atomic beam comes out of the drawing's plane. The underlying technical drawing was kindly provided by the "Feinmechanik-Werkstatt des Instituts für Angewandte Physik". Right: schematic cut through the Zeeman slower's magnetic field coils. The separate magnetic field coils have separate power supplies, which makes the Zeeman slower tunable. Detailed information on the Zeeman slower can be found in [57, 59]. Figure taken and modified from [57].

shutter system is further away from the oven's exit which brings the advantage of a reduced atomic flux at the position of the shutter. The 10 mm pinhole provides additional shielding for the shutter's mechanics preventing erbium atoms from accumulating in the shutter's mechanics.

Zeeman slower

The following Zeeman slower (see fig. 3.3 right) changes the longitudinal velocity distribution of the atoms towards a smaller mean velocity. The Zeeman slower was designed and build in-house and consists out of different magnetic coils [57, 59]. For more information on the working principle of the Zeeman slower please refer to [57, 59] or [67]. In previous work it has been shown that the Zeeman slower used in this experiment changes the velocity distribution from a Maxwell-Boltzmann like distribution (mean velocity of $\approx 430\,\mathrm{m\,s^{-1}}$) to a flattened velocity distribution with a higher flux toward the capture velocity of the MOT of $\approx 2.2\,\mathrm{m\,s^{-1}}$. The modified velocity distribution provides an atomic flux which is sufficient to efficiently load the MOT [67].

3.1.3 Main chamber

The Zeeman slower is followed by the main chamber, depicted in fig. 3.4, which provides along its vertical axis two entry windows for one optical beam path and in the horizontal axis entry points for eight optical beam paths in total. The MOT and the ODT are realised in the main chamber therefore the atomic cloud is captured and manipulated inside the main chamber. The magnetic field coils needed for different applications are also mounted to the main chamber.

3.1.4 Magnetic field coils

To control the magnetic fields three pairs of bias coils are mounted to the chamber, see fig. 3.4, which can be used to create magnetic offset fields in the range of a few Gauss. To create and control magnetic

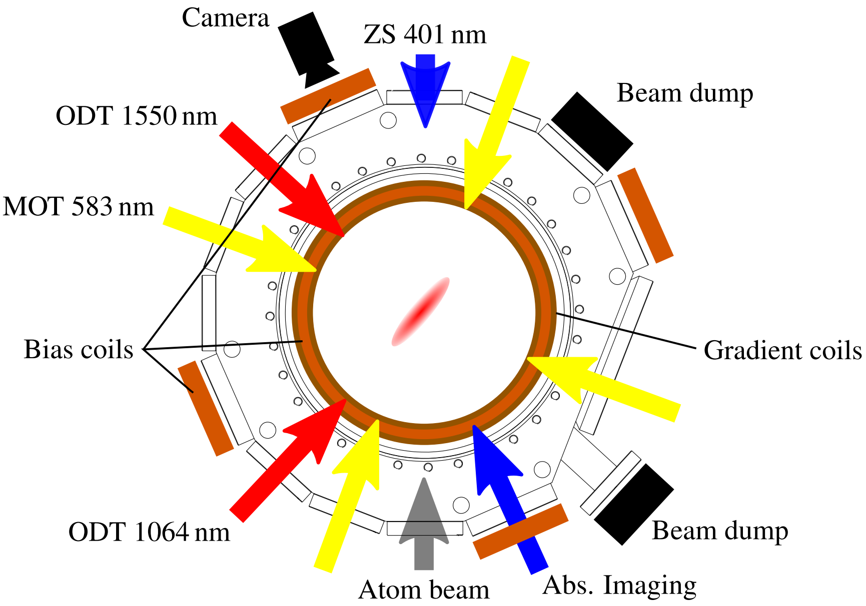

Figure 3.4: Vacuum chamber with optical paths and magnetic field coils used for the preparation of a BEC. The underlying technical drawing was kindly provided by the "Feinmechanik-Werkstatt des Instituts für Angewandte Physik".

field gradients a pair of water cooled coils in an anti-Helmholtz like configuration [2] is mounted to the chamber along the gravitational axis providing maximal gradients of $\approx 16\,\mathrm{G\,cm^{-1}}$ along the gravitational axis. Typically used gradients in this thesis are in the range of $4\,\mathrm{G\,cm^{-1}}$.

3.1.5 Magneto-optical trap

The pre-cooled atoms are trapped by a magneto-optical trap operated at the 583 nm transition. The MOT setup consists out of 3 counter propagating laser beam pairs and a quadrupole magnetic field realised by the anti-Helmholtz like coil pair. The laser beams are circularly polarised and counter propagating beams have opposite chiralities. The MOT phase consists of two sequences. The first sequence, the loading of the MOT, takes 20 s. During this time the oven shutter is open, the Zeeman slower and the transversal cooling lasers are on and the MOTs light detuning with respect to the 583 nm transition is about 30 linewidths of this transition. This relatively large detuning results in a large trapping area but also a weaker force and a higher temperature of the trapped atoms. The large trapping area results in the atoms being pulled down by gravity and being trapped below the Zeeman slower beam, see fig. 3.5. This prevents unwanted scattering of the trapped atoms with the Zeeman slower beam. Another advantageous effect of the large detuning is that atoms trapped in the MOT are more likely to interact with the σ^- polarised light coming from below due to the gravitational pull. The atoms are optically pumped into the $m_j = -6$ state and the ensemble is automatically spin polarised. In previous works it has been shown that this spin polarisation is conserved in the ODT [67, 68].

Once enough atoms are loaded (approximately 5×10^7 atoms) the oven is closed, the Zeeman slower light and the transversal cooling light is blocked before the frequency detuning of the MOTs light is ramped

---

[2] The distance between the coils is not exactly the radius of the coils, as in the case of a Helmholtz coil pair.

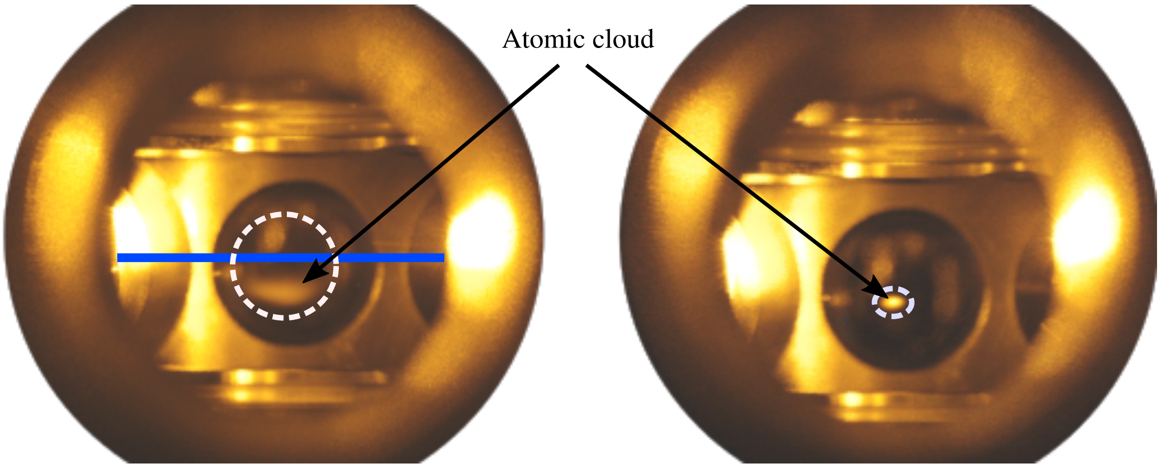

Figure 3.5: Picture of the loading phase (left) and compression phase (right) of the MOT through an access window. The blue line in the left picture shows the approximated path of the Zeeman slower laser beam. The white dashed circles depict the approximate trapping areas. Figure taken and modified from [69].

closer to resonance of about two natural linewidths in 700 ms. By ramping the frequency detuning closer to resonance the MOT is compressed and the temperature of the atoms changes from a few mK down to approximately 20 µK. Additionally to the frequency the MOT light's intensity and the magnetic fields are ramped in such a way, that the following loading into the ODT is optimised. The parameter ramping is followed by a hold phase in which the MOT parameters are held constant. During this holding time the MOT and the ODT are spatially overlapped. More details can be found in [67, 68, 72].

3.1.6 Optical-dipole trap

In earlier work on this experiment the ODT was realised by a single focussed CO_2 laser working at a wavelength of 10.6 µm [62, 67]. Later work used a crossed ODT realised by a CO_2 laser and a weak Nd:YAG laser operating at a wavelength of 1 064 nm [68]. The current version of this experiment uses a Mephisto MOPA 55 W Nd:YAG laser at 1 064 nm together with a NKT Koheras Boostik E15 15 W fibre laser at 1 550 nm, the beam arrangement is sketched in fig. 3.4. The change was necessary since the used CO_2 laser started to loose its single mode character probably caused by internal thermal fluctuations. In the experiment, it was observed that as a consequence quantum degeneracy in the atomic ensemble was not achieved every shot. The change in wavelength was done due to the better optics available for the wavelengths of 1 064 nm and 1 550 nm. The new laser systems improved the stability of the system and quantum degeneracy in the atomic cloud is reliably achieved. Even though the setup changed the trap parameters remained similar to the previous setups.

A notable change in the experimental routine is that the loading of the atoms from the compressed MOT into the ODT is possible by the spatial and temporal overlap of both traps. In the case of the CO_2 laser working at 10.6 µm it was not possible to have the light of both traps overlap spatially and being on at the same time. The loading efficiency was so low that in the following evaporative cooling quantum degeneracy was not achieved. Therefore, the MOT light at the end of the compression phase and the ODT light had to be chopped with a phase difference of 180°. The chopping allows to increase the loading efficiency but it did not allow for an increase in the number of atoms in the ODT with an additional holding time after the MOT compression phase. In the case of the Nd:YAG operating at 1 064 nm combined with the fibre laser working at 1 550 nm both traps, the MOT and the crossed ODT can be active at the same time and be spatially overlapped. This allows for using a MOT holding time in which the atoms are held after the compression while the ODT is already on. No chopping is required, which simplifies the technical implementation and reduces the error susceptibility. The loading efficiency has been improved and the technical implementation is much easier. The system showed to be more stable.

Typically around 4×10^6 to 5×10^6 atoms are loaded into the crossed ODT (measured after 1 000 ms after switching off of the MOT light). Forced evaporative cooling for approximately 15 s follows the loading. The laser beam power of the Nd:YAG laser is here ramped down to typically 0.5 % of the initial power. The power ramp consists of 5 consecutive linear ramps. The fibre laser beam power is ramped down to typically 8 % of the initial power within 3 consecutive linear ramps. The power ramps are followed by a waiting time in which the final power is held for 500 ms. A BEC with nearly all atoms in the ground state is reached with typically 4×10^4 to 7×10^4 atoms at temperatures below 100 nK. Radial trap frequencies are in the range of ≈ 100 Hz.

3.1.7 Absorption imaging

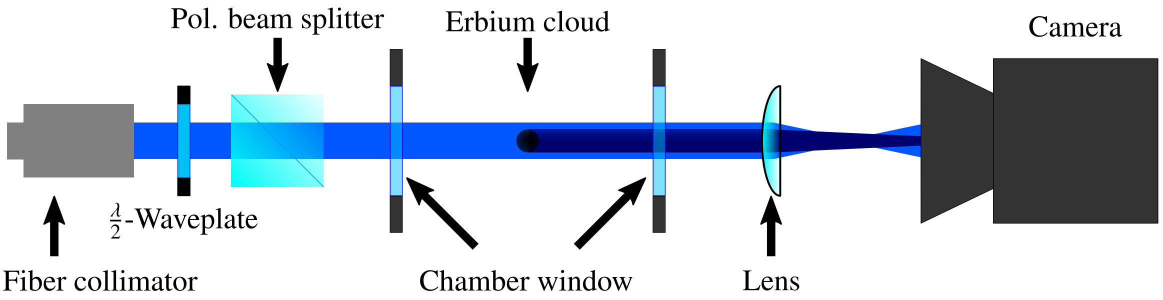

Figure 3.6: Absorption imaging setup. Due to the large distance between atoms and imaging lens the diffraction limit is ≈ 4 µm. The polarising beam splitter ensures that the light is linearly polarised.

For detection and analysis an absorption imaging setup is used, sketched in fig. 3.6. The atomic cloud is illuminated with resonant light for 80 µs using the 401 nm transition. During this time each atom scatters ≈ 500 photons [59]. The shadow image is then imaged onto a sCMOS[3] camera. Three images, one with the atoms (signal, intensity $I_\mathrm{S}(x,y)$), one only with the resonant light (flat, intensity $I_\mathrm{F}(x,y)$) and one dark image (dark, intensity $I_\mathrm{D}(x,y)$) without light are taken. Both, the signal and the flat image, are corrected by subtracting the dark image. The negative logarithmic ratio between the signal and the flat image corresponds to the optical density $D(x,y)$:

$$D(x,y) = -\ln\left(\frac{I_\mathrm{S}(x,y) - I_\mathrm{D}(x,y)}{I_\mathrm{F}(x,y) - I_\mathrm{D}(x,y)}\right). \tag{3.1}$$

Using the Beer-Lambert-law the optical density can be connected to the cross section σ_π and the column of atoms n via

$$D(x,y) = \sigma_\pi \int \mathrm{d}z\, n(x,y,z) \tag{3.2}$$

---

[3] Model Zyla sCMOS, Oxford Instruments

with

$$\sigma_\pi = C^2 \frac{3\lambda^2}{2\pi(1 + (2\delta/\Gamma)^2)} \tag{3.3}$$

being the cross section for linear polarised light. Here Γ is the natural linewidth of the used transition, δ the detuning of the light from resonance, λ the wavelength and C^2 the average squared Clebsch-Gordan coefficient [4]. The number of atoms can be estimated via

$$N = \int \mathrm{d}x\,\mathrm{d}y\,\mathrm{d}z\,n(x, y, z) = \frac{1}{\sigma_\pi} \int \mathrm{d}x\,\mathrm{d}y\,D(x, y). \tag{3.4}$$

The latter integral is done by integrating the pixel values.

A widely used tool in cold atoms experiment is the method of time-of-flight (TOF) measurements. After an ensemble of cold atoms is prepared the confining (trapping) potentials are turned off and the ensemble can evolve freely for a time t_{TOF} (referred to as TOF time) before an image of the atomic ensemble is taken. This method allows to transfer from position space into momentum space and holds information about the momentum distribution of the atoms. In this thesis TOF measurements have been used to verify that an atomic ensemble is in a BEC state by looking at the radius and optical density evolution for different TOF times. Later measurements in the synthetic quantum Hall system are based on TOF measurements combined with a spatial magnetic field gradient to distinguish not only between different momentum states but also between different internal Zeeman states.

3.2 Bose-Einstein condensation

Several publications and books exist, which describe the physics of a Bose-Einstein condensate. Therefore, I would like to refer to external sources like [71] and just give examples of the verification that the atom cloud is in a BEC state.

Above the critical temperature a thermal ensemble of atoms follows the Maxwell-Boltzmann statistics. Therefore, a line-cut through a thermal atomic ensemble shows a Gaussian shaped density profile. For temperatures around the critical temperature the density profile becomes bimodal. A macroscopically occupied ground state can be observed by means of a sharp peak emerging in the centre of the atomic ensemble enclosed by a Gaussian shaped thermal cloud. With decreasing temperature less atoms occupy thermal states and more atoms occupy the ground state. The density profile can again be described by a single Gaussian density profile.

Figure 3.7 A) - C) presents density profiles of the atomic cloud for different ensemble temperatures controlled by the forced evaporative cooling ramps after a TOF time of 16 ms. In sub-figure A) a temperature above the critical temperature of $T_c \approx 170\,\mathrm{nK}$ has been chosen. The blue points are the experimentally determined density profile of the atomic cloud. In red a Gaussian function has been fitted to the experimental data. The expected Gaussian density profile can be confirmed. In sub-figure B) the temperature has been chosen near the critical temperature. The red fit is done with a single Gaussian function to the thermal part of the atomic ensemble. The orange fit it done with a bimodal function consisting of two Gaussian function. In sub-figure C) the thermal part (red Gaussian fit) vanishes almost completely and almost all atoms are in the ground state (orange bimodal fit). Here, typically between 4×10^4 to 7×10^4 atoms with temperatures in the regime of 100 nK are in the ground state. Phase space densities are around 10, indicating that a large

---

[4] $C^2 = 0.385$ for the transitions from $m_j = -6$ to $m_j = 6$

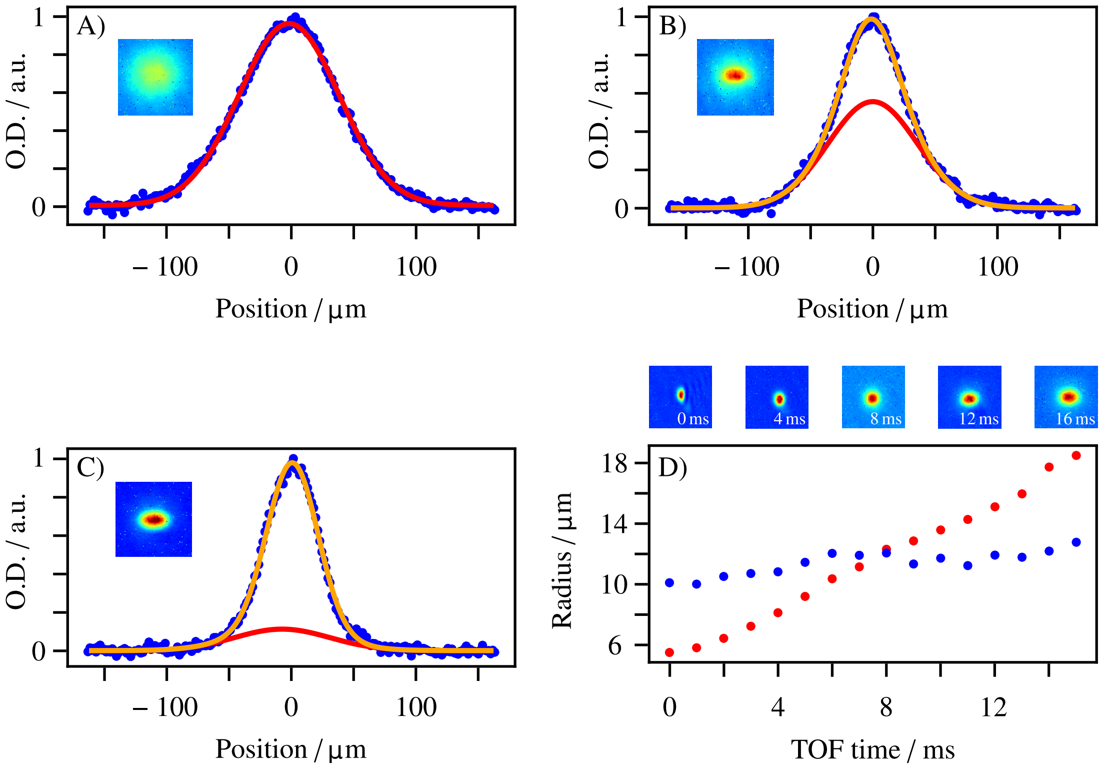

Figure 3.7: A), B), C,) Vertical line cuts through absorption images of atomic clouds. A) The observed optical density profile here still follows a Maxwell-Boltzman distribution, hence a Gaussian fit (red) to the data in blue. B) Further forced evaporative cooling results in a bimodal optical density profile (orange). The red Gaussian fit represents the thermal part. C) Further forced evaporative cooling leads to a decreasing thermal part (red). D) Radius (red: vertical radius, blue: horizontal radius) evolution during a TOF measurement. A radius inversion can be seen after 8 ms. Since the graphs only purpose is to verify a BEC error bars were ignored.

fraction of the atoms is in the ground state [5]. From the absorption images inside sub-figures A)-C) the transition is also observed. The colour scale connects a low density with blue towards high densities with red. Starting in sub-figure A) a dilute atomic gas is observed. With decreasing temperature, sub-figure B), the density in the centre increases depict by a colour change from yellow-green to red. A large yellow-green cloud around the red centre can still be observed. Below the critical temperature the density in the centre is maximised and the thermal part presented in a yellow-green colour is minimised. From the images a change in the aspect ratio can also be observed.

Sub-figure D) presents the evolution of the radius of the atomic cloud as function of the free evolution (TOF) time for a fixed temperature below the critical temperature. An atomic cloud with a macroscopically occupied ground state is expected to show a radius inversion upon a TOF measurement. Initially the horizontal axis, depicted in blue, is the long axis of the cigar shaped atomic cloud. After a free evolution time of ≈ 8 ms the radius inversion is observed and the initially short vertical axis, depicted in red, becomes the long axis.

---

[5] The phase space density is defined by $\rho_{\mathrm{psd}} = n_0 \lambda_{\mathrm{th}}^3$ with n_0 the spatial density of the atomic cloud and λ_{th} the thermal de Broglie wavelength. Atoms trapped in a harmonic trap need a phase space density larger than 1.2 to reach the BEC state [71].

Whereas the bimodal profile of the atomic cloud's line-cut confirms a macroscopically occupied ground state a radius inversion does not necessarily confirms a macroscopically occupied ground state. The radius evolution during a TOF measurement of atom species, which show a dipolar character and are subject to dipole-dipole interaction can be manipulated. An example would be the *d*-wave collapse which has been shown in similar cold atom systems [66, 73].

CHAPTER 4

Electrons in magnetic fields - the Hall effect

In 1980, Klaus von Klitzing experimentally observed the quantum Hall effect, which attracted wide general interest [4]. These experiments carried out in the domain of condensed matter physics require strong magnetic fields to reach the quantum Hall regime. This chapter aims at introducing the physics of electrons subject to a magnetic field. The physics behind the quantum Hall effect will be introduced following the book [74] and a lecture [75] before looking into the implementation of synthetic magnetic fields with ultracold erbium atoms in the next chapter. In general, due to the non charged nature of atoms, these systems lack the Lorentz force on which the quantum Hall effect relies. However, cold atom systems can be manipulated in a way that they mimic a system of charged particles in a magnetic field.

In this thesis the following notation will be used. Vectors are printed **bold** and operators are denoted by a hat. Correspondingly $\hat{\boldsymbol{r}}$ denotes a three dimensional position operator, whereas $\hat{x}$ denotes only the x-position operator and $\boldsymbol{e}_i$ with $i = x, y, z$ are the corresponding unit vectors.

4.1 Classical Hall effect

Since many textbooks are available on the topic of the Hall effect, only the key aspects of the classical Hall effect are introduced to support the understanding of the quantum Hall effect. For more details [74] is recommended. The classical Hall effect describes the occurrence of a potential difference known as Hall-voltage caused by an electron's two-dimensional motion in an external (static) magnetic ($\boldsymbol{B}$) and electric ($\boldsymbol{\mathscr{E}}$) field. Assuming an electron with elementary charge e and mass m_e is restricted to motion in the x-y-plane with velocity $\boldsymbol{v}$, the magnetic field along the z-axis and an additional force along the x-direction applied by an external electric field ($\mathscr{E}_x$), from the equation of motion

$$m_e \frac{d^2\boldsymbol{r}}{dt^2} = e(\boldsymbol{\mathscr{E}} + \boldsymbol{v} \times \boldsymbol{B}) \tag{4.1}$$

with $\boldsymbol{B} = (0, 0, B)$ and $\mathscr{E} = (\mathscr{E}_x, 0, 0)$ the classical trajectories can be derived

$$r(t) = \begin{pmatrix} x_0 + R\cos(\omega_c t + \phi) \\ y_0 + R\sin(\omega_c t + \phi) - \mathscr{E}_x t/B \\ 0 \end{pmatrix}. \tag{4.2}$$

For $\mathscr{E}_x = 0$, the case without an additional electric field, the electron is moving on a circle with radius

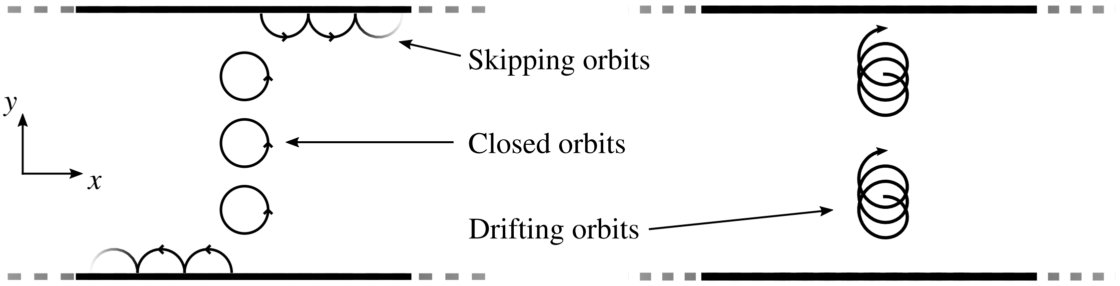

Figure 4.1: Left: electron trajectories in a two-dimensional plane without additional force along the x-direction. Inside the plane the electrons are moving on closed circles. Is the distance to the edge in the y-direction of the plane smaller that the cyclotron radius, the electrons are reflected from the edges and propagate along the edge in form of skipping orbits. Right: an additional force along the x-direction results in drifting orbits along the y-direction. This transversal drift is the main feature of the classical Hall effect.

$R = \frac{m_e v_\perp}{eB}$ and frequency $\omega_c = \frac{eB}{m_e}$, see fig. 4.1 left hand side. It is noticeable that an electric field along x-direction and therefore a force along x-direction results in a drifting orbit along the y-direction, see fig. 4.1 right hand side. This transversal drift of the electrons is called Hall current and is the defining property of Hall physics. The so called Hall mobility

$$\mu = \frac{\partial \langle v_y \rangle}{\partial F_x} \tag{4.3}$$

describes the response of the transversal drift velocity v_y as function of the applied force. In general the mobility is a function of the local properties of the system. For the bulk region, the region in which the electron has a distance D greater than R to the edge of the system, and a uniform force along the x-direction the mobility can be determined to be

$$\mu_{\text{bulk}} = \frac{\partial \langle v_y \rangle}{\partial F_x} = -\frac{d}{dE}\frac{E}{eB} = -\frac{1}{eB}. \tag{4.4}$$

Here a sample without defects was assumed. Defects in the sample can locally change the mobility. For distances smaller than R to the edge the cyclotron orbit can not complete its trajectory and the electron will rebound on the edge (assuming hard walls), resulting in so called skipping orbits creating an edge current. For decreasing distances smaller than R the mobility decreases until it vanishes completely. This behaviour can be explained in an intuitive way: Due to the restricted space along the y-direction the force along the x-direction has little to no effect anymore. The hard walls apply a counteracting force along the y-direction.

The transverse response of a classical Hall system can be measured in form of the Hall voltage U_H. Assuming a two-dimensional conductor through which a current I flows in x-direction, the Hall drift along y caused by a magnetic field along the z-direction and the underlying charge separation creates a potential difference along the y-direction. This potential difference can be measured. For the classical Hall effect the Hall voltage follows the strength of the magnetic field along the z-direction linearly and the Hall resistance

$$R_H = \frac{U_H(A_H B/d)}{I} \tag{4.5}$$

can be defined. Here A_H is the Hall constant and d the layer thickness of the sample. For strong magnetic fields (typically over 1 T) the linear response observed in suitable two-dimensional electron gas samples changes to a quantised behaviour and the Hall resistance takes the form $\rho_{xy} = h/(e^2\nu)$ with h Planck's constant and e the elementary charge. The variable ν can take integer values, called the integer quantum Hall effect (IQHE), or certain fractions called fractional quantum Hall effect (FQHE). The observed quantised behaviour makes a description in the quantum approach necessary. The IQHE is introduced since an IQHE like behaviour will be simulated later with the system which creates artificial magnetic fields. The FQHE, which is understood to arise from so-called Laughlin many particle states, is out of the scope of this thesis and is subject to continued work following this thesis. Therefore it will not be introduced here.

4.2 Landau Gauge

Before introducing the quantum Hall effect the Hamiltonian in the Landau gauge will be derived. Gauge theories connect magnetic fields to vector potentials, which allows to describe charged particles subject to magnetic fields. In the Landau gauge the vector potential $\boldsymbol{A}(\hat{\boldsymbol{r}})$ can be chosen by $\boldsymbol{A}(\hat{\boldsymbol{r}}) = (-B\hat{y}, 0, 0)$ or $\boldsymbol{A}(\hat{\boldsymbol{r}}) = (0, -B\hat{x}, 0)$ with $\boldsymbol{B} = B\boldsymbol{e}_z = B$. The Landau gauge breaks translational invariance and is therefore a preferable choice in the description of a quantum ribbon, which will follow in the later sections. Another advantage of the Landau gauge is that additional electric fields perpendicular to the magnetic field can be added to the description conveniently.

To motivate the necessity of a gauge the start is the gauge invariant Hamiltonian for an electron in an external magnetic field along the z-direction and free to move along the x and y-direction:

$$\hat{H} = \frac{\left(\hat{\boldsymbol{p}} + e\boldsymbol{A}(\hat{\boldsymbol{r}})\right)^2}{2m_e} \tag{4.6}$$

with $\hat{\boldsymbol{p}}$ the canonical momentum, e the elementary charge, $\boldsymbol{A}(\hat{\boldsymbol{r}})$ the vector potential and m_e the electron's mass. The gauge invariant eigenenergies of eq. 4.6 are known as Landau-levels and have been shown to resemble the eigenenergies of a harmonic oscillator given by

$$E_n = \hbar\omega_c\left(n + \frac{1}{2}\right), \tag{4.7}$$

with n an integer describing the energy level and $\omega_c = eB/m$ the so called cyclotron frequency. A plot of the energy levels as function of the momentum p_x can be seen in fig. 4.2 (left). The energy levels are equally separated by $\hbar\omega_c$.

To obtain information about the particle's wave function a gauge has to be chosen. The Landau gauge in the form $\boldsymbol{A}(\hat{\boldsymbol{r}}) = (-B\hat{y}, 0, 0)$ is chosen so that eq. 4.6 becomes

$$\hat{H} = \frac{\hat{p}_y^2}{2m} + \frac{(\hat{p}_x - eB\hat{y})^2}{2m} \tag{4.8}$$

with the motion of the electron restricted to the x-y-plane. Due to the translational invariance along the x-direction a plane wave ansatz can be chosen along the x-direction. The ansatz $\psi_k(x, y) = \exp(ikx) f_k(y)$

together with eq. 4.8 yields

$$\hat{H}\psi_k(x,y) = \left(\frac{\hat{p}_y^2}{2m} + \frac{(\hbar k - eB\hat{y})^2}{2m}\right)\psi_k(x,y) \tag{4.9}$$

with $\hat{p}_x = i\hbar\partial_x$. Introducing the magnetic length[1] $\ell = \sqrt{\frac{\hbar}{eB}}$ the Hamiltonian in eq. 4.9 can be expressed as

$$H = \frac{\hat{p}_y}{2m} + \frac{m\omega_c^2}{2}(\ell^2 k - \hat{y})^2, \tag{4.10}$$

which resembles a harmonic oscillator in x-direction, displaced by $\ell^2 k$. The eigenfunctions of the system are therefore known and can be expressed by the Hermite polynomials H_n

$$\psi_{n,k}(x,y) \sim e^{ikx} H_n(\hat{y} + k\ell^2)\exp\left(\frac{-(y - k\ell^2)}{2l^2}\right) \tag{4.11}$$

without any normalisation. $\psi_{n,k}(x,y)$ depends on the wave number k and the quantum number n whereas the eigenenergies in eq. 4.7 only depend on n. Each eigenenergie E_n is degenerate by the number of allowed k values.

4.2.1 Degeneracy

To determine the degeneracy of the Landau-levels the number of allowed k-values need to be derived. Assuming a finite sample size of $L_x \times L_y$ with periodic boundary conditions k becomes quantised in x-direction by $2\pi/L_x$ due to the translational invariance in x-direction. The choice of the gauge breaks translational invariance along the y-direction due to the shift of $y = -\ell^2 k$. For the allowed k-values it follows

$$0 \quad\leq\quad y \quad\leq\quad L_y \quad\Longrightarrow\quad -\frac{L_y}{\ell^2} \quad\leq\quad k \quad\leq\quad 0. \tag{4.12}$$

The total number of allowed states per Landau-level can be calculated by integrating over all possible k-values

$$N = \frac{Lx}{2\pi}\int_{-L_y/\ell^2}^{0} dk = \frac{L_x L_y}{2\pi\ell^2} = \frac{eBL_xL_y}{2\pi\hbar} = \frac{BL_xL_y}{\Phi} \tag{4.13}$$

with the quantum flux Φ which corresponds to the magnetic flux through an area of size $2\pi\ell^2$ (the area enclosed by the smallest possible cyclotron orbit of a charged particle).

4.3 Quantum Hall effect

Are the typical length scale in an experiment in the range of the Planck constant h, quantum effects have to be considered. The typical length scale for quantum Hall systems is the earlier introduced magnetic length $\ell = \sqrt{\hbar/(eB)}$. To derive the Hall resistivity $\rho_{xy} = \frac{h}{e^2\nu}$ an intuitive shortcut for a single free particle for the

---

[1] A charged particle free to move in a two-dimensional plane and subject to an external magnetic field perpendicular to the two-dimensional plane will move on a circular orbit. The smallest allowed radius is called magnetic length and is given by the uncertainty principle.

IQHE can be done [75]. The current can be connected to the particles velocity via

$$I = \frac{dQ}{dt} = \frac{dQ}{dV}\frac{dV}{dt} = \frac{dQ}{dV}\frac{Adx}{dt} = neAv \tag{4.14}$$

with n the charge carrier density, e the charge of a single particle, A the current cross-section and v the velocity. It follows for a single particle in one dimension[2] in the x-direction with $n = 1/L_x$

$$I_x = ev_x, \tag{4.15}$$

with the velocity in x-direction defined by

$$v_x = \frac{1}{i\hbar}\left[\hat{x}, \hat{H}\right]. \tag{4.16}$$

The Hamiltonian in the Landau gauge was derived in the previous section (eq. 4.10) and can be extended by an electric field $\mathscr{E}_y$ along the y-direction to

$$H = \frac{\hat{p}_y^2}{2m_e} + \frac{(\hat{p}_x + eB\hat{y})^2}{2m_e} - e\mathscr{E}_y, \tag{4.17}$$

with the magnetic field B in z-direction. The states can be expressed by

$$\psi(x, y) = \psi_{n,k}(x, y - m\mathscr{E}_y/eB^2). \tag{4.18}$$

The total current I_x is then given by summing over the contributions of all filled states f:

$$I_x = e\sum_f v_x = \frac{e}{i\hbar}\sum_f \langle\psi_{n,k}|\left[\hat{x}, \hat{H}\right]|\psi_{n,k}\rangle = \frac{e}{m}\sum_\nu\sum_k \langle\psi_{n,k}|\frac{\partial}{\partial x} + eB\hat{y}|\psi_{n,k}\rangle \tag{4.19}$$

with ν filled Landau levels which are k degenerate. With

$$\langle\psi_{n,k}|\hat{y}|\psi_{n,k}\rangle = -\frac{\hbar k}{eB} + \frac{m\mathscr{E}_y}{eB^2} \tag{4.20}$$

the y-position expectation value it follows

$$\begin{aligned} I_x &= \frac{e}{m}\sum_\nu\sum_k \langle\psi_{n,k}|\hbar k + eB\left(-\frac{\hbar k}{eB} + \frac{m\mathscr{E}_y}{eB^2}\right)|\psi_{n,k}\rangle && (4.21)\\ &= e\nu\sum_k \frac{\mathscr{E}_y}{B} && (4.22)\\ &= e\nu\frac{L_x\mathscr{E}_y}{\phi} && (4.23) \end{aligned}$$

where the degeneracy from eq. 4.13 was used. The one-dimensional current density is obtained by dividing through the length L_x in the x-direction

$$J_x = e\nu\frac{\mathscr{E}}{\phi}. \tag{4.24}$$

---

[2] A becomes the length L_x

The one-dimensional current I_y in y-direction vanishes since the electron's motion along the y-direction follows the motion of an harmonic oscillator with vanishing expectation value for the position operator. From the current density

$$\boldsymbol{J} = \begin{pmatrix} \sigma_{xx} & \sigma_{xy} \\ \sigma_{yx} & \sigma_{yy} \end{pmatrix} \begin{pmatrix} 0 \\ \mathscr{E} \end{pmatrix} = \begin{pmatrix} e\nu\frac{E}{\phi} \\ 0 \end{pmatrix} \tag{4.25}$$

the conductivity tensor can be obtained to be

$$\sigma_{xx} = \sigma_{yy} = 0 \text{ and } \sigma_{xy} = \sigma_{yx} = \frac{e\nu}{\phi} = \frac{e^2\nu}{2\pi\hbar}. \tag{4.26}$$

Hence, it follows for the resistivity $\rho_{xx} = \rho_{yy} = 0$ and

$$\rho_{xy} = \frac{2\pi\hbar}{e^2\nu}, \tag{4.27}$$

which is the known Hall resistivity.

4.3.1 The velocity of the electrons

The derivation of the Hall conductivity started by defining the one dimensional currents as $I_i = ev_i$. The velocity is connected to the dispersion relation via the Hellmann-Feynman theorem by

$$\langle v \rangle = \frac{\partial E_0}{\partial p}. \tag{4.28}$$

For the energies defined in eq. 4.7, an electron in a two-dimensional plane subject to a magnetic field perpendicular to the plane, the velocity is zero due to the flat bands. An electric Field $\mathscr{E}_y$ in y-direction would modify the eigenenergies to [74]

$$E_{nk} = \hbar\omega_c\left(n + \frac{1}{2}\right) - e\mathscr{E}_y k\ell^2 - \frac{m\mathscr{E}^2}{2B^2} \tag{4.29}$$

which effectively tilts the energy bands (depicted in fig. 4.2 right hand side) resulting in a constant velocity for all wave vectors k and thus creating a current.

4.3.2 Edge effects

Edges can be introduced to the system by adding potentials in at least one dimension. Adding a hard wall potential with $V(y) \neq 0$ for $y < 0$ and $y > L_y$, in between $V(y) = 0$, will result in skipping orbits if the distance between orbit centre and potential is smaller than the orbit radius. Therefore on the edges a charge transport is present. It can be shown that the velocity is connected to the potential V via [74]

$$\langle v_x \rangle = \frac{1}{eB}\frac{\partial V(y)}{\partial y}. \tag{4.30}$$

If both potential walls have the same strength the velocity and correspondingly the currents at the edges have the same absolute value but are different in direction. Therefore no net current is present. The situation changes in the case of different potential strengths. Here the absolute velocities are different at the edges

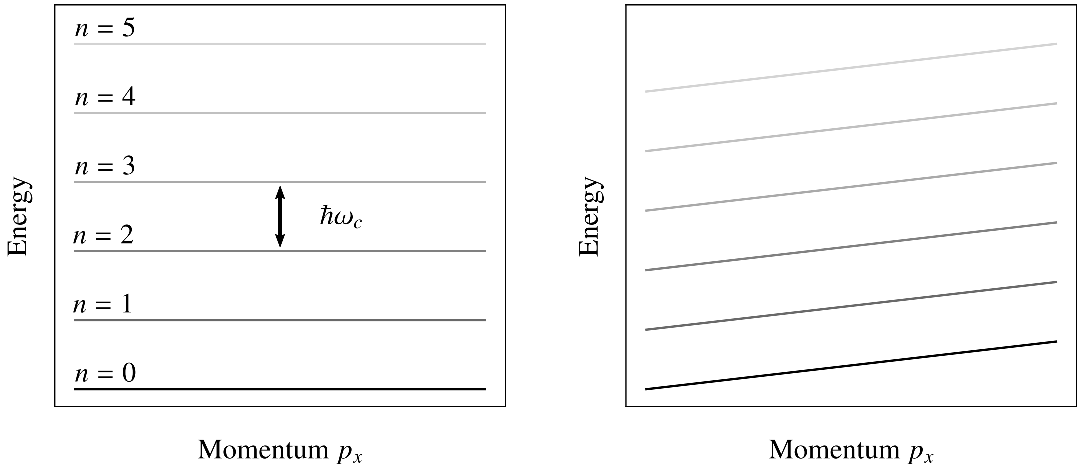

Figure 4.2: Left: energy of a harmonic oscillator. The energy levels are separated $\hbar\omega_c$ and are degenerate in p_x. Right: an additional electric potential in Hamiltonian 4.6 leads to tilted energy bands.

and a net current can be observed. Such a scenario is similar to a tilted dispersion relation realised by an electric field along the y-direction. However, in the edge case the edges result in skipping orbits and can result in an effective current.

In fig. 4.3 the numerically calculated dispersion relations and the corresponding velocities for an added potential well are depicted. The hard wall potential is approximated by a polynomial function of 14th order for calculation reasons. In the upper left plot of fig. 4.3 the flat lines bend in the proximity of the potential walls. Therefore the velocity is non zero with opposite signs for the edge on the left and respectively on the right hand side. In the bulk the velocity is zero, shown by the blue line in the lower left graph. If the potential walls have different strengths the energies are tilted as depicted in fig. 4.3 (right hand graphs). Therefore, the velocity is shifted and also non zero in the bulk. However, the velocity in the bulk is constant.

4.3.3 Local Chern Marker

To verify a quantum behaviour, which is distinguishable from classical physics, observables are required which show a quantum behaviour. For the quantum Hall effect one observable would be the just introduced conductivity or resistivity (eq. 4.27). For later measurements in the artificial Landau like system another more accessible quantity is chosen: the local chern marker (LCM). Therefore, the Chern number is introduced before defining the LCM.

Chern numbers are defined in the context of topology. Even though topology is not restricted to quantum physics it will be shown that the quantisation in the integer value of ν in the Hall conductivity in eq. 4.26 can be connected to the Chern number. Chern numbers are topological invariants, i.e. they do not change for smooth changes in the Hamiltonian of the system. This property makes Chern numbers of such great interest since disorder or small perturbations have no effect on the Chern number.

The chern number will be introduced here for a two-dimensional lattice similar to [45]. The starting point is a two-dimensional lattice in the x-y-plane with spacing a and periodic boundary conditions. Therefore,

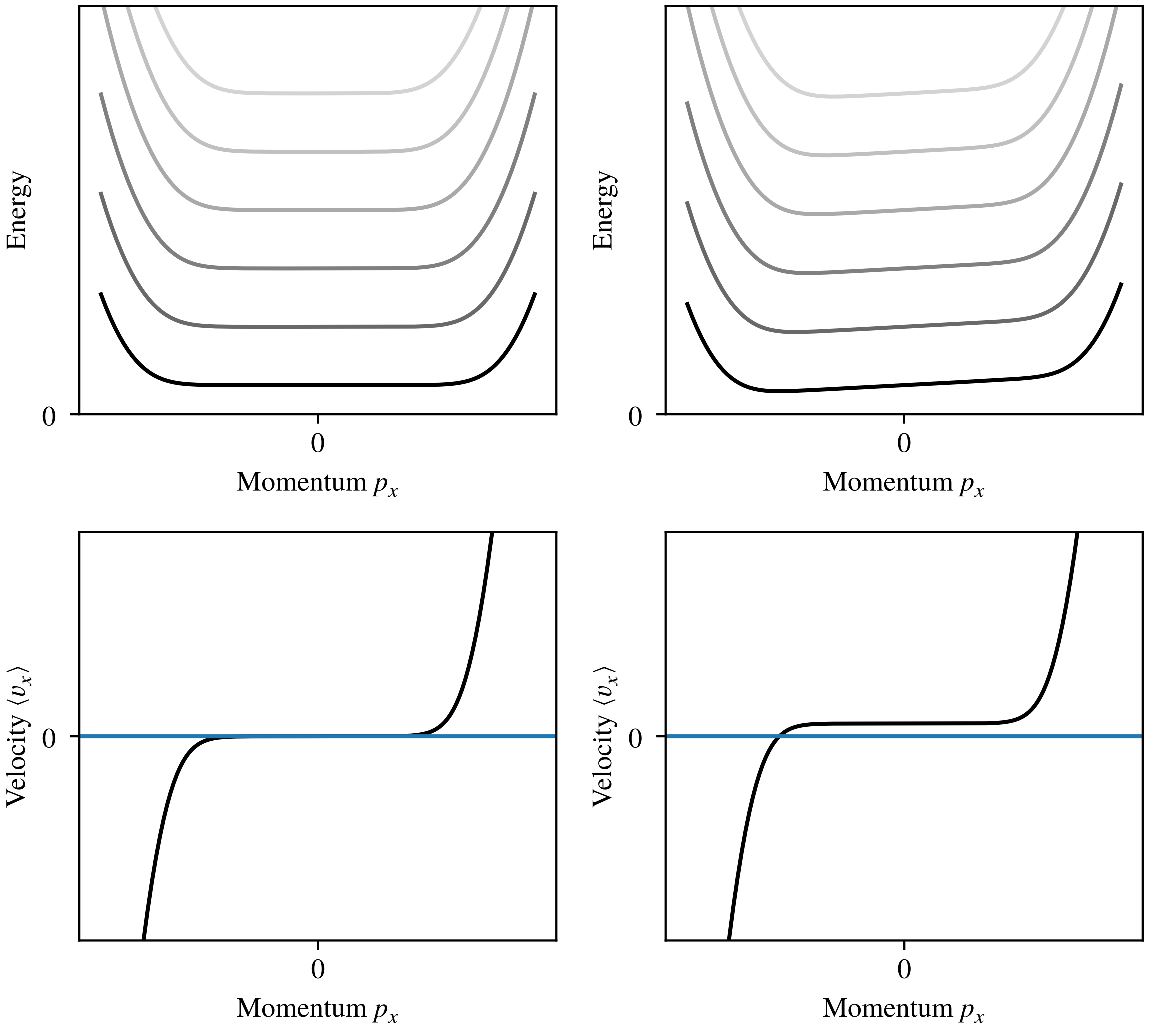

Figure 4.3: Top left: dispersion relation for a two-dimensional ribbon geometry. These simulations use a smooth potential at the edges for calculation reasons. Bottom left: velocity corresponding to the dispersion relation at the top left with the blue line marking a velocity of 0. The bulk has a vanishing velocity. The edges of the system show velocities with different signs. Right: same geometry and potential used as in the left column, but with an additional potential along the y-direction. The energy bands get tilted which results in a non vanishing, but constant, velocity in the bulk. The velocity receives a global offset.

the system underlies translational invariance which makes a Bloch Ansatz a valid choice:

$$\Psi_{n,\boldsymbol{k}}(\boldsymbol{r}) = e^{(i\boldsymbol{k}\boldsymbol{r})}u_{n,\boldsymbol{k}}(\boldsymbol{r}) \tag{4.31}$$

with n the band index and $\boldsymbol{k}$ the two-dimensional wavevector. The Bloch theorem states that $u_{n,\boldsymbol{k}}(\boldsymbol{r})$ is a periodic function with

$$u_{n,\boldsymbol{k}}(x,y) = u_{n,\boldsymbol{k}}(x+a,y) \text{ and } u_{n,\boldsymbol{k}}(x,y) = u_{n,\boldsymbol{k}}(x,y+a). \tag{4.32}$$

The so called Berry connection $\mathscr{A}_{n,\boldsymbol{k}}$ and the Berry curvature $\Omega_{n,\boldsymbol{k}}$ are introduced as [76]

$$\mathscr{A}_{n,\boldsymbol{k}} = i\langle u_{n,\boldsymbol{k}}|\hat{\nabla}_{\boldsymbol{k}} u_{n,\boldsymbol{k}}\rangle \tag{4.33}$$

$$\Omega_{n,\boldsymbol{k}} = \hat{\nabla}_{\boldsymbol{k}} \times \mathscr{A}_{n,\boldsymbol{k}} \tag{4.34}$$

which are used to define the chern number $\mathscr{C}_n$ as the integral of the Berry curvature over the first Brillouin zone:

$$\mathscr{C}_n = \frac{1}{2\pi}\int_{\mathrm{BZ}} d\boldsymbol{k}\hat{\nabla}_{\boldsymbol{k}} \times \mathscr{A}_{n,\boldsymbol{k}} = \frac{i}{2\pi}\int_{\mathrm{BZ}} d\boldsymbol{k}\left(\langle\partial_{k_y}u_{n\boldsymbol{k}}|\partial_{k_x}u_{n,\boldsymbol{k}}\rangle - \langle\partial_{k_x}u_{n\boldsymbol{k}}|\partial_{k_y}u_{n,\boldsymbol{k}}\rangle\right). \tag{4.35}$$

The Kubo formula can be used to determine a connection between Chern number and conductance [77]. In general it gives the linear response of an observable from a time dependent perturbation,

$$\sigma_{xy} = \frac{ie^2}{\hbar}\sum_n \int d\boldsymbol{k}\frac{1}{2\pi}\left(\langle\partial_{k_y}u_{n\boldsymbol{k}}|\partial_{k_x}u_{n,\boldsymbol{k}}\rangle - \langle\partial_{k_x}u_{n\boldsymbol{k}}|\partial_{k_y}u_{n,\boldsymbol{k}}\rangle\right) = \frac{e^2}{h}\sum_n \mathscr{C}_n. \tag{4.36}$$

Comparing this equation with eq. 4.26 it can be seen that the value ν is the sum over the Chern numbers of the filled bands. Therefore, it can be concluded that each Landau level has a Chern number of 1.

Making the transition to the experiment presented in this thesis, edge effects have to be included. So far the derivation of the Chern number, which depends on global properties, was done for an infinite system. In a finite system like the one presented in this thesis the first Brillouin zone cannot be defined. Therefore another quantity called the local Chern marker (LCM) is introduced, which is a local property [78]. The LCM is expected to show the same value as the Chern number for regions far enough from the edge. It can be expressed by

$$c(x,y) = -i2\pi\,\langle x,y|\left[\hat{P}\hat{x}\hat{P},\hat{P}\hat{y}\hat{P}\right]|x,y\rangle \tag{4.37}$$

with $\hat{P}$ the projection operator onto the occupied states and $\hat{x}$, $\hat{y}$ position operators. In the thesis from T. Chalopin [45] it has been shown that for a system infinite in x-direction and finite in y-direction with hard walls as boundaries the LCM only depends on the y coordinate and can be expressed as

$$c(y) = \int dk|\psi_{0,k}(x,y)|^2\partial_k\langle\hat{y}\rangle_k. \tag{4.38}$$

The integration takes place over all occupied states and $\langle\hat{y}\rangle$ is the average position in state k.

The LCM is of great importance since it can be directly connected to the quantisation of the quantum Hall conductivity. An LCM, or Chern number, of zero is describing a trivial topology equivalent to free space whereas an LCM different to zero identifies a region with a non trivial topology. The intersection of regions with different topological order shows topological protected edge states, which have been observed [79–82]. Edge currents appearing at the border between regions of different Chern numbers are expected to be robust against local changes in the Hamiltonian due to the robustness of the topologically protected edge states.

A deeper look into the topological behaviour of ultracold atom systems and topological insulators can be found in [83] and [84].

CHAPTER 5

Artificial gauge fields with ultracold atoms

As described earlier, atoms are electrically neutral, but by suitable manipulation artificial magnetic fields can be synthesised. From analogy with the electron system described in chapter 4 it is clear that the generation of a suitable vector potential allows to implement an atomic system suitable to realise quantum Hall physics.

In general, the effect of a vector potential on a charged particle can be extracted from the dispersion relation of a particle with charge q in an external magnetic field. The canonical momentum is changed from $\hat{\boldsymbol{p}} = m\hat{\boldsymbol{v}}$ to $\hat{\boldsymbol{p}} = m\hat{\boldsymbol{v}} + q\boldsymbol{A}(\hat{\boldsymbol{r}})$. From the vector potential a magnetic field can be calculated by $\boldsymbol{B} = \hat{\nabla} \times \boldsymbol{A}(\hat{\boldsymbol{r}})$ from which the requirement of the spatial dependence of the vector potential for a non vanishing magnetic field can be derived.

Therefore, an equivalent vector potential for neutral atoms need to modify the momentum of the atoms with a spatial dependence. Such a modification can be realised by exposing the atoms by external light fields [85]. The spatial dependence can be realised by a spatially varying laser field intensity or a real magnetic field gradient. Both methods result in an effective optical coupling, which has a spatial dependence. The latter scheme has been realised by Y.-J. Lin et al. in 2009 for ultracold rubidium atoms [42].

An early approach in realising artificial vector potentials is based on the similar structure of the Lorentz force and the Coriolis force. By stirring an ensemble of ultra cold atoms into a rotation the appearing Coriolis force can be interpreted as Lorentz force [28–32].

Another way of creating artificial vector potentials for ultracold atoms is by inducing direction dependent tunneling rates in two-dimensional optical lattices. The aquired phase while hopping through the lattice can be identified with the Aharonov-Bohm phase, which is the phase collected by a charged particle traveling through a vector potential [33–36].

In this thesis the spatial dependence is created by using a different approach: the coupling between atoms and optical fields, which results in a pair of external momentum and internal Zeeman state of the atom, the so called spin-orbit coupling. The internal Zeeman state is used as an effective position. This synthetic dimension combined with one real dimension realises a two-dimensional system. In this picture $\boldsymbol{A}(\hat{\boldsymbol{r}})$ becomes a function of the position [1] and with this an artificial magnetic field $\boldsymbol{B}_{\text{Art}} = \hat{\nabla} \times \boldsymbol{A}(\hat{\boldsymbol{r}}) \neq 0$ can be defined. In 2014 a paper by Celi et al. proposed the idea of synthetic dimensions encoded into the hyperfine states of rubidium. In 2015 such a system was realised by two groups [86, 87] using two and three internal Zeeman states, respectively. In 2020 Chalopin et al. published a realisation with dysprosium atoms [44, 45]. Dysprosium, with its 17 internal states, allowed to clearly distinguish between an edge and

---

[1] Due to the specific momentum - synthetic position pairs.

a bulk behaviour as expected for a two dimensional quantum ribbon for the first time.

In the following chapter spin-orbit coupling is introduced and it will be shown how the internal degree of freedom of the atom can be used to mimic a quantum Hall system in the Landau gauge.

5.1 Spin-orbit coupling

Spin-orbit coupling (SOC) also known as spin-orbit interaction describes the interaction of a particle's motion with its internal spin in a potential. A well known effect is the internal atomic energy splitting due to the interaction of the magnetic dipole moment of the electron propagating through the electrostatic field of the positively charged atomic nucleus. Speaking of SOC in cold atomic systems often refers to the coupling between an internal atomic state (e.g. spin state) to a specific momentum state [88]. In this sense of coupling, an internal atomic state coupled with a momentum state allows to create artificial vector potentials for ultracold atoms and therefore allows to create artificial magnetic and electric fields, an important tool for quantum simulations.

The simplest example of SOC is a two level system (both states are stable) with energies E_1 and E_2, energy difference of $\mathit{\Delta} E = \hbar\omega$. The internal spin states being $s_1 = |\downarrow\rangle$ and $s_2 = |\uparrow\rangle$. With optical Raman coupling two energy levels are coupled via a third, virtual energy level E_v, see fig. 5.1. Two counter-propagating laser beams with frequency $\omega_1 = \omega_\mathrm{v}$ and $\omega_2 = \omega_\mathrm{v} - \mathit{\Delta} E - \delta$ illuminate the atom. ω_v is the angular frequency corresponding to the energy difference between the ground state and the virtual level.

In real experiments a virtual level is realised by using a far detuned real transition to an excited state E_e. For a detuning $\mathit{\Delta}$ from the excited state that is much larger than the linewidth of the transition the excited state can be adiabatically eliminated and the system can be described by an effective two-level system. A schematic of this optical Raman process can be seen in fig. 5.1.

An atom in energy state E_1, momentum state $-\hbar k$ and internal spin state $s_1 =\downarrow$ is expressed by $|\downarrow, -\hbar k\rangle$. By absorbing a photon of laser 1 and re-emitting a photon via stimulated emission from laser 2 and the right polarisation the atom can be transferred to E_2 and $|\uparrow, \hbar k\rangle$. At this point is should be mentioned that this explanation of two one photon processes is strictly speaking a single two photon process. However, thinking of two single photon processes makes the picture more intuitive.

The change in energy is accompanied by a momentum kick of $2\hbar k$ which is the two photon momentum. The detuning δ depends on the momentum state of the atom. The two photon process starting with a photon from laser 2 (grey dashed arrows in fig. 5.1) is suppressed, since the detuning δ is increased by $2 \times \mathit{\Delta} E$. Hence, an atom with spin down will have the momentum $-\hbar k$, whereas an atom with spin up will have a momentum of $\hbar k$.

Figure 5.1 shows the two photon process with the two ground states as well as the virtual state. The SOC can be described by a two photon process with an effective coupling strength $\mathit{\Omega}_\mathrm{eff}$ of

$$\mathit{\Omega}_\mathrm{eff} = \frac{\mathit{\Omega}_2 \mathit{\Omega}_1}{2\delta}. \tag{5.1}$$

Here $\mathit{\Omega}_1$ and $\mathit{\Omega}_2$ are the single photon Rabi frequencies to the virtual energy level and δ the detuning from two-photon resonance.

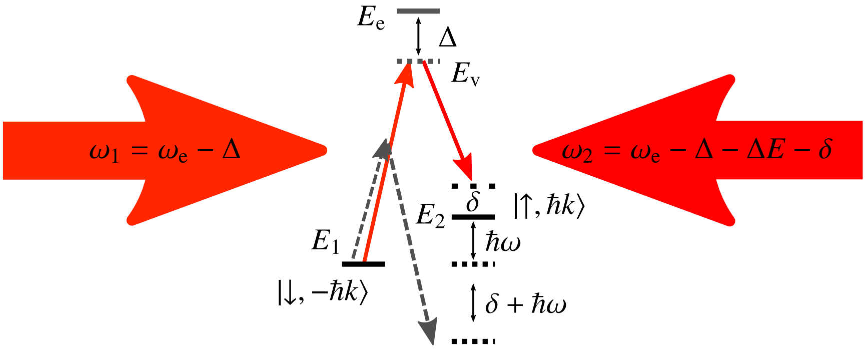

Figure 5.1: Scheme of spin-orbit coupling for an effective two level system. The two levels with energies E_1 and E_2 are coupled via a two photon process. A virtual energy level E_v can be realised by a using a far detuned real transition with energy E_e. Two pairs, $|\downarrow, -\hbar k\rangle$ and $|\uparrow, \hbar k\rangle$, of internal spin state and external momentum state are coupled.

5.1.1 Artificial gauge fields - Synthetic dimensions

The two level SOC is a well known scheme and its Hamiltonian can be expressed by

$$\hat{H}_{\text{2L,SOC}} = \frac{(\hat{\boldsymbol{p}} - \hbar \boldsymbol{k} \hat{\sigma}_z)^2}{2m} + \frac{\hbar \Omega}{2} \hat{\sigma}_x + \frac{\hbar \delta}{2} \hat{\sigma}_z \tag{5.2}$$

with $\hat{\sigma}_x$ and $\hat{\sigma}_z$ the Pauli matrices and Ω the two photon coupling strength, also known as two-photon Rabi frequency. The Hamiltonian for a charged particle with charge q in a magnetic field is given by

$$\hat{H} = \frac{(\hat{\boldsymbol{p}} - q\hat{\boldsymbol{A}})^2}{2m} \tag{5.3}$$

and by comparing it to eq. 5.2 a similar structure can already be identified. Ignoring additional terms in eq. 5.2 in both equations the canonical momentum is modified and $\hbar \boldsymbol{k} \hat{\sigma}_z$ can be identified with $\hat{\boldsymbol{A}}$, corresponding to an artificial vector potential.

In quantum theory the effect of a magnetic field on a charged particle can be described by the Aharonov-Bohm phase, which is the phase collected by a particle moving through a vector potential [27]. To collect the phase the particle does not necessarily needs to move through a magnetic or an electric field, but it is sufficient to move on a path, which encloses magnetic or electric field lines. Therefore, the effect of a magnetic field on a charged particle can completely described by the collection of such a phase. An atom propagating through the combination of real and synthetic dimension also collects a phase $\Phi = 2k\Delta x$ with $\Delta x = x_2 - x_1$ the real space displacement as shown in fig. 5.1 due to the interaction with the laser field. The collected phase $\Phi \neq 0$ can be interpreted as an equivalent to the Aharonov-Bohm phase.

5.1.2 Spin-orbit coupling for erbium atoms

In this thesis spin-orbit coupling is implemented by using optical Raman transitions, see scheme in fig. 5.3. A static magnetic field along the z-axis is used to lift the degeneracy of the ground state by $\Delta E = \vec{\mu}\vec{B} = \hbar\omega_z$. Two counter propagating, linearly polarised laser beams with angular frequencies ω_1 and $\omega_2 = \omega_1 + \omega_z + \delta$ along the x-axis intersect the atomic cloud. The linear polarisation of the laser beams are at a 45° angle with respect to the magnetic field in z-direction and are orthogonal to each other. Therefore, the atoms are subject

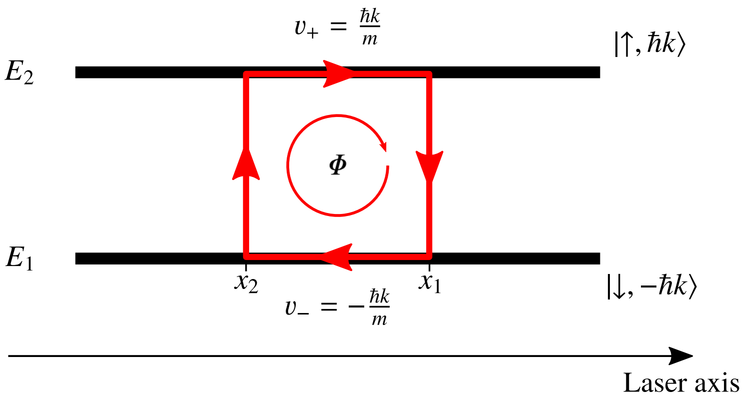

Figure 5.2: An atom transferred from state $|\downarrow, -\hbar k\rangle$, with energy E_1 and velocity $v_- = -\hbar k/m$, to $|\uparrow, \hbar k\rangle$, with energy E_2 and velocity $v_+ = \hbar k/m$, and back collects a total phase $\Phi = 2k\Delta x$ with $\Delta x = x_2 - x_1$ the real space displacement. This phase can be interpreted as an effective Aharonov-Bohm phase. The transfer from state $|\downarrow, -\hbar k\rangle$ to $|\uparrow, \hbar k\rangle$ and back can be interpreted as a closed loop through a two dimensional space with one real and one synthetic dimension imprinted in the internal spin state.

to π, σ_+ and σ_- polarised light. The optical Raman transitions in this experiment are using the 841 nm transition. Important energy scales are given by the transition angular frequency ω_0 and the frequency difference $\omega_{12} = \omega_2 - \omega_1$ of the two laser beams as well as the two photon detuning $\delta = \Delta E/\hbar - \omega_{12}$ and the single photon detuning $\Delta_s = \omega_0 - \omega_1 \approx \omega_0 - \omega_2$ with $\Delta_s \gg \delta$. Figure 5.3 shows the transition scheme of the optical Raman coupling for erbium in the case of $\delta m_j = +1$. In general atoms can be transferred by a two photon process to neighbouring Zeeman states with $\delta m_j = \pm 1$ via π-$\sigma_\mp$ and $\sigma_\pm$-π transitions. By effectively using π, σ_+ and σ_- polarised light the coupling between neighbouring Zeeman states is equally realised by π-$\sigma_\mp$ and $\sigma_\pm$-π transitions, giving a symmetric coupling. The symmetric coupling is necessary to realise flat dispersion relations, as will be seen section 5.3. The derivation of the Hamiltonian of the introduced system is identical to [45]. Important steps are explained in the following with a more detailed derivation in the appendix A. The start is a Hamiltonian which describes the atom light interaction [89]:

$$\hat{H} = \hat{H}_0 + \hat{H}_{\text{int}} \tag{5.4}$$

with $\hat{H}_0 = \hat{\boldsymbol{p}}^2/(2m) + \hbar\omega_z \hat{J}_z$ and

$$\hat{H}_{\text{int}} = V_0 \left\{ \alpha_s |\boldsymbol{u}|^2 \mathbb{1} - i\alpha_v (\boldsymbol{u}^* \times \boldsymbol{u}) \frac{\hat{\boldsymbol{J}}}{2J} + \alpha_t \frac{3[(\boldsymbol{u}^*\hat{\boldsymbol{J}})(\boldsymbol{u}\hat{\boldsymbol{J}}) + (\boldsymbol{u}\hat{\boldsymbol{J}})(\boldsymbol{u}^*\hat{\boldsymbol{J}})] - 2|\boldsymbol{u}|^2 \hat{\boldsymbol{J}}^2}{2J(2J-1)} \right\}. \tag{5.5}$$

$\hat{H}_0$ describes the particle's energy in a magnetic field along the z-direction with $\boldsymbol{p}$ the particle's momentum, m the particle's mass, $\hat{J}_z$ the dimensionless spin projection operator and ω_z the frequency of the corresponding Zeeman splitting. $\hat{H}_{\text{int}}$ describes the interaction between the atoms and the external light field. Here α_i are the scalar, vectorial and tensorial polarisation coefficients and $\hat{\boldsymbol{J}}$ is the total angular momentum operator with $J = 6$ in the case of erbium. The vectors $\boldsymbol{u}$ are the position dependent polarisation vectors defined by

$$\boldsymbol{u} = \frac{1}{2} e^{-i\omega_0 t} \left[e^{ikx} (\hat{\boldsymbol{y}} + \hat{\boldsymbol{z}}) + e^{-i(kx + (\omega_z + \delta)t)} (\hat{\boldsymbol{y}} - \hat{\boldsymbol{z}}) \right] \tag{5.6}$$

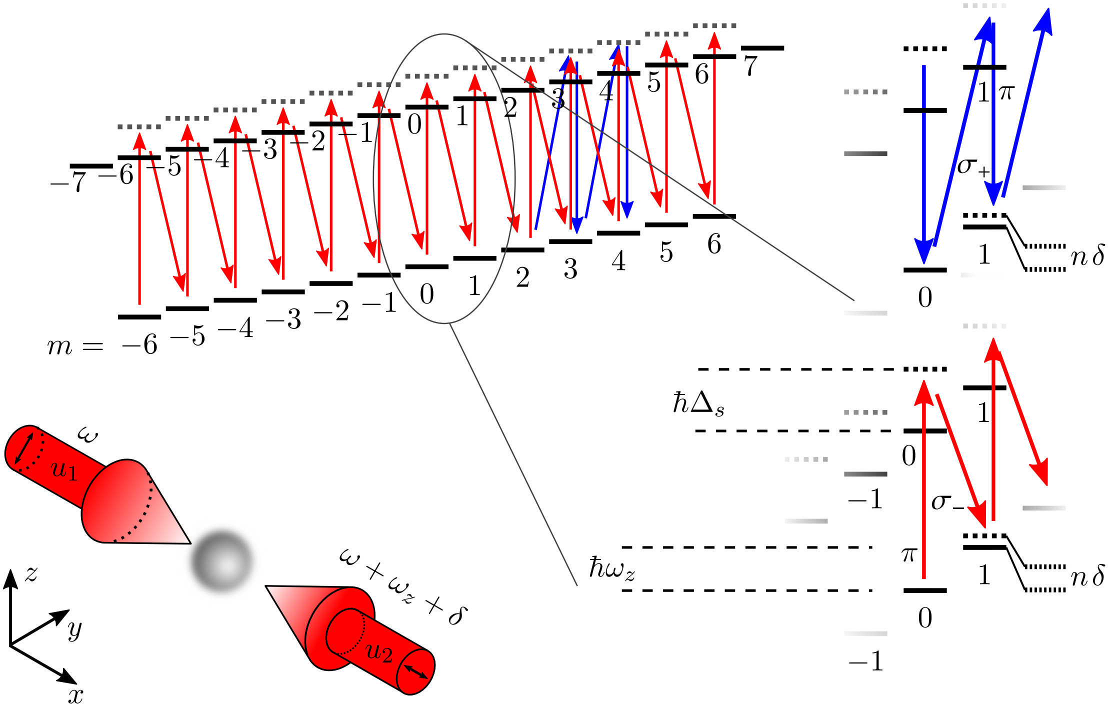

Figure 5.3: SOC in erbium with its 13 Zeeman states in the case of $\delta m_j = +1$. It is mentioned that both $\boldsymbol{u}_1$ and $\boldsymbol{u}_2$ consist of π,σ_+ and σ_- polarised light, which has not been sketched in the figure for better visibility. A SOC scheme only containing π-σ_- transitions (red) or σ_+-π transitions (blue) would result in a non flat dispersion relation. For a clearer overview not all σ_+-π (blue) transitions have been drawn. In the preparation scheme for this experiment n would be 7 since the detuning δ adds up per transition. The sample is initially prepared in $m_j = -6$.

and the coupling strength V_0 is given by

$$V_0 = \frac{3\pi c^2 \varGamma I}{2\omega_0^3 \varDelta_s}. \tag{5.7}$$

Here, c is the speed of light, $\varGamma$ the natural linewidth of the used transition, I the light's intensity and $\varDelta$ the single photon detuning. Combining eq. 5.5 and eq. 5.6 eq. 5.5 reduces to

$$\hat{H}_{\text{int}} = V_0 \left[\alpha_s \hat{\mathbb{1}} + \alpha_v \sin(\phi) \frac{\hat{J}_x}{2J} + \alpha_t \frac{\hat{\boldsymbol{J}}^2 - 3\hat{J}_x^2 + 3\cos(\phi)\left(\hat{J}_y^2 - \hat{J}_z^2\right)}{2J(2J-1)} \right] \tag{5.8}$$

with $\phi = 2kx + (\omega_z + \delta)t$. A unitary transformation to prepare a rotating wave approximation is applied by replacing $|\psi\rangle$ with

$$|\varPsi\rangle = \hat{U}\,|\psi\rangle = e^{i(\omega_z+\delta)t\hat{J}_z}\,|\psi\rangle \tag{5.9}$$

to transfer into a system rotating at $\omega_{\text{RWA}} = \omega_z + \delta$. It follows for $\hat{H}_0$

$$\hat{H}_{\text{RWA},0} = \frac{\hat{\boldsymbol{p}}^2}{2m} - \hbar\delta\hat{J}_z.$$

Before applying the transformation on $\hat{H}_{\text{int}}$, $\hat{J}_x$ and $\hat{J}_y$ are replaced by the ladder operators $\hat{J}_+ = \hat{J}_x + i\hat{J}_y$ and $\hat{J}_- = \hat{J}_x - i\hat{J}_y$. The unitary transformation is applied and $\hat{H}_{\text{int}}$ becomes

$$\hat{H}_{\text{RWA,int}} = V_0\Bigg[\alpha_s \mathbb{1} + \alpha_v \sin(\phi)\left(\frac{e^{i(\omega_z+\delta)t}\hat{J}_+ + e^{-i(\omega_z+\delta)t}\hat{J}_-}{4J}\right) \tag{5.10}$$

$$+ \frac{\alpha_t}{2J(2J-1)}\Bigg(\hat{\boldsymbol{J}}^2 - \frac{3}{4}\left(e^{2i(\omega_z+\delta)t}\hat{J}_+^2 + e^{-2i(\omega_z+\delta)t}\hat{J}_-^2 + \hat{J}_+\hat{J}_- + \hat{J}_-\hat{J}_+\right) \tag{5.11}$$

$$- \frac{3}{4}\cos(\phi)\left(e^{2i(\omega_z+\delta)t}\hat{J}_+^2 + e^{-2i(\omega_z+\delta)t}\hat{J}_-^2 - \hat{J}_+\hat{J}_- - \hat{J}_-\hat{J}_+ - 4\hat{J}_z^2\right)\Bigg)\Bigg]. \tag{5.12}$$

The rotating wave approximation (RWA) can be applied by only keeping slowly varying terms. A bit of caution has to be taken for the $\sin(\phi)$ term since ϕ contains a time component. Replacing the sine by its exponential form followed by some algebra leads to

$$\hat{H}_{\text{RWA,int}} = V_0\left[\alpha_s \hat{\mathbb{1}} + \frac{\alpha_v}{i8J}\left(e^{i2kx}\hat{J}_- - e^{-i2kx}\hat{J}_+\right) + \frac{\alpha_t}{2J(2J-1)}\left(\hat{\boldsymbol{J}}^2 - \frac{3}{2}\left(\hat{J}_x^2 + \hat{J}_y^2\right)\right)\right]. \tag{5.13}$$

At this point the SOC can already be seen: A change in the spin projection is associated with a momentum kick of $2k$. To make the momentum change more visible a unitary transformation in position space can be applied:

$$|\Psi\rangle = e^{i2k\hat{x}\hat{J}_z}|\psi\rangle, \tag{5.14}$$

and the total Hamiltonian follows to be

$$\hat{H}_{\text{SOC}} = \frac{\hat{p}_y^2 + \hat{p}_z^2}{2m} + \frac{(\hat{p}_x - 2\hbar k\hat{J}_z)^2}{2m} - \hbar\delta\hat{J}_z + V_0\left[\alpha_s \hat{\mathbb{1}} - \frac{\alpha_v}{4J}\hat{J}_y + \frac{\alpha_t}{2J(2J-1)}\frac{3}{2}\hat{J}_z^2\right] \tag{5.15}$$

where the trivial dynamics by $\hat{p}_y$ and $\hat{p}_z$ will be dropped in the following. The canonical momentum is then given by $\hat{p}_x = m\hat{v}_x + 2\hbar k\hat{J}_z$.

Equation 5.15 can be further simplified by explicitly writing out the polarisabilities. The scalar polarisability $\alpha_s \hat{\mathbb{1}}$ accounts for a constants energy offset and can be neglected. From [89] α_v and α_t can be determined to be

$$\alpha_v = \frac{90}{91} \tag{5.16}$$

$$\alpha_t = -\frac{22}{91} = -\frac{15}{2J+3}\frac{22}{91} \tag{5.17}$$

for the used transition which leads to

$$\hat{H}_{\text{SOC}} = \frac{(\hat{p}_x - 2\hbar k\hat{J}_z)^2}{2m} - \hbar\delta\hat{J}_z + V_0\left[-\frac{15}{364}\hat{J}_y - \frac{1}{2J+3}\frac{15}{364}\hat{J}_z^2\right] \tag{5.18}$$

$$= \frac{(\hat{p}_x - 2\hbar k\hat{J}_z)^2}{2m} - \hbar\delta\hat{J}_z - \hbar\Omega\left[\hat{J}_y + \frac{1}{2J+3}\hat{J}_z^2\right] \tag{5.19}$$

with $\hbar\Omega = V_0 15/364$. The calculation of the vectorial polarisability α_v and the polarisability tensorial α_t is shown in the detailed derivation in the appendix A.

5.2 From SOC to artificial Landau levels with erbium

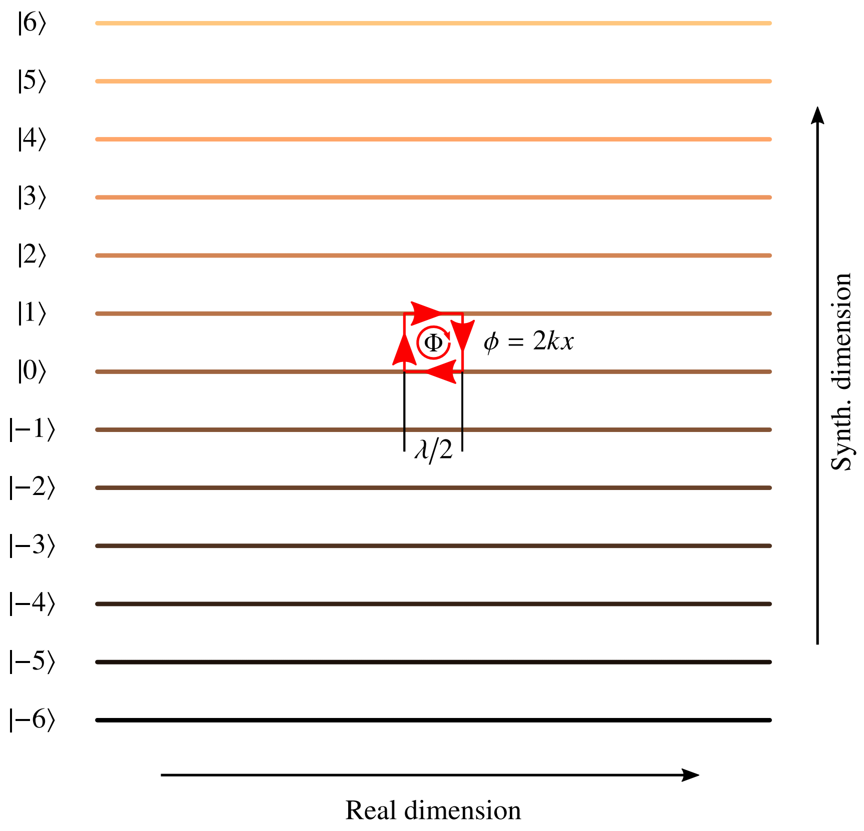

Figure 5.4: Two dimensional quantum ribbon. One dimension is the real space position whereas the second dimension is provided by the internal spin state of the erbium atoms. A spin flip leads to a transition through the synthetic dimension. An erbium atom moving on the closed red path collects a phase of $2k\Delta x$ with Δx being the displacement in real space. A displacement of $\Delta x = \lambda/2$ with λ the wavelength of the laser light results in a flux of $\Phi = 2\pi$.

The construction of the Hamiltonian in section 5.1.2 is intended to resemble an artificial Landau like system for cold atoms, which follows the dispersion relation for charged particles in a magnetic field in the Landau gauge. Comparing the Hamiltonian for a charged particle in the Landau gauge

$$\hat{H} = \frac{\hat{\boldsymbol{p}}_y{}^2}{2m} + \frac{(\hat{\boldsymbol{p}}_x - eB\hat{y})^2}{2m} \tag{5.20}$$

and the Hamiltonian 5.19 in SOC in resonance ($\delta = 0$)

$$\hat{H}_{\mathrm{SOC}} = \frac{(\hat{p}_x - 2\hbar k\hat{J}_z)^2}{2m} - \hbar\Omega\left[\hat{J}_y + \frac{1}{2J+3}\hat{J}_z^2\right] \tag{5.21}$$

$\hat{J}_z$ in $\hat{H}_{SOC}$ can be identified with $\hat{y}$, which means that the m_j state is interpreted as an effective position in an artificial dimension defined by the Zeeman state. The momentum corresponding to the two photon recoil momentum $p_{\mathrm{rec}} = 2\hbar k$ is then identified with eB. The connection of $\hat{p}_y^2$ with $\hat{J}_y$ is not trivial and has been shown in [45] as well as the additional term in $\hat{H}_{\mathrm{SOC}}$ proportional to J_z^2, acting as an additional trapping potential, which can be neglected in the context of the mapping used here.

Figure 5.4 shows the quantum ribbon spanned by the one real dimension given in direction of the laser light and the synthetic dimension provided by the internal spin states. The colour scheme used for the different spin states will also be used in the following chapter. As already introduced earlier a charged particle travelling through a vector potential collects the Aharonov-Bohm phase. An equivalent phase of $\Phi = 2k\Delta x$ with k the wave number of the light and Δx the real space displacement is collected by the erbium atoms in the two dimensional quantum ribbon. This phase allows for an interpretation of a charged particle in an external magnetic field. A closed loop with displacement $\Delta x = \lambda/2$ corresponds to a flux of $\Phi = 2\pi$.

The later shown experimental data will show that in most cases more than one internal spin state m_j is occupied. A continuous variable here called magnetisation, which is defined as the average m_j state of the system is introduced. Hence, in the case of erbium the magnetisation can take values between -6 and $+6$.

5.3 Dispersion relations

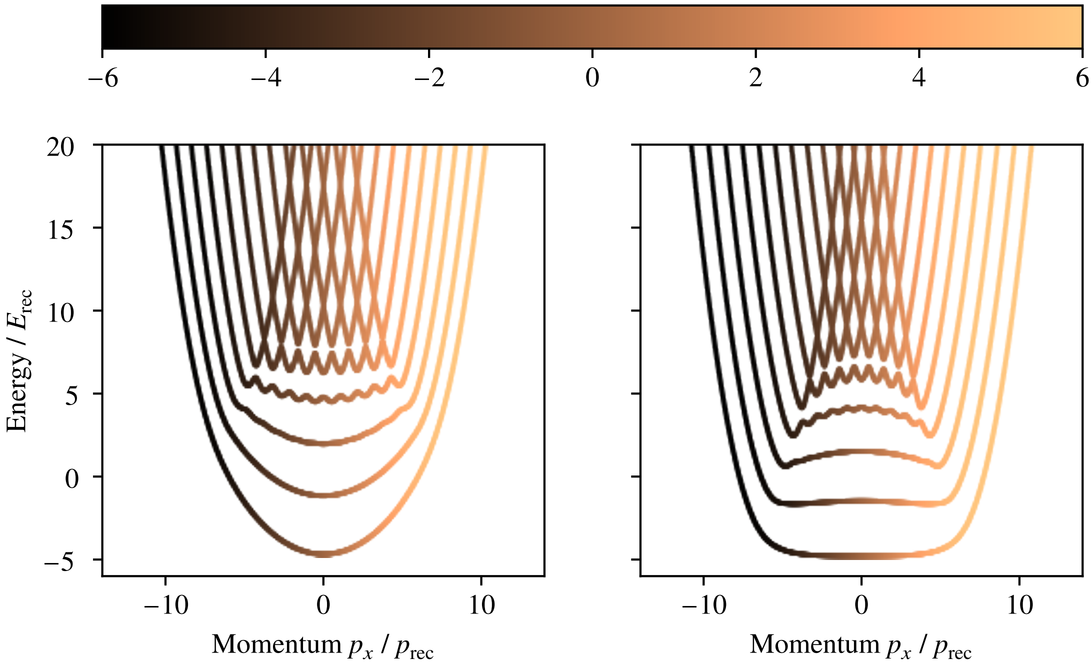

Figure 5.5: Dispersion relations of the spin-orbit coupled system. Left: a negative effective coupling of $\Omega = -\Omega_{\mathrm{rec}}$ results in curved dispersion relations. Right: a positive coupling of $\Omega = \Omega_{\mathrm{rec}}$ results in an almost flat lowest band for the central (bulk) region. The first excited band still shows a relative flat behaviour in the centre.

The Hamiltonian in eq. 5.19 should show a dispersionless bulk region similar to an electron Landau system. To verify this the eigenvalues are calculated as a function of the canonical momentum state p_x (from here on referred to as momentum p_x) for different effective coupling strengths and are shown in fig. 5.5 with the magnetisation encoded in the colour. The left plot in fig. 5.5 shows the dispersion relation for an effective coupling strength of $\Omega = -E_{\mathrm{rec}}/\hbar = -\Omega_{\mathrm{rec}}$ with E_{rec} the energy associated to a momentum kick of $2\hbar k$. The dispersion relations does not show a flat region for the lower bands. A positive effective coupling strength of $\Omega = \Omega_{\mathrm{rec}}$ has flat regions in the lower bands, as presented in fig. 5.5 right hand side. The flatness is caused by the counteracting dispersive effects of the terms proportional to $\hbar\Omega\hat{J}_y$ and $\hbar\Omega\hat{J}_z$ in the Hamiltonian from eq. 5.19 [44]. Therefore, it is concluded that a positive coupling is necessary to observe dispersion relations with a flat bulk.

To find a suitable coupling strength for later experiments the dispersion relation for different effective couplings from $\Omega = 0.1\ \Omega_{\mathrm{rec}}$ to $\Omega = 3\ \Omega_{\mathrm{rec}}$ are plotted in fig. 5.6. The size of the flat region in the lower bands are anti proportional to the coupling strength. Therefore, smaller couplings are in general preferable. However, couplings below $\Omega = \Omega_{\mathrm{rec}}$ show fast oscillations on the bands even in the lowest two bands. The lowest band and the first excited band are of special interest, since later experiments will look at the dynamics of the atoms when excited into a coherent superposition of states in the lowest and first excited band.

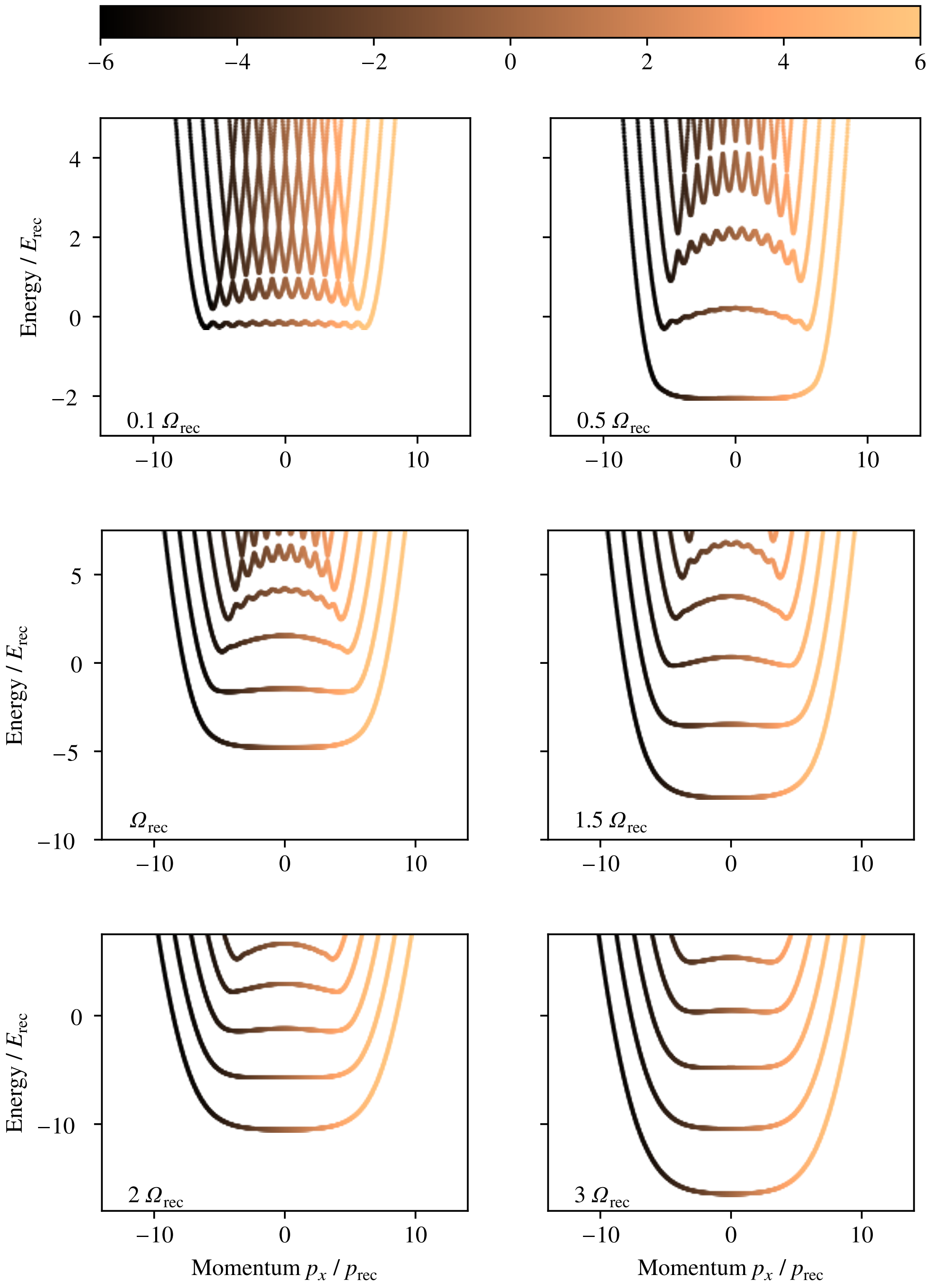

Figure 5.6: Dispersion relations for different positive coupling strengths (given within the corresponding graphs) to determine suitable coupling strengths for later experiments.

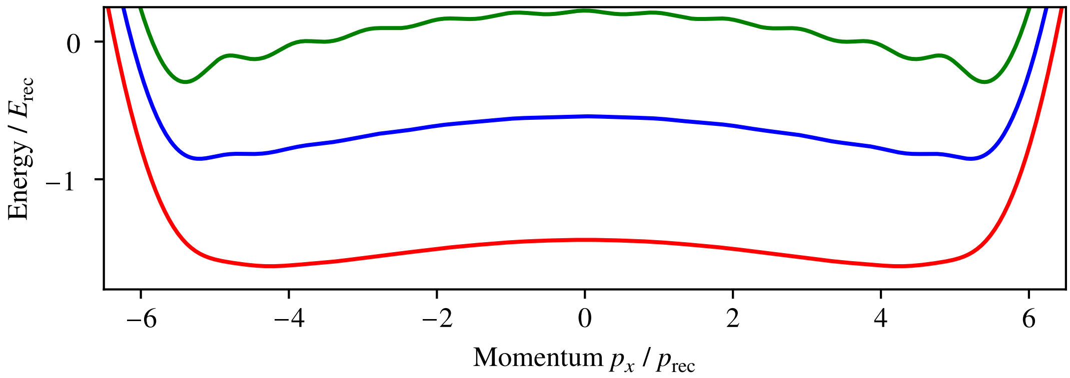

Figure 5.7: To determine the coupling strength for which no fast oscillations are observable in the first two bands the first excited bands for coupling strengths of $\Omega = 0.5\,\Omega_{\mathrm{rec}}$ (green), $\Omega = 0.75\,\Omega_{\mathrm{rec}}$ (blue) and $\Omega = \Omega_{\mathrm{rec}}$ (red) are plotted. A coupling strength of $\Omega = 0.5\,\Omega_{\mathrm{rec}}$ (green) shows clear oscillations whereas $\Omega = 0.75\,\Omega_{\mathrm{rec}}$ (blue) only shows remaining oscillations in the minimums. For a coupling strength of $\Omega = \Omega_{\mathrm{rec}}$ (red) the fast oscillations are suppressed in the first excited, and therefore also in the lowest, band.

Those fast oscillations are residuals from the uncoupled case [2]. For a better overview fig. 5.7 depicts only the first excited band for effective couplings of $\Omega = 0.5\,\Omega_{\mathrm{rec}}$ (green) , $\Omega = 0.75\,\Omega_{\mathrm{rec}}$ (blue) and $\Omega = \Omega_{\mathrm{rec}}$ (red). The lowest band is not shown since those fast oscillations are more dominant in higher bands, i.e. if the first excited band shows no fast oscillations the lowest band will also show no oscillation.

Whereas an effective coupling of $\Omega = 0.5\,\Omega_{\mathrm{rec}}$ shows a clear oscillation on the first excited band, these oscillations are almost completely suppressed for a coupling of $\Omega = 0.75\,\Omega_{\mathrm{rec}}$, which only shows residuals oscillations in the minima of the first excited band. For a coupling of $\Omega = \Omega_{\mathrm{rec}}$ no fast oscillations in the first band is observed.

In section 6.6.2 velocity measurements will be presented, since the group velocity of the atoms in the coupled system follow the derivative of the dispersion relation, see eq. 4.28. The group velocity is, in contrast to the dispersion relation, directly measurable in this experiment. The following discussion will be restricted to the ground band corresponding to the lowest Landau level (LLL) in an electron quantum Hall system.

---

[2] The uncoupled case shows 13 independent parabolas and is therefore a trivial scenario. The corresponding plot can be found in the appendix in fig. B.1.

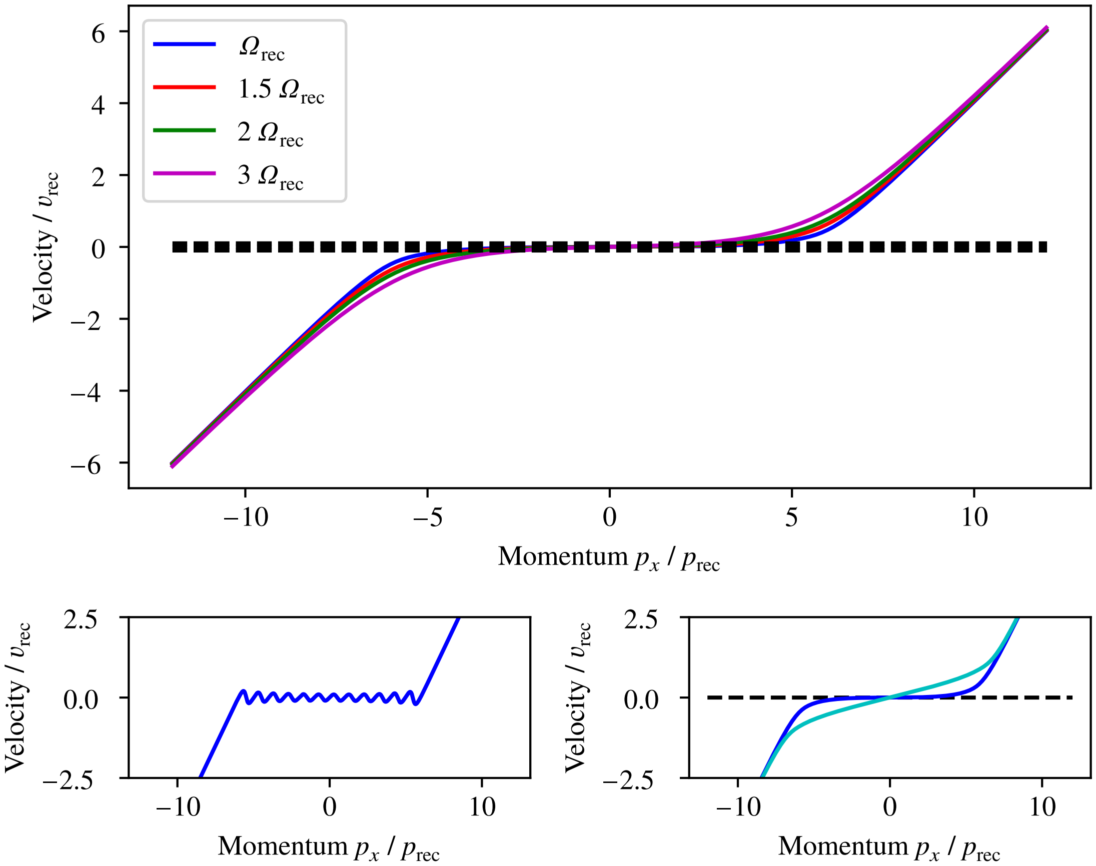

Figure 5.8: Top: calculated group velocities as function of the momentum p_x for different coupling strength. The dashed line marks the zero velocity line and has a width corresponding to $0.1\ v_{\text{rec}}$, which will be set as threshold value to define the bulk region (see section 5.3.1). Bottom, left: velocity as function of the momentum p_x for a coupling of $\Omega = 0.1\ \Omega_{\text{rec}}$. The fast oscillations on the lowest energy band in the dispersion relation are also visible in the velocity. Bottom, right: comparison of the velocities for a coupling of Ω_{rec} (blue) and $-\Omega_{\text{rec}}$ (cyan). Whereas the coupling of Ω_{rec} shows an almost dispersion less bulk, a coupling of $-\Omega_{\text{rec}}$ shows a clear and steep increasing velocity.

It has already been shown that the single photon detuning should be positive to have a nearly flat band and that the effective coupling strength should be $\geq \Omega_{\text{rec}}$ to suppress fast oscillation in the lowest and the first excited band. The top plot in fig. 5.8 illustrates the velocity as function of the momentum p_x for different coupling strengths. The coupling strength have been chosen according to the already determined range, which is possibly suitable for measurements. Whereas the velocities in the bulk, the almost flat regions in the dispersion relations, are similiar, clear differences appear at the edges (the side regions in which the energy is increasing in the dispersion relations). The difference between a coupling of Ω_{rec}, $1.5\ \Omega_{\text{rec}}$ and $2\ \Omega_{\text{rec}}$ is small compared to the difference to a coupling of $3\ \Omega_{\text{rec}}$. Therefore, later experiments will use an effective coupling in the regime of $1.5\ \Omega_{\text{rec}}$ due to the large bulk area and no fast oscillations on the two lowest bands. Even if the effective coupling strength would fluctuate within $\Delta\Omega \pm 0.5\ \Omega_{\text{rec}}$ fast oscillations on the bands are suppressed and the velocity distribution will only show small changes.

5.3.1 Edge - Bulk border

Looking more closely the dispersion relations for the SOC system show a curvature inside the bulk region whereas the Landau levels of an electron system show a flat bulk, as shown in fig. 4.3. Therefore only in the very centre for a vanishing momentum the velocity also vanishes completely in die spin-orbit coupled system. Moreover the energy separation between the bands is not constant for different momenta p_x and has an influence on measurements, which includes excitation in the first excited band. The deviations from an electron Landau system are, in the scope of this thesis, negligible. Nevertheless a definition of the bulk and edge regions is necessary to quantify the size of the bulk. For this purpose the bending of the lowest band is depicted in fig. 5.9 (left) for a coupling of $\Omega = 1.5\,\Omega_{\text{rec}}$. The corresponding velocity is shown on the right hand side. To define the bulk region a threshold velocity of $0.1\,v_{\text{rec}}$ has been chosen as depicted in fig. 5.9, meaning that all momentum p_x states with a velocity smaller than $0.1\,v_{\text{rec}}$ are counted as bulk states. Figure 5.10 shows the bulk size in momentum space as function of the effective coupling. Additionally table 5.1 gives the bulk size for suitable coupling strengths.

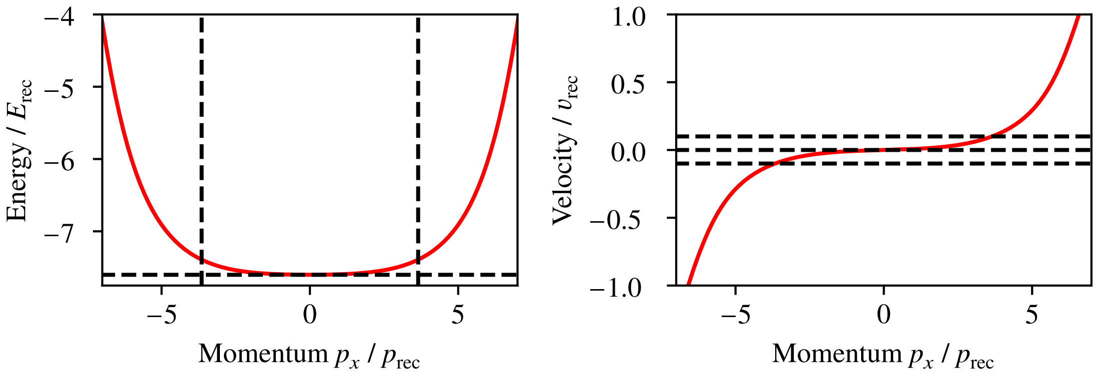

Figure 5.9: Left: in contrast to a real Landau system the dispersion relations from the SOC Hamiltonian show a slight bending, here illustrated for a coupling of $\Omega = 1.5\,\Omega_{\text{rec}}$. The vertical dashed lines mark the momenta p_x which correspond to a velocity of $0.1\,v_{\text{rec}}$. Right: corresponding velocity. The dashed lines mark a velocity of $0.1\,v_{\text{rec}}$.

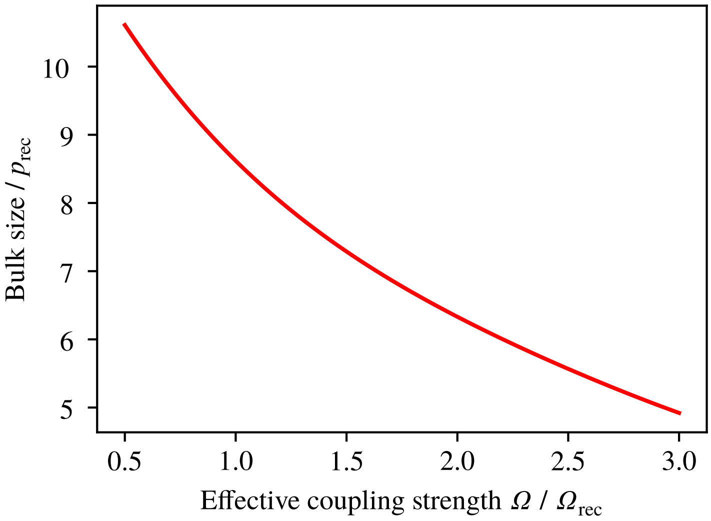

Figure 5.10: Bulk size as function of the effective coupling strength Ω. The bulk size is here the region in which the group velocity is smaller than $0.1\, v_{\mathrm{rec}}$. With increasing coupling the bulk size decreases.

Table 5.1: Approximate bulk sizes in momenta p_x. With increasing coupling strength the bulk size shrinks. The bulk size is not following the coupling strength in a linear manner.

Effective coupling strength	$1\ \Omega_{\mathrm{rec}}$	$1.5\ \Omega_{\mathrm{rec}}$	$2\ \Omega_{\mathrm{rec}}$
Bulk size	$\approx 8.6\, p_{\mathrm{rec}}$	$\approx 7.3\, p_{\mathrm{rec}}$	$\approx 6.3\, p_{\mathrm{rec}}$

5.4 Synthetic Hall mobility

The Hall mobility was introduced earlier and describes the transversal reaction of the system to an external force. To account for such an effective force, the Hamiltonian in eq. 5.19 can be extended [45]

$$H_p = H_{\mathrm{SOC}} - \hbar\delta\hat{J}_z \tag{5.22}$$

via the detuning δ, i.e. the effective force along the synthetic dimension can be determined to be

$$F_{\mathrm{eff}} = \hbar\delta. \tag{5.23}$$

From the perturbed Hamiltonian in eq. 5.22 the velocity and the mobility can be determined to be [45]

$$\langle v_{\mathrm{p}}\rangle = \langle v_0\rangle + \mu\hbar\delta \tag{5.24}$$

with the mobility μ given by

$$\mu_{\mathrm{SOC}} = \frac{1}{2\hbar k}\left(\frac{\partial}{\partial p}(m\langle v\rangle - p)\right), \tag{5.25}$$

where $\langle v_0 \rangle$ is the velocity without applying an external force. As calculated in section 5.3 the velocity vanishes in the unperturbed scenario for the bulk region. Therefore, the mobility can be determined to be

$$\mu_{\text{SOC,Bulk}} = -\frac{1}{2\hbar k} \tag{5.26}$$

in the bulk region. From the SOC Hamiltonian in eq. 5.21, $2\hbar k$ was identified with eB from the Landau Hamiltonian in eq. 5.20 which, inserted into μ_{SOC} gives the expected bulk mobility of $\mu = -(eB)^{-1}$ derived in section 4.1 for an electron Hall system. This fact nicely shows the coherent mapping between the SOC system and an electron Landau system.

Figure 5.11 shows a plot of the theoretical expected mobility for an effective coupling strength of $1.5\ \Omega_{\text{rec}}$ as function of the momentum p_x. For the bulk region the mobility is near $(p_{\text{rec}})^{-1}$ and decreases towards 0 for edge states. The position in the synthetic dimension is given by the colour map.

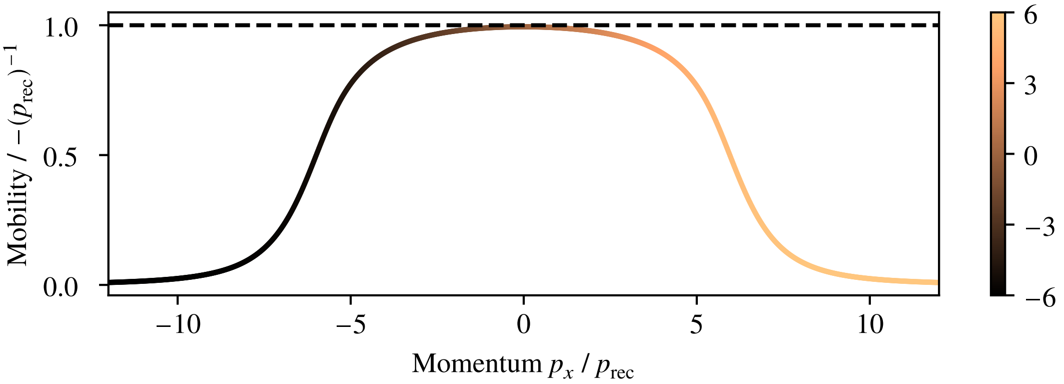

Figure 5.11: Theoretical mobility for a SOC system with an effective coupling strength of $1.5\ \Omega_{\text{rec}}$. The colour map gives the position in the synthetic dimension. In the bulk the mobility reaches the expected value of $(p_{\text{rec}})^{-1}$. Towards the edges the mobility is decreasing until vanishing completely.

5.5 Local Chern marker of the synthetic system

To show that the SOC system mimics an electron quantum Hall system with non trivial topology the local Chern marker which was introduced in section 4.3.3 can be derived for the SOC system. The SOC coupled system will be realised with erbium atoms, which have 13 m_j Zeeman levels in the electronic ground state, and correspondingly hard edges in the synthetic dimension. Hence, the definition of the LCM is necessary. The LCM for a SOC system is known and a detailed derivation for a stripe or ribbon geometry can be found in [45].

The starting point is the already introduced LCM from section 4.3.3 eq. 4.37:

$$c(x,y) = -i2\pi \langle x,y| \left[\hat{P}\hat{x}\hat{P}, \hat{P}\hat{y}\hat{P}\right] |x,y\rangle\,, \tag{5.27}$$

but this time the coordinate y is exchanged for the synthetic coordinate m_j and the corresponding operator $\hat{J}_z$

$$c(x,y) = -i2\pi \langle x,m_j| \left[\hat{P}\hat{x}\hat{P}, \hat{P}\hat{J}_z\hat{P}\right] |x,m_j\rangle\,. \tag{5.28}$$

The following derivation is analogous and yields

$$c(m_j) = \frac{1}{2\hbar k}\int dp\,\Pi_{m_j}(p)\frac{\partial}{\partial p}\left(p - mv(p)\right) = \int dp\,\Pi_{m_j}(p)\,\mu_{\mathrm{SOC}}(p), \tag{5.29}$$

with Π_{m_j} the spin projection probability which is as all other variables experimentally accessible. For the integration domain all momentum states with an energy lower or equal to the lowest band energy plus half the gap energy between lowest and first excited band for a momentum state of 0 are chosen. Figure 5.12 shows the theoretical expected LCM for an effective coupling strength of 1.5 Ω_{rec}. The bulk shows a value near 1 as expected. In this regime the distance to the edges is sufficient to show local properties similar to an infinite system. Towards the edges the LCM gets reduced to close the gap between vacuum and system [84].

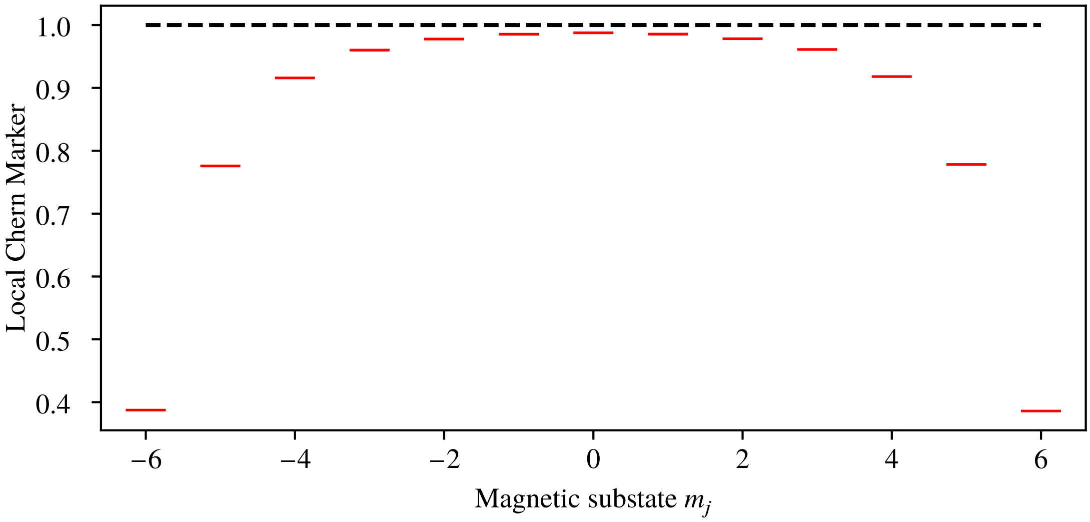

Figure 5.12: Local Chern marker as function of the synthetic dimension encoded in the magnetic sub levels m_j for an effective coupling strength of 1.5 Ω_{rec}. The integration domain includes all momentum p_x values whose energy is below the energy of half the energy gap between the first two bands plus the energy of the ground band for a momentum p_x of $p = 0$. Inside the bulk the LCM takes the value of the topological protected Chern number of 1.

CHAPTER 6

Experimental realisation of artificial gauge fields with ultracold erbium atoms

This chapter will first introduce the experimental setup used to realise the artificial quantum Hall system with ultra cold erbium atoms, followed by characterising measurements in preparation of spin-orbit coupling. The SOC is realised by optical Raman transitions tuned to near the erbium 841 nm narrow line transition. Experimental results for the artificial quantum Hall system will be presented and details on the underlying measurement routines are given.

6.1 841 nm Laser setup

The laser setup providing the laser light near 841 nm is shown in fig. 6.1. A Coherent Inc. MBR-110 Titan:Saphir (Ti:Sa) laser system which is optically pumped by a Coherent Inc. Verdi V18 provides typically an output power of around 3 W at a wavelength near 841 nm. After passing an optical isolator the beam is divided into two parts: One part is going to the wavemeter and the spectroscopy set up. The remaining light is used for the optical Raman manipulation. The frequency of the light can be shifted by acousto optical modulators (AOM) driven by an arbitrary waveform generator [1]. Since the later introduced functions are rather complex and functions which will become relevant in the future are even more complicated, an arbitrary waveform generator is necessary. The laser light is guided to the main chamber via polarisation maintaining optical fibres. To ensure a proper polarisation polarising beam splitters in rotary mounts are used in front of the fibres. Fast switching of the light is done with the AOMs. To block any light coming through the fibre additional mechanical shutters are used.

6.2 Optical Raman Setup at vacuum chamber

Due to the limited number of access windows of the chamber the Raman light beams have to be on the same axis as one of the MOT beam pairs, see fig. 6.2. To realise this dichroic mirrors are used. One Raman beam path is realised using a long pass, the other using a short pass dichroic mirror. This restriction is due to limitations in the optical setup around the main chamber. Both Raman beams are focused by the fibre outcouplers into the atom cloud to a diameter of $\approx 280\,\mu\text{m}$. A typical size of the atomic BEC

---

[1] Keysight 33612A

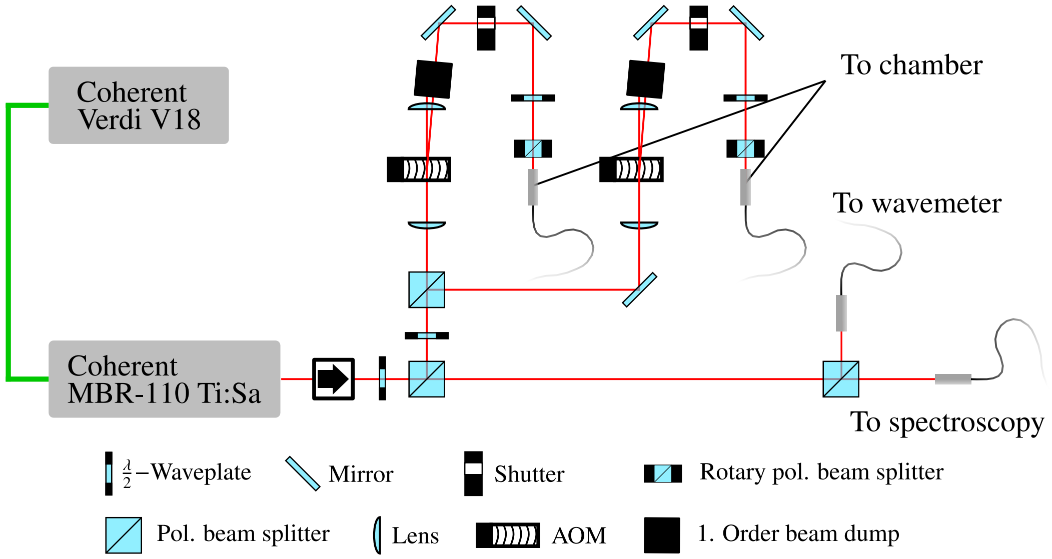

Figure 6.1: Setup which provides the experiment with light near 841 nm. The light source is a Titan:Saphir laser. The light is divided into several parts to be distributed for different purposes. Fast switching for the optical Raman manipulation is done with AOMs. Additional mechanical shutters block stray light.

cloud is $\approx 10\,\mu\text{m} \times 5\,\mu\text{m}$, which is much smaller than the diameter of the Raman beams and justifies a plane wave approximation. After each fibre a half waveplate is followed by a polarising beam splitter to assure a stable polarisation. The polarising beam splitter is followed by another half waveplate, which has its optical axis in an 22.5° angle with respect to the linear polarisation after the pol. beam splitter. The quantisation axis is along the z-direction. Therefore, the light is a superposition of σ_+, σ_- and π polarised light, which is necessary for the later realised SOC. Two photodiodes capture small amounts of 841 nm light, which passes through mirrors and is used to monitor the power of the two Raman beams. Each beam has a maximum power of $\approx 800\,\text{mW}$.

6.3 841 nm - Transition

The optical Raman coupling which was introduced in section 5.1 needs a suitable transition. The work presented in this thesis uses a narrow line transition near 841 nm. In order to work with this transition the laser needs to be reliably set to the corresponding frequency. Due to the weak transition an absorption spectroscopy using a hollow cathode lamp was not possible. A fluorescence spectroscopy was set up instead in a master thesis [90] to find the transition.

6.3.1 Spectroscopy

The spectroscopy setup is placed at the position of the transversal cooling stage and was realised in a master thesis [90]. Light with a wavelength near the 841 nm transition is guided through the atomic

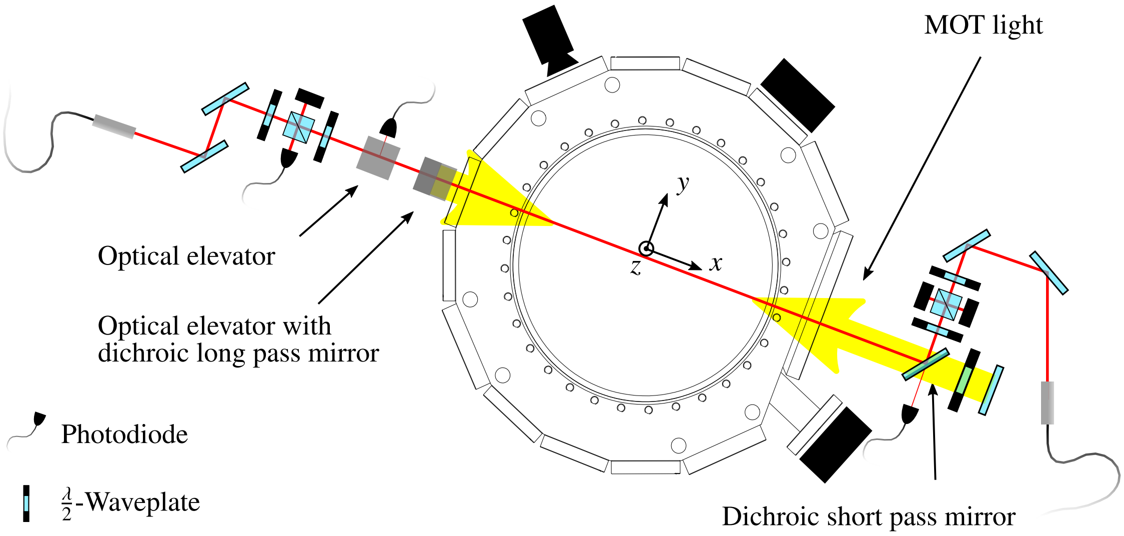

Figure 6.2: Optical set up at the chamber to realise optical Raman coupling. The optical power in the beam path are monitored by stray light which passes through mirrors. One of the MOT beam pairs and the Raman beam pair have to be on the same axis due to the restricted number of access windows. The underlying technical drawing was kindly provided by the “Feinmechanik-Werkstatt des Instituts für Angewandte Physik”

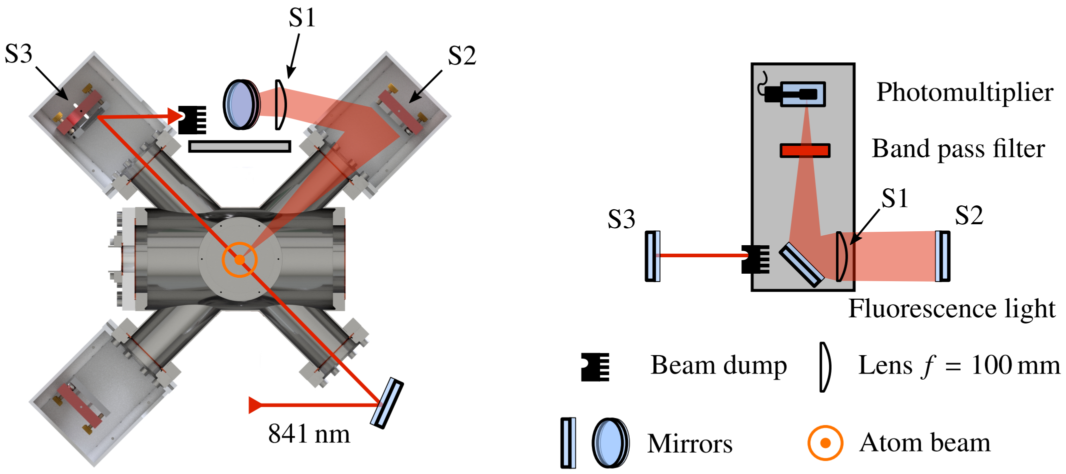

Figure 6.3: Spectroscopy setup at the position of the transversal cooling stage. Left: a cut through the setup showing the beam path through the transversal cooling stage. The probe light passes the atomic beam before it is captured in a beam dump. The fluorescence light is captured through another window by a PMT. Right: spectroscopy setup from above. Figure taken and modified from [90].

beam once before it is going into a beam dump, see fig. 6.3. An estimated fraction of 0.15 % of the emitted light is captured onto a photomultiplier tube (PMT). To reduce noise a band pass filter with centre frequency (840 ± 2) nm and full width half maximum of 10 nm is placed in front of the PMT. The laser light is chopped at a frequency of 1 kHz and frequency scanned over a total range of (4.2 ± 0.1) GHz. The frequency scan follows a sawtooth function with a frequency of 0.155 Hz. The PMT's signal is fed into a lock-in amplifier and the final data is an average over 64 scanning cycles.

Figure 6.4 shows measured data. The positions of the visible resonances of Er^{166}, Er^{168} and Er^{170} are determined by a fits with Gaussian functions. The absolute peak position in terms of the exact wavelengths could not be determined. The distances between the peaks were determined to be (1.38 ± 0.08) GHz between the Er^{166}-Er^{168} isotopes and (1.35 ± 0.08) GHz between the Er^{168}-Er^{170} isotopes and are in agreement with the literature values given by (1.433 ± 0.001) GHz (Er^{166}-Er^{168}) and (1.476 ± 0.002) GHz (Er^{168}-Er^{170}) [91]. The used optical power was approximately five times the saturation intensity and therefore a power broadened line of $\approx$ 5 MHz was expected. The extracted linewidth by means of the FWHM value was found to be $\approx$ 41 MHz and therefore $\approx$ 8 times the expected power broadened line. Other broadening effects could include a transversal velocity of the atoms in the dimension of the spectroscopy laser beam light or a drift in the laser frequency.

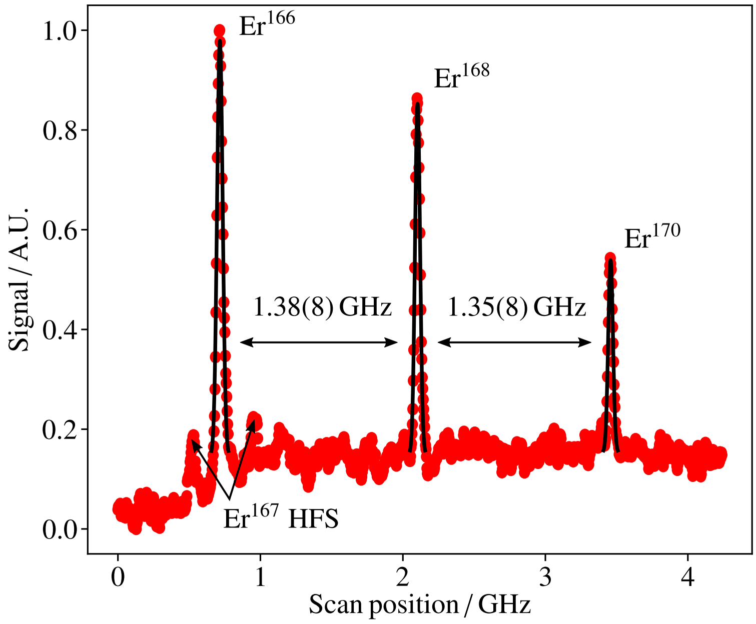

Figure 6.4: Fluorescence signal of the spectroscopy setup realised at the position of the transversal cooling stage. The three isotopes with the highest abundance can clearly be observed. The hyperfine structure of Er^{167} can also be observed. The fit functions are Gaussian functions with an offset.

6.3.2 Frequency stabilisation of the Titan:Saphir laser

The 841 nm laser system is frequency stabilised using a digital proportional-integral-derivative (PID) controller provided by the wavemeter. The wavemeter is a High Finesse WS7-60 with an absolute accuracy of 60 MHz. In the range of 800 to 1 180 nm the absolute accuracy is given as 50 MHz or not better than 20 % of the laser linewidth. The optical Raman manipulation will be realised with a large detuning of about 10^5 to 10^7 natural linewidths of the transition corresponding to an absolute detuning of 0.8 to 80 GHz.

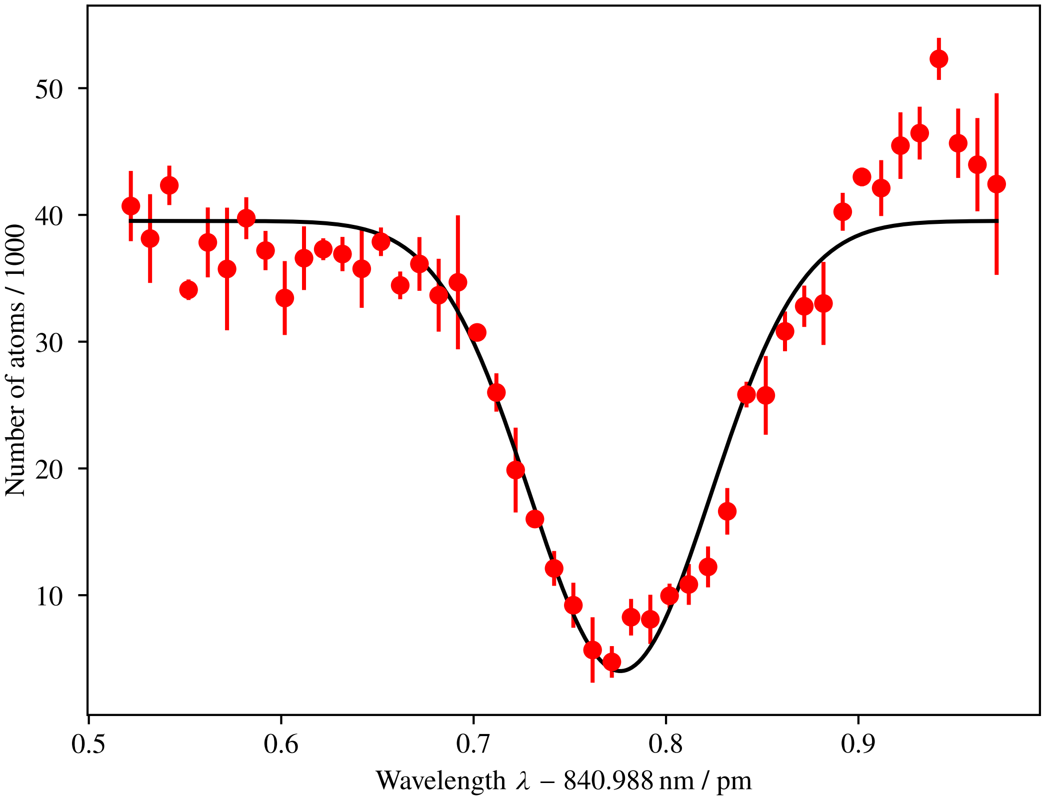

Figure 6.5: Number of atoms as function of the wavelength used for the laser light pulse to find the transition wavelength for later experiments. The wavelength is stabilised using a digital PID controller of a High Finesse WS-7 60 wavemeter.

Therefore, the accuracy and the locking mechanism of the wavemeter is suitable.

Figure 6.5 shows experimental data to find the resonance wavelength for the 841 nm transition in air as a marker for further measurements, which include optical manipulation. For the measurement a BEC is prepared and one of the Raman beams is blocked. A 200 µs pulse with ≈ 160 mW is illuminating the BEC and the number of atoms is determined after a time of flight of 15 ms. In fig. 6.5 the number of atoms as a function of the wavelength in air can be seen.

The fit function in fig. 6.5 is a dip with a Gaussian distribution. The resonance in air is found at 840.988776 nm with a standard deviation width of 0.000047 nm corresponding to ≈ 20 MHz. The measured linewidth is therefore approximately 2500 times bigger than the natural linewidth. The laser pulse length of 200 µs only corresponds to a spectral width of 5 kHz. The doppler broadening corresponding to the temperature of the atoms is estimated to 4 kHz. It can be concluded that other, most likely the saturation broadening effects are present.

In this thesis a positive effective coupling was realised by setting the laser wavelength in air to 840.985 nm

[2] corresponding to a positive detuning of $\approx 2.0 \times 10^5\, \Gamma_{841} \approx 1.6\,\mathrm{GHz}$. For a negative effective coupling the laser was frequency stabilised to a wavelength of 840.99165 nm corresponding to a detuning of $\approx -1.5 \times 10^5\, \Gamma_{841} \approx -1.2\,\mathrm{GHz}$. The uncertainty of ≈ 20 MHz is therefore negligible.

6.3.3 Magnetic field

To experimentally realise and control the Zeeman splitting of the ground state, which is necessary for SOC, magnetic bias coils are installed, see section 3.1.4. The magnetic stray fields were compensated by carefully determining the magnetic fields in all three spacial directions. For this, a spin polarised [3] BEC was prepared and subsequently probed by a radio pulse with variable frequency. The remaining number of atoms in the $m_j = -6$ Zeeman state was measured from which the resonance frequency was determined [4]. By changing the currents through the bias coils the resonance frequency was reduced to $(0 \pm 30)\,\mathrm{kHz}$, corresponding to a residual magnetic field of 50 mG.

The magnetic guiding field realising the Zeeman splitting should be much larger than the remaining uncompensated bias fields, while still being small enough such that the quadratic Zeeman effect is negligible. The latter shifts the resonance condition for the different Raman transitions and a transfer into other Zeeman states can be suppressed. The relative effect of the remaining magnetic stray fields is minimised by choosing larger guiding magnetic field strengths. A magnetic field of ≈ 500 mG corresponding to a Zeeman splitting of ≈ 300 kHz showed to be a suitable value for the experiments presented in the next sections.

The relative strength between the polarisation components of the light is directly connected to the magnetic field direction which should be along the z-direction. An imperfect magnetic field direction will lead to unequal parts of π, σ_+ and σ_- polarisation components.

Another important aspect is the magnetic field stability. To estimate the magnetic field fluctuations a magnetic fluxgate sensor [5] was placed near the chamber and used to measure the magnetic field, which is present during the SOC. A fluctuation by means of the standard deviation of 0.9 mG was determined.

The Zeeman splitting was measured on a daily basis by means of a RF-frequency scan [6] to include day to day drifts in the magnetic fields since no active control loop was used for the measurements presented later in this chapter.

6.4 Sample preparation

All the experimental procedures presented in the following start after the preparation of a spin polarised ($m_\mathrm{J} = -6$) BEC followed by the experimental realisation of spin-orbit coupling with erbium. After the forced evaporative cooling the atom cloud is held for 500 ms inside the ODT. In the last 250 ms the magnetic bias coils are ramped in 100 ms to a value such that magnetic fields in x- and y-direction are compensated and a known field in z-direction is present at the position of the atomic ensemble. After the BEC is prepared in a defined magnetic field the optical dipole traps are switched off, followed by a waiting time of 20 µs before the Raman beams are switched on.

---

[2] Including the 200 MHz shift from the AOM this corresponds to ≈ 840.9845 nm.

[3] The MOT loading results in all atoms in the $m_j = -6$ Zeeman state. The spin polarisation is kept through the preparation of the BEC.

[4] The resonance frequency is the frequency for which the remaining number of atoms in the $m_j = -6$ Zeeman state is minimised.

[5] Stefan Mayer Instruments, FLC 100

[6] The BEC was probed by radio frequency pulses of fixed length but varying frequency.

6.5 Effective coupling strength

The effective coupling strengths were determined for the used Raman beam intensities either before or after measurements to include day to day drifts [7]. The frequency difference ω_{12} between the two Raman laser beams was set according to the Zeeman splitting and the atoms were probed with Raman pulses. The laser pulse excites a coherent superposition of eigenstates of the system, which evolves in time. To determine the effective coupling strength the oscillation period of the magnetisation as a function of the pulse length was determined. Figure 6.6 shows the average m_j state as a function of the Raman pulse length with a cosine fitted to the experimental data.

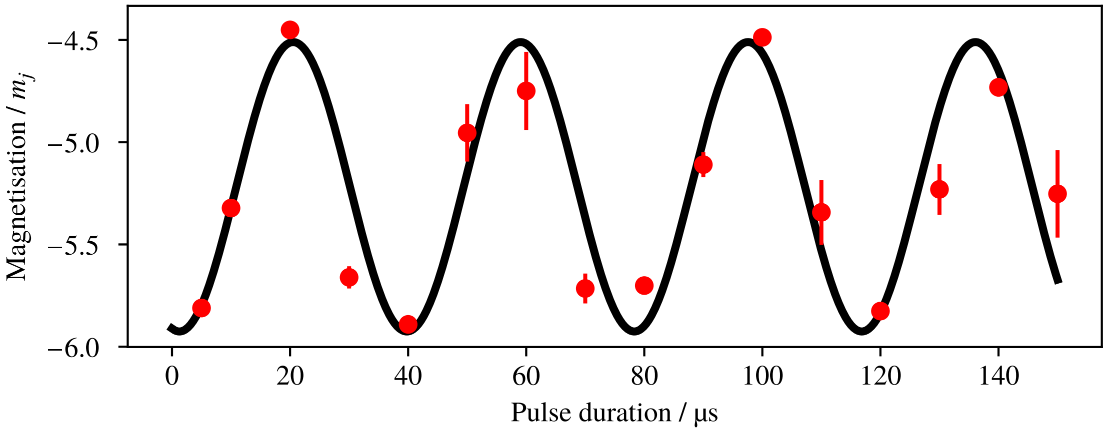

Figure 6.6: Measurement to determine the effective Raman coupling strength. The Raman beam frequency difference is set to the two photon resonance (corresponding to the Zeeman splitting) and the atoms are illuminated by Raman pulses with different pulse lengths. An oscillation with a frequency corresponding to the energy gap between the lowest band and the first excited band can be observed from which the effective two photon coupling Ω can be determined. In the here shown data the oscillation corresponds to an effective coupling strength of $(1.44 \pm 0.01)\ \Omega_{\text{rec}}$

The oscillation frequency corresponds to the energy gap $E_g = h\nu_g$ between the lowest and first excited band for a momentum p_x of $-6\,p_{\text{rec}}$. To derive the effective coupling strength Ω the theoretical energy gaps were calculated as a function of the effective photon coupling strength for the momentum p_x state $-6\,p_{\text{rec}}$. Figure 6.7 shows the effective coupling strength as a function of the energy gap. For the effective coupling strength in fig. 6.6 follows $(1.44 \pm 0.01)\ \Omega_{\text{rec}}$. Since the effective coupling strength is only used to calculate theoretical dispersion relations, a closer error analysis has not been done and the given errors consist only of the fitting uncertainties. Small differences in the coupling strength only have little effect, as will be shown in section 6.6.2. Other means of calibration of the coupling strength should be used if the knowledge of the exact coupling strength is crucial. The method used in [45] which worked by observing the atoms reaction to a laser beam pulse by one of the Raman laser beams onto the atomic cloud could not be realised at this experiment due to the relative positions of Raman laser beams and camera system to one another.

---

[7] The beam alignment was checked and optimised on a daily basis.

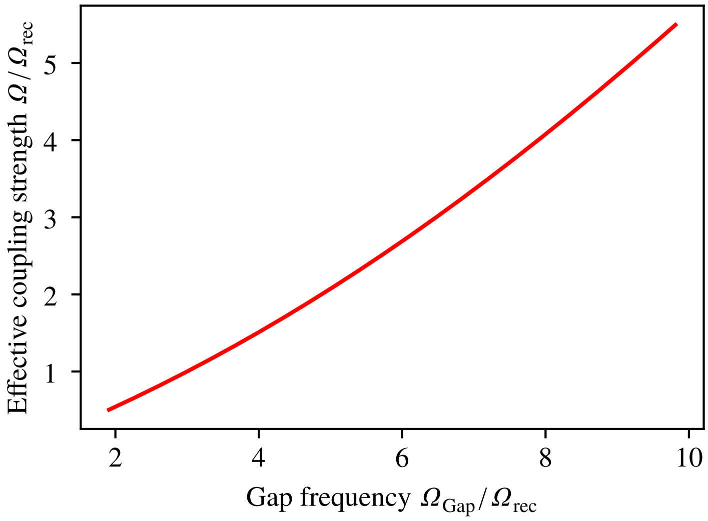

Figure 6.7: Calculated two photon coupling as function of the energy gap between the lowest and the first excited band from Hamiltonian 5.19 for a momentum p_x of $-6 p_{\mathrm{rec}}$.

6.6 Dispersion relations - Group velocities

6.6.1 Experimental procedure

Artificial magnetic fields manifest into a disperionless bulk in the dispersion relation, corresponding to section 5.2. Therefore, the first experimental observations are measurements of the group velocities in the lowest band to confirm a flat dispersion relation.

An atom cloud is prepared as introduced in section 6.4 and the Raman laser beams are adiabatically switched on after a waiting time of 20 µs after turning off the ODTs. The adiabatic increase in laser power ensures that the atoms are not excited to higher energy levels and stay in the lowest level. The intensity ramp takes 150 µs in an exponential form and was found empirically by means of no change in the atomic cloud after ramping up the Raman beams. Once the Raman beams are at the final power the detuning $\delta = \omega_{12} - \omega_z$ is changed to prepare a specific momentum p_x state. A sketch of the experimental routine for the Raman beams can be seen in figure 6.8. Starting with the momentum of the atom in the frame of the moving lattice

$$p_x = p_0 + m \frac{\delta}{2k} \tag{6.1}$$

with $p_0 = -6 p_{\mathrm{rec}}$ as the initial momentum state and $\delta / 2k$ the velocity of the lattice, it follows

$$\omega_{12}(p_x) = \omega_z + 2 \frac{E_{\mathrm{rec}}}{\hbar} \left(\frac{p_x}{p_{\mathrm{rec}}} + 6 \right) \tag{6.2}$$

for the frequency difference of the Raman laser beams as function of the momentum p_x.

In the experiment an initial frequency difference ω_{12} of $2\pi \times 245$ kHz is used. For a usual Zeeman splitting of $\omega_z = 2\pi \times 307$ kHz this corresponds to a prepared momentum state of $p_x \approx -10.5 p_{\mathrm{rec}}$. Other momentum states can be prepared by simply ramping ω_{12} to a different value. The frequency ramp has to

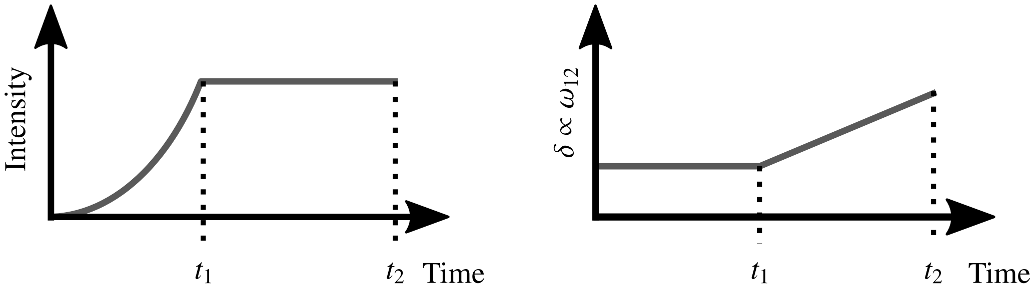

Figure 6.8: Left: intensity as function of time of the two Raman laser beams. The intensity is ramped up in an exponential form until $t_1 = 150\,\mu\mathrm{s}$. After the final intensity is reached the intensity is held until the end of the state preparation. Right: frequency difference ω_{12} between the two Raman laser beams. During the intensity ramp the frequency difference is kept constant at $\omega_{12} = 2\pi \times 245\,\mathrm{kHz}$. After the final intensity is reached at time t_1 the frequency is changed with a constant ramp to tune to the desired momentum state, see eq. 6.2.

be chosen carefully. Is it too fast the transfer is not efficient. Is it too slow on the other hand, unwanted scattering between atoms and Raman light leads to heating of the sample. Suitable frequency ramp rates depend on the coupling strength. For effective coupling strengths in the order of $\Omega = 1.5\,\Omega_{\mathrm{rec}}$ a ramp of $1\,\mathrm{kHz}\,\mu\mathrm{s}^{-1}$ showed to be a good trade-off between the effects.

Figure 6.9 shows a transfer efficiency measurement for an effective coupling strength of $\Omega \approx 1.3\,\Omega_{\mathrm{rec}}$ (left graph) and $\approx 3.9\,\Omega_{\mathrm{rec}}$ (right graph). The ramp time is chosen so that the atoms are transferred into a momentum state of $p \approx 10\,p_{\mathrm{rec}}$ corresponding to all atoms being in the $m_j = 6$ Zeeman state. Therefore, for each ramp rate the total ramp time is different. For a relatively weak coupling of $\approx 1.3\,\Omega_{\mathrm{rec}}$ it clearly can be seen that for ramp rates over $2\,\mathrm{kHz}\,\mu\mathrm{s}^{-1}$ the total magnetisation goes down, which means more atoms are in Zeeman states below $m_j = 6$. Is the ramp rate too fast the frequency change can be thought of as a frequency kick or quench, which excites atoms into a superposition of eigenstates resulting in an oscillation in the Zeeman levels. The total number of atoms is also affected. For ramps rates below $1\,\mathrm{kHz}\,\mu\mathrm{s}^{-1}$ or above $3\,\mathrm{kHz}\,\mu\mathrm{s}^{-1}$ significant atom loss is observed. For ramp rates below $1\,\mathrm{kHz}\,\mu\mathrm{s}^{-1}$ the atom loss can be explained by unwanted spontaneous scattering. For ramp rates over $3\,\mathrm{kHz}\,\mu\mathrm{s}^{-1}$ an atom loss is not expected. Hence, the smaller number of atoms are caused by other external influences. Increasing the coupling to $\approx 3.9\,\Omega_{\mathrm{rec}}$ (right graph) allows for faster ramp rates. This behaviour can be explained by the energy gap between different bands, see figure 6.7. A larger effective coupling strength leads to larger energy gaps and the non-adiabatic excitations get reduced as explained by the Landau-Zener effect.

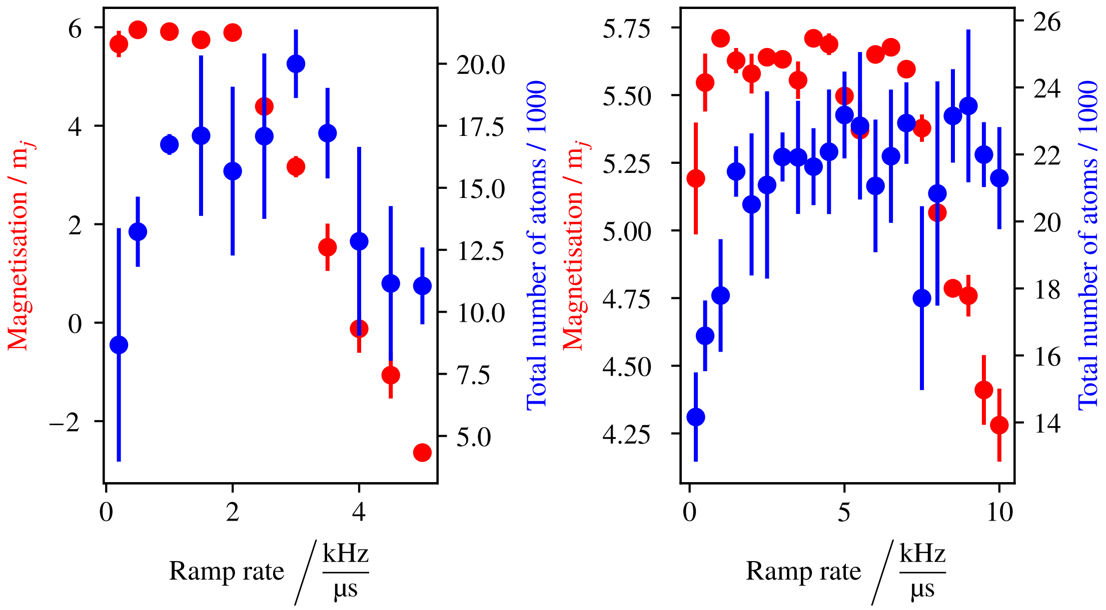

Figure 6.9: Magnetisation and total number of atoms at the end of the frequency ramp as function of the ramp rate, here for an atom-light coupling of ≈ 1.3 Ω_{rec} (left graph) and ≈ 3.9 Ω_{rec} (right graph). The total ramp time was chosen to theoretically transfer all atoms into the $m_j = 6$ Zeeman state. Left: the magnetisation goes down for ramp rates faster than 2 kHz μs^{-1}. The total number of atoms goes up until 1 kHz μs^{-1}. With faster ramp rates unwanted scattering is reduced. For ramp rates faster than 3 kHz μs^{-1} the number of atoms decreases unexpectedly, which can be explained by unwanted external influences. Right: compared to the weaker coupling in the left graph the ramp rates can be chosen faster, which can be explained by larger energy gaps between the different bands. For this measurement each ramp rate was measured 5 times and the shown data correspond to the average. The errors stem from the standard deviation from the 5 measurements.

With the ramp speed chosen the population of the 13 Zeeman states was measured as a function of the prepared momentum p_x state for different effective coupling strengths. As the starting point a momentum p_x state of ≈ $-10.5\,p_{\text{rec}}$ was chosen and each momentum state was measured 5 times.

The velocity of the atoms with respect to the reference frame of the moving lattice can be calculated by

$$\begin{aligned} v &= v_{\text{Atoms,lab}} - v_{\text{lattice}} && (6.3)\\ &= -(\langle m_j\rangle + 6)v_{\text{rec}} - \frac{\omega_z - \omega_{12}}{2k} && (6.4)\end{aligned}$$

with v_{rec} the velocity corresponding to the two photon momentum transfer and the average $\langle m_j\rangle$ the magnetisation. The velocity $v_{\text{Atoms,lab}}$ can be derived by the fact that the atoms are prepared in the $m_j = -6$ state and are at rest. If all atoms are transferred into $m_j = 6$ the atoms have a velocity of $12\,v_{\text{rec}}$ in the lab frame, since every transfer from m_j to m_{j+1} is accompanied by a velocity kick of v_{rec}. The velocity of the lattice is known to be the detuning divided by the wave number.

To measure the relative populations of the Zeeman states and determine the mean velocity of the atoms the just introduced scheme was implemented. After the preparation of the atoms in a well defined momentum p_x state the Raman beams are switched off abruptly and the atoms evolve for 12 ms in total in

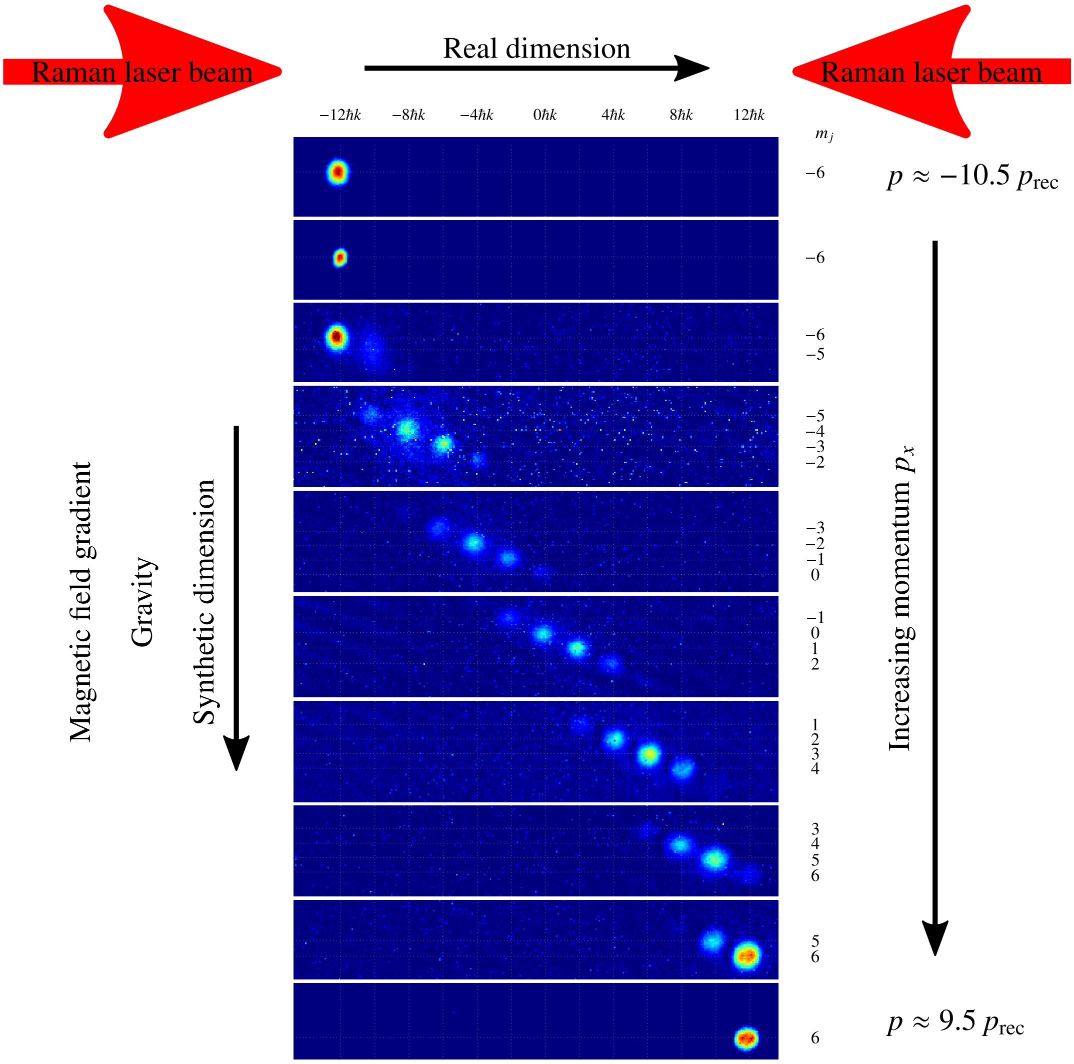

Figure 6.10: Series of absorption images taken for a group velocity measurement. Each slice is an average of 5 images. With change of the prepared momentum p_x the atoms are transferred through the synthetic as well as through the real dimension. The discrete positions in the synthetic dimension are given through the discrete internal Zeeman states and are separated in real space by a magnetic field gradient. The discrete clouds in the real dimension are caused by the momentum transfer from laser to atom in multiple of $2\hbar k$. Therefore, the system spans a lattice with 13 × 13 lattice sites. The colour scale in the images is not constant and the contrast is changing though the pictures for better visibility.

a time of flight measurement. During this time the magnetic field, which was present during the optical Raman manipulation is kept. After a time of flight of 2 ms an additional magnetic field gradient is applied to spatially separate the different m_j states and after further 10 ms time of flight an absorption image is taken. The relative number of atoms per m_j-state are determined as described in section 3.1.7. Figure 6.10 shows a series of absorption images taken for different prepared momenta p_x showing all positions in the synthetic dimension.

In the taken absorption images 13 regions of interest, corresponding to the 13 coupled states, are defined and the number of atoms in those regions are determined automatically. A problem of this method is that even if no atoms are present a false background count often appears [8]. Hence, a threshold number of atoms has been obtained for each data set individually. The magnetisation is known to be $\langle m_j \rangle = -6$ after the adiabatic increase of the intensity of the Raman beams, but shows values smaller than -6. The threshold value has been chosen to correct the initial magnetisation to $\langle m_j \rangle = -6$. Typical thresholds are in the regime of 300 atoms. With the threshold defined the average number of atoms in a m_j state is compared to the threshold value. If the average number of atoms is below the threshold the corresponding number of atoms are set to zero. Once the relative population are known the magnetisation $\langle m_j \rangle$ can be determined and with eq. 6.4 the velocity in the frame of the moving lattice can be calculated.

---

[8] The background correction, which is done in the analysis of the absorption images by subtracting a dark image and dividing through the flat image, does not get rid of vibrations. Therefore, the signal image and the flat image have effectively a slight difference in the area which is imaged. This leads to fringes on the final image which are falsely counted as atoms if falling into a region of interest. Unfortunately, the magnitude of this effect varies.

6.6.2 Velocity measurements

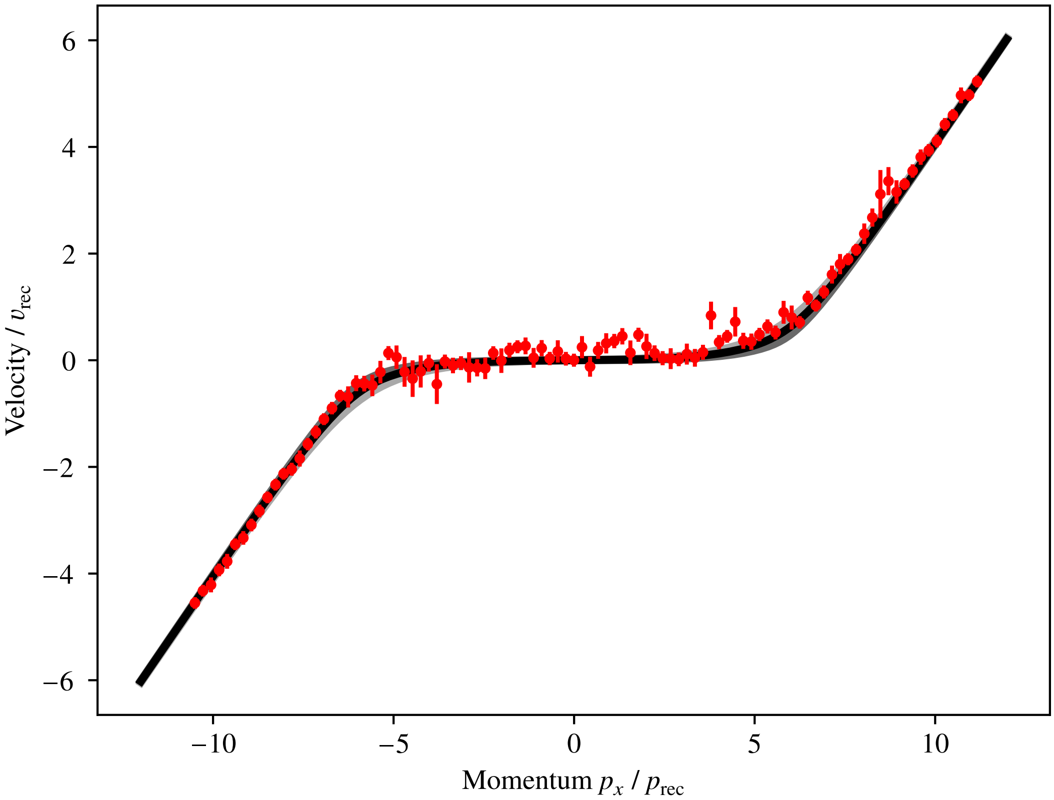

Figure 6.11: Measured group velocity as a function of the momentum p_x (red data points) and corresponding theoretical expectation for an effective coupling strenght of 1.44 Ω_{rec} (black line). The experimental data has been corrected by a threshold value, see text for more information. Additionally theoretical expectations for effective coupling strengths of 1 Ω_{rec} and 2 Ω_{rec} (gray) have been plotted.

The velocity measurements are compared to expectations. To obtain the theoretically expected dependence of the atomic group velocity the first derivative of the dispersion relation was calculated. Figure 6.11 shows a velocity measurement for a coupling of $(1.44 \pm 0.01)\ \Omega_{\text{rec}}$. The single photon detuning was set to $\approx 2.0 \times 10^5\ \Gamma_{841} \approx 1.6\,\text{GHz}$ as stated in chapter 6.3.2 and a beam power of $\approx 25\,\text{mW}$ has been used. The experimental data is shown in red whereas the expected group velocity is shown in black. The error bars stem from a statistical error (standard deviation) from measuring each point 5 times and the magnetic field fluctuations in the laboratory. It can clearly be seen that the measurement follows the expectation. In the centre a dispersion less bulk is observed whereas at the edges the expected edge modes with velocities of different direction are observed. Deviations, most clearly observed in the bulk, are attributed to magnetic field fluctuations and the resulting fluctuating occupation of the Zeeman states. The grey lines, which correspond to couplings of 1 Ω_{rec} and 2 Ω_{rec} also fit the experimental data and leads to the conclusion that the resolution of the experimental apparatus is to date not sufficient to distinguish different effective couplings in this regime of effective couplings. However, for the scope of this thesis this is also not necessary.

The effect of the used threshold (see end of chapter 6.6.1) is depicted in fig. 6.12. The left column shows the measured data before applying the threshold. The average magnetisation after the adiabatic increase of the Raman laser beam power is clearly greater than −6. A threshold of 300 atoms corrects this deviation. The effect is clearly observable in the group velocity as well.

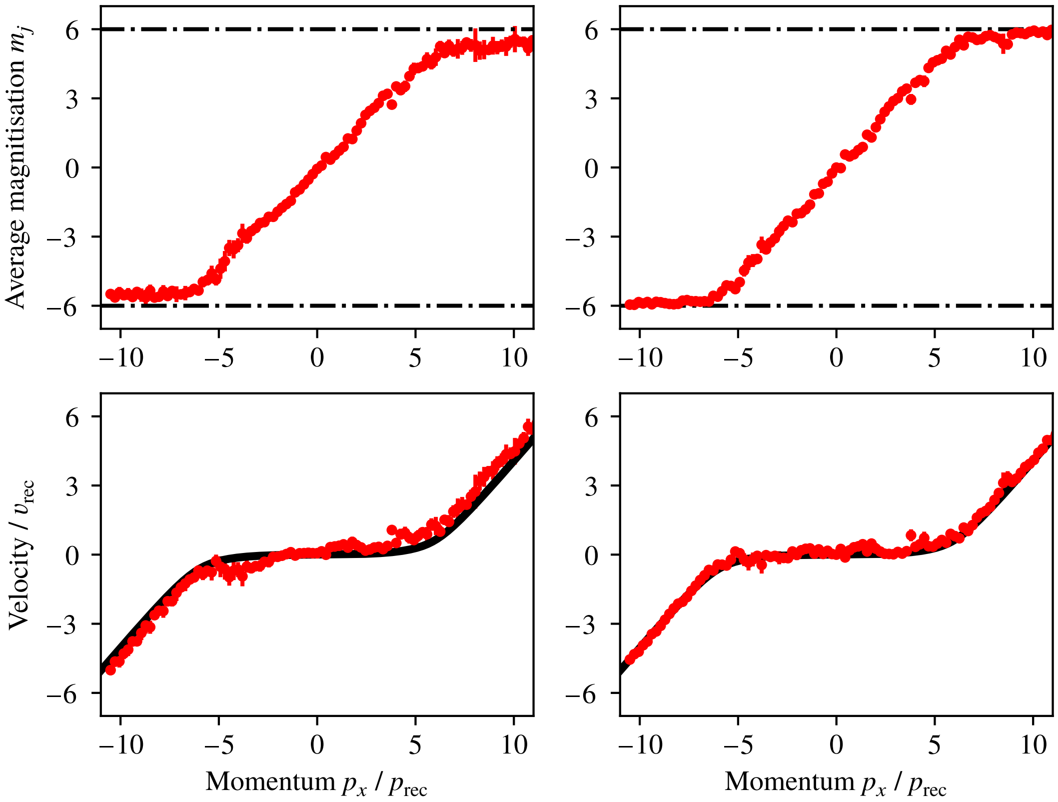

Figure 6.12: Defining a threshold value. Left column: uncorrected data. It can clearly be seen that even though experimentally all atoms are in $m_j = -6$ for momenta p_x below $\approx -6\,p_{\mathrm{red}}$ the magnetisation is reduced which results in an increased absolute velocity. Right column: if the average number of atoms in a m_j-state was below 300 atoms, the number of atoms has been set to 0.

Figure 6.13 shows velocity measurements for different used effective coupling strengths Ω and for a different geometry. The upper left graph shows a comparison for approximately the same coupling strength, but measured on different days. The measured group velocities show the expected behaviour, which confirms a stable running experiment. The observed deviation between measurements on different days can be attributed to fluctuations in the laboratory environment. Measurements with a coupling of $(4.11 \pm 0.03)\,\Omega_{\mathrm{rec}}$ (fig. 6.13, top-right graph) and a coupling of $(-0.96 \pm 0.01)\,\Omega_{\mathrm{rec}}$ (fig. 6.13, bottom-left graph) have been performed to investigate the expected dependence of the coupling strength. It is evident that both velocity measurements show no flat band behaviour despite the deviations from the expected velocity. The strong positive effective coupling shows a residual oscillation, which is attributed to an imbalance in polarisation. To demonstrate this effect clearly, the bottom-right graph in fig. 6.13 shows the group velocities for a non symmetric coupling by means of one Raman laser beam polarised in π-polarisation and the other in σ-polarisation. The deviations for the negative effective coupling is attributed to mode jumps of the Raman laser system, which occurred during the recording of this data as a result of a broken laser chiller.

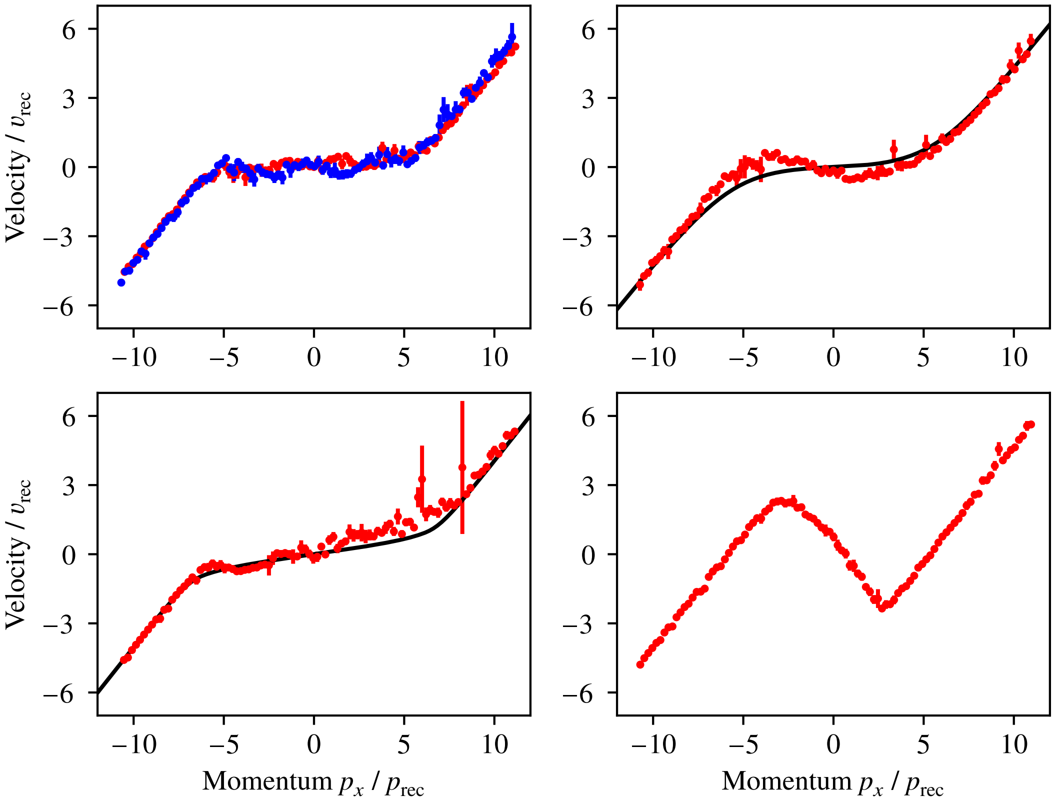

Figure 6.13: Upper left: two measurements with approximately the same coupling measured on different days. Red has a measured coupling of $(1.44 \pm 0.01)\ \Omega_{\text{rec}}$ and blue of $(1.42 \pm 0.01)\ \Omega_{\text{rec}}$. Upper Right: group velocities for a measured coupling of $(4.11 \pm 0.03)\ \Omega_{\text{rec}}$. Lower left: group velocities for a measured coupling of $(-0.96 \pm 0.01)\ \Omega_{\text{rec}}$. Lower right: velocity distribution for the non symmetric coupling case. One beam consists only of π, the other only of σ polarised light.

As already discussed in chapter 5.3, a wide range of coupling strengths show a flat dispersion in the lowest band. To verify this experimentally figure 6.14 shows a comparison between a coupling of $(1.44 \pm 0.01)\ \Omega_{\text{rec}}$ (red data points) and $(0.89 \pm 0.01)\ \Omega_{\text{rec}}$ (blue data points). The data shows no clear difference within experimental uncertainties. On the one hand this behaviour is preferable since small changes in the coupling should show no to little influence in measurements over several hours. On the other hand the differences may be small in the velocity measurements but could have larger influence on other measurements, e.g. the orbital measurements shown in the next section.

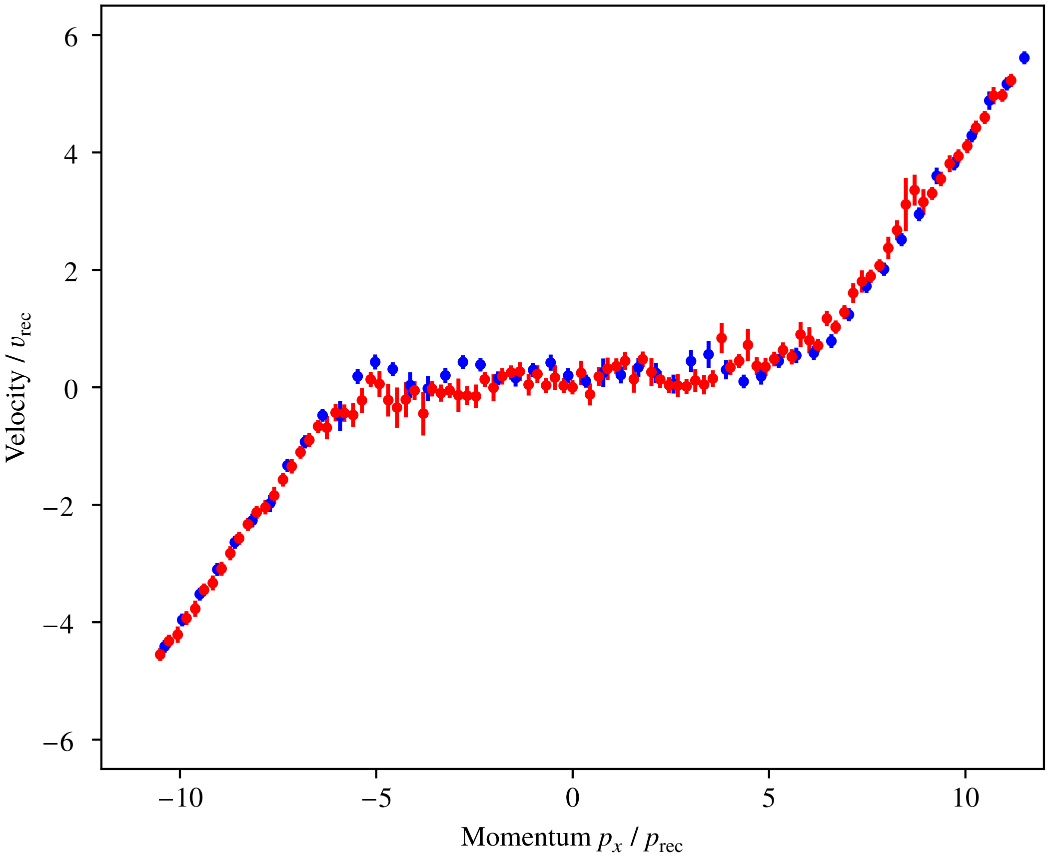

Figure 6.14: Comparison between experimentally determined group velocities with an effective coupling of $(1.44 \pm 0.01)\ \Omega_{\mathrm{rec}}$ (red data points) and $(0.89 \pm 0.01)\ \Omega_{\mathrm{rec}}$ (blue data points).

It can be concluded that the setup is able to realise different coupling schemes and strengths. The experimental data meets the expectations to good accuracy in the for this thesis relevant coupling regime and shows an almost dispersionless bulk region.

6.7 Cyclotron Orbits

A Hall system with charged particles shows characteristic trajectories as introduced in section 4.1 and shown in fig. 4.1. Similar trajectories can be observed in the synthetic Hall system by preparing the atoms in a coherent superposition of eigenstates. The presentation of the following measurements uses a colour map used to illustrate the time evolution. The time is proportional to the colour: White is always the starting point at time 0 all the way to red which is the last measurement. The time steps are constant at 4 µs. Figure 6.15 shows the ramp of the two photon detuning used to observe cyclotron orbits. The sample is prepared in a specific momentum p_x state identical to the state preparation for the velocity measurements. A frequency quench by $(\Omega_{\mathrm{rec}}/\pi)$ kHz, corresponding to a velocity kick of v_{rec}, is applied at time t_2 as shown in the graph [9]. The sudden quench results in the atoms not being able to follow an eigenstate of the system and are therefore in a coherent superposition of eigenstates, which evolves over time and oscillates between the lowest and the first excited band with the frequency corresponding to the energy gap. The classical analogue to the frequency which correspond to the energy gap would be the cyclotron frequency.

In the experiment the frequency is held for a variable holding time $t_h = t_3 - t_2$ before the Raman lasers are turned off. The following time of flight procedure allows to determine the magnetisation as function of the holding time.

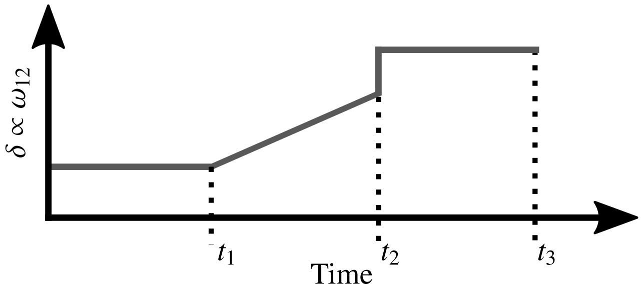

Figure 6.15: Frequency difference ω_{12} (effective detuning) as a function of time to excite cyclotron orbits in the artifical quantum Hall system. Until t_2 the sample is prepared in a specific momentum p_x state before a frequency quench at time t_2 is applied. The Raman lasers are turned of at time t_3.

Bulk

For an electron two-dimensional Hall system it is expected that particles move on a closed circle inside a two dimensional plane in absence of any additional force. Figure 6.16 shows an equivalent in the implemented synthetic Hall system. The measurement was performed for an effective coupling of $\approx 1.2\,\Omega_{\mathrm{rec}}$ and a prepared momentum p_x state of $p = 0$. The left graph of figure 6.16 shows the magnetisation as a function of the holding time.

---

[9] The frequency quench is realised by changing the frequency of one Raman laser abruptly at time t_2 changing ω_{12} and thus effectively changing the detuning δ.

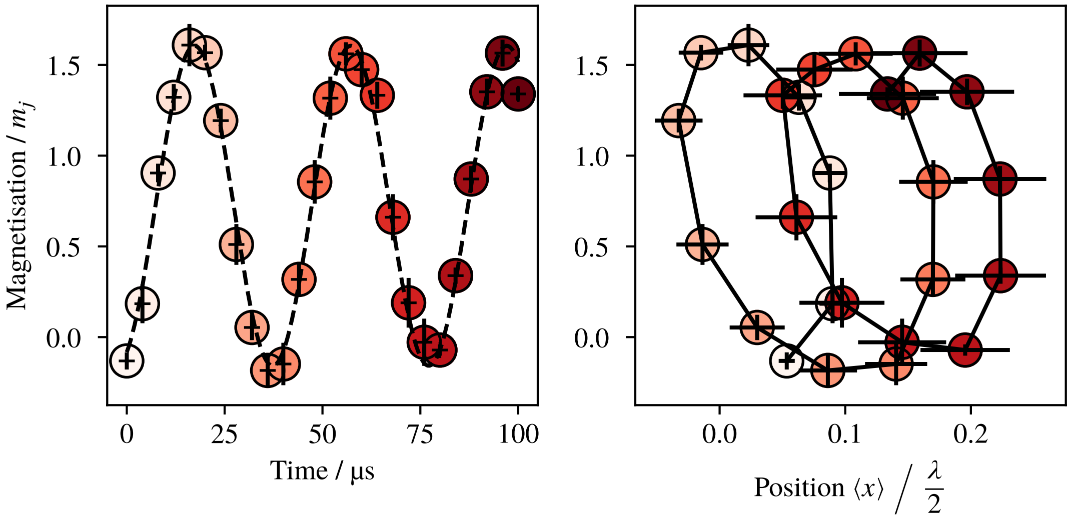

Figure 6.16: Left: time evolutions of the magnetisation after a velocity kick realised by a frequency quench. The colour of the points is proportional to the time. Right: the same data as shown in the graph on the left but as a function of the real space position obtained by integrating over the velocity.

The right graph of figure 6.16 shows the same data with the time converted into a real space position. The velocity for each holding time t_h is calculated and integrated over time which gives the average covered distance by the atoms. Interpreting the magnetisation as a synthetic spatial dimension allows to plot the two-dimensional plane, the magnetisation as one dimension and the real space position as second dimension, shown in fig. 6.16.

Against expectations, the atoms are here observed to follow the trajectory of a drifting orbit. The drift is attributed to drifts of the magnetic field. As stated before, variations of the magnetic field have an influence on the determined velocities. For the velocity measurements, fluctuations in the external magnetic fields only result in relatively small differences in the calculated velocities, whereas when the velocity is integrated to a position, small deviations already show up in non closed orbits.

To estimate the underlying magnetic drift and justify the assumption that external magnetic field drift are the reason for the drifting orbit, the Zeeman splitting, for which the data shows a closed orbit has been determined. It has been found that the amplitude of the needed correction is equivalent to the observed magnetic field fluctuations. Figure 6.17 shows the data with the underlying Zeeman shift corrected to show a closed cyclotron orbit. The experimental data gives evidence that the atoms follow a closed loop inside the bulk region. Further measurements with prepared momentum states of $p = \pm 2 p_{\mathrm{rec}}$, depicted further down in fig. 6.19, showed less deviations from closed orbits.

Edge

For the measurements at the edges two different routines are used. Measurements at the $m_j = 6$ edge are done the same way as the measurements for the closed cyclotron orbits in the bulk: a specific momentum p_x state is prepared and the frequency is quenched.

Measurements at the $m_j = -6$ edge follow the same routine as to determine the effective coupling strength. The BEC is prepared and the Raman beams are pulsed for different pulse lengths on two photon

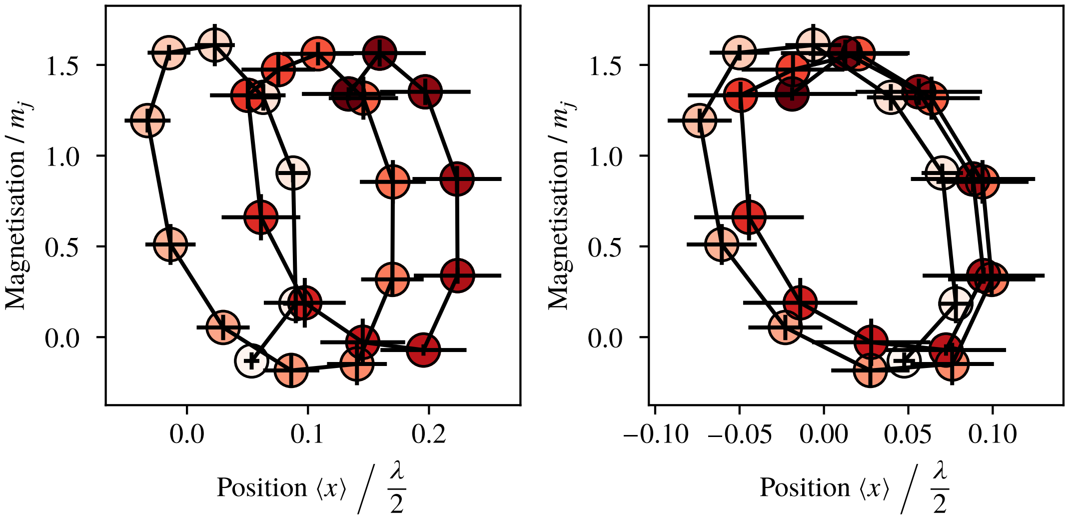

Figure 6.17: Left: a closed orbit is expected for the plotted data. Right: data set which is shown in the left graph but with $\omega_z = \omega_z + \delta\omega_z$. It can be seen that a Zeeman splitting corrected by the external magnetic field fluctuation which result in $\delta\omega_z$ shows a closed loop. These graphs show how important a stable magnetic field is or alternatively that the magnetic field needs to be tracked closely to perform a post correction.

resonance. The Raman light pulse on two photon resonance corresponds to the BEC already in a momentum p_x edge state. An additional momentum p_x state preparation is not necessary. Figure 6.18 shows an edge measurement for the $m_j = 6$ edge at a coupling of $\approx 1.5\ \Omega_{\text{rec}}$. The right graph shows a clear skipping orbit behaviour as expected for a hard edge.

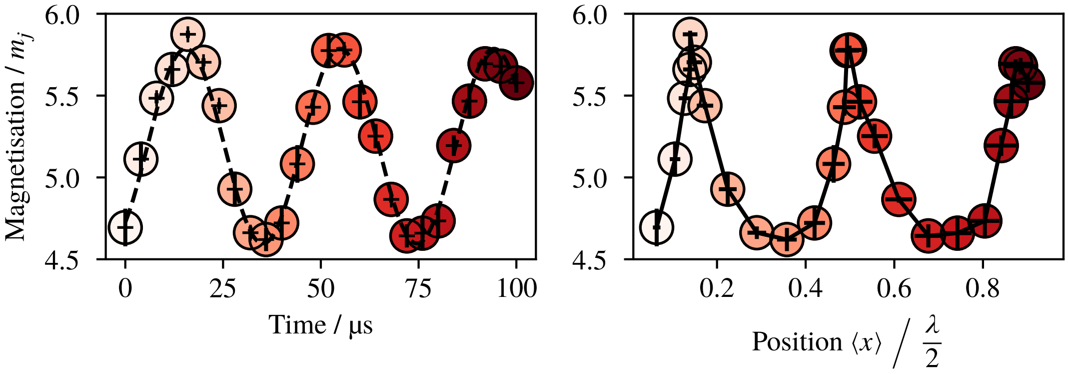

Figure 6.18: Orbit measurement at the edge $m_j = 6$: observing skipping orbits. Left: the magnetisation as function of the time. Right: average magnetisation as function of the real space position obtained by integrating over the velocity of the atoms.

Bulk and edge modes in a two-dimensional quantum Hall ribbon

Cyclotron orbits similar to the cyclotron orbits in an electron Hall system presented in fig. 6.17 can be observed for different prepared momentum states inside the bulk. By combining those measurements including the edge measurements in a two-dimensional quantum ribbon spanning the full synthetic dimension from $m_j = -6$ to $m_j = 6$ the different bulk and edge behaviour is visualised and resembles fig. 4.1 of a electron Hall system. Closed cyclotron orbits are observed in the bulk, in fig. 6.19 for prepared momentum p_x state of $-2, 0$ and $2\,p_{\mathrm{rec}}$. Excitation at opposite edges result in skipping orbits propagation along the edges in different directions.

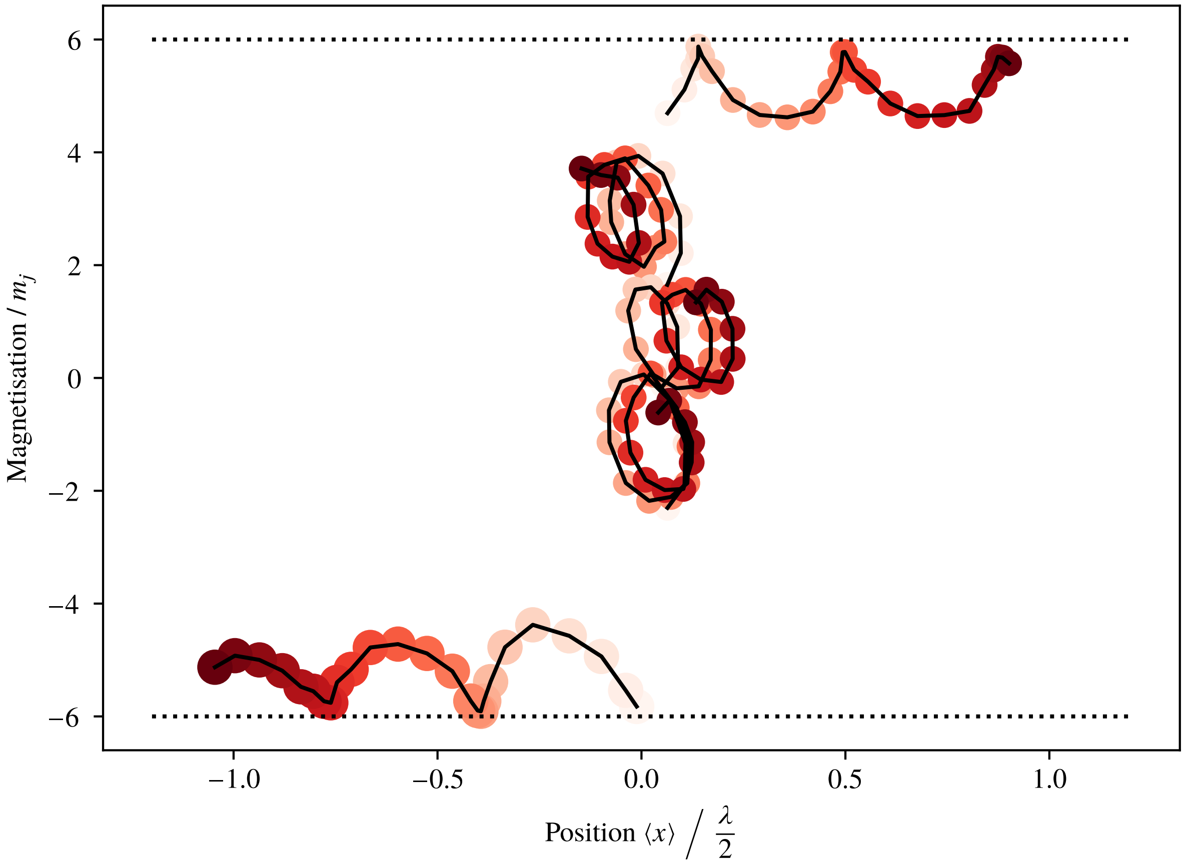

Figure 6.19: Two dimensional quantum Hall ribbon with the real space position $\langle x \rangle$ and an artificial dimension encoded into the magnetisation. The artificial dimension has hard walls at the edges. A clear bulk (closed orbits) and edge (skipping orbits) behaviour can be distinguished. The orbits in the bulk correspond to prepared momentum p_x states of $-2, 0$ and $2\,p_{\mathrm{rec}}$. The lower skipping orbit is obtained by quenching the Raman beam intensity at resonance corresponding to the Zeeman splitting. The upper skipping orbit uses the same experimental procedure as the orbits in the bulk. The system was prepared in a momentum p_x of $\approx 5\,p_{\mathrm{rec}}$ corresponding to an edge state. The orbit measurements were done on different days. The effective coupling varied from $\approx 1.2\,\Omega_{\mathrm{rec}}$ to $\approx 1.5\,\Omega_{\mathrm{rec}}$ and was determined from the oscillation period in the magnetisation.

Limits of the system

The shown trajectories mimic the trajectories of electrons in a two-dimensional plane subject to an external magnetic field. However, if the experimental parameters are not chosen correctly the behaviour changes. Different coupling strengths result in different dispersion relations and therefore in different relative sizes between bulk and edge region. Is the coupling too strong the dispersionless bulk vanishes and the dispersion shows no distinct bulk and edge behaviour. Another important parameter is the frequency quench. Is the quench too strong the atoms can populate more Zeeman levels resulting in a changing orbit radius, as depicted in fig 6.20 for a frequency quench corresponding to $2\,v_{\mathrm{rec}}$ (left), or even drifting orbits combined with a changing orbit radius as depicted in fig. 6.20 for a frequency quench corresponding to $3\,v_{\mathrm{rec}}$ (right).

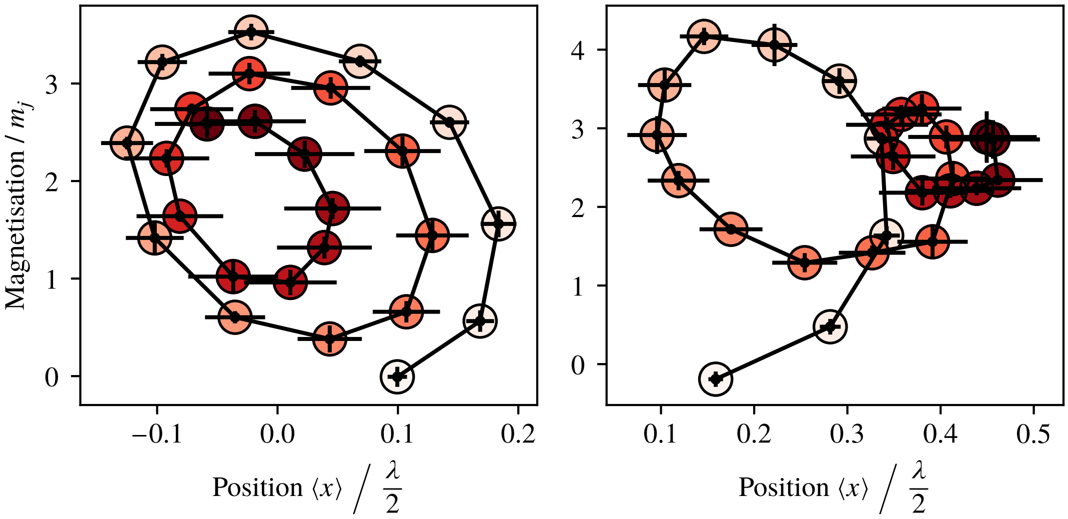

Figure 6.20: Left: experimental data for a frequency quench corresponding to $2\,v_{\mathrm{rec}}$. The circular path starts with a bigger diameter compared to smaller velocity kicks but loses in size for longer times. The effective coupling strength is $\approx 1.2\,\Omega_{\mathrm{rec}}$. Right: experimental data for a frequency quench corresponding to $3\,v_{\mathrm{rec}}$. The quench is so powerful that an additional drift in the real space position x is induced. The effective coupling strength is $\approx 1.0\,\Omega_{\mathrm{rec}}$.

6.8 Synthetic Hall mobility

Using the definition of the mobility for the artificial Hall system derived in section 5.4 the mobility can be calculated from the velocity measurements. The preparation method to prepare a specific momentum p_x state by changing the two photon detuning δ is equivalent to applying a force. From eq. 5.25,

$$\mu_{\mathrm{SOC}} = \frac{1}{2\hbar k}\left(\frac{\partial}{\partial p}(m\langle v\rangle - p)\right), \tag{6.5}$$

it can be seen that the partial derivative of the mean velocity is necessary. For a continuous set of data this would be of little to no problem. The measurements presented here are of discrete nature combined with noise. To decrease the influence of the noise the velocity data has been filtered with a Savitzky-Golay filter [92] before the derivative was calculated. Comparisons between filtered and unfiltered data can be found in the appendix C. An error approximation based on a the propagation of uncertainty resulted in errors larger than the mobility values due to the discrete nature of the data, which is also the reason for the use of a Savitzky-Golay filter in the first place. Therefore an error approximation based on the propagation of uncertainty is not meaningful. To estimate the error a bootstrap sampling analysis could be used, however the underlying data set is not large enough. Since the data shown here is of qualitative nature, the error approximation has been neglected in the calculation of the mobility.

Figure 6.21 shows the mobility (red data points) calculated for the group velocities shown in fig. 6.11 together with the theoretical expected mobility (black line) for an effective coupling strength of 1.44 Ω_{rec}. The expected behaviour can be extracted from the experimental data. The value in the bulk region reaches the expected value of $-(p_{\text{rec}})^{-1}$ corresponding to $-(eB)^{-1}$ in an electron Hall system and decreases towards zero for the edges. The experimental values for negative momenta p_x follow the theoretical expectations closely. Larger momenta p_x show larger deviations from the expectations. This is attributed to the correlation between momentum p_x state and run time of the experiment, as a velocity measurement took about 8 hours with greater momentum p_x states measured later in the day. Despite different measures to stabilise the experimental environment, changes can not be prevented entirely through the day. A changing environment, e.g. the temperature of the laboratory, can lead to all sort of changes with the probably most critical being the external magnetic fields.

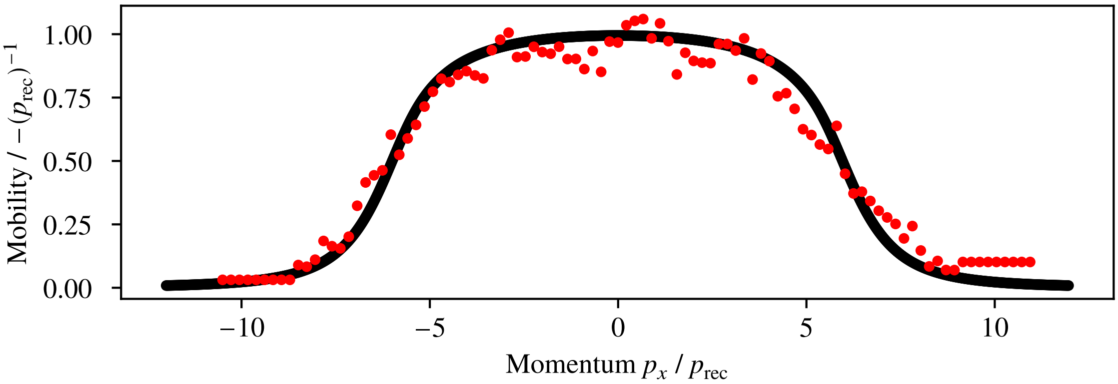

Figure 6.21: Experimentally determined mobility (red points) and theoretical expected mobility (black line) for the data set used in fig. 6.11. The velocity has been filtered by a Savitzky-Golay filter. An error approximation has been neglected , see text.

6.9 Local Chern Marker

As detailed in section 5.5 the LCM can be determined from the mobility. Using eq. 5.25 (mobility) together with eq. 5.29 (LCM) in its discrete form, which is used for the analysis the derivative with respect to the momentum p_x vanishes. Figure 6.22 shows the experimental determined LCM again for the data set used in fig. 6.11. The black marker show the theoretically expected LCM for a coupling of 1.44 Ω_{rec}. As the integration domain again all states with a maximum energy below the ground band energy plus half the energy gap between the ground- and first excited band (for a momentum p_x state of 0) is chosen.

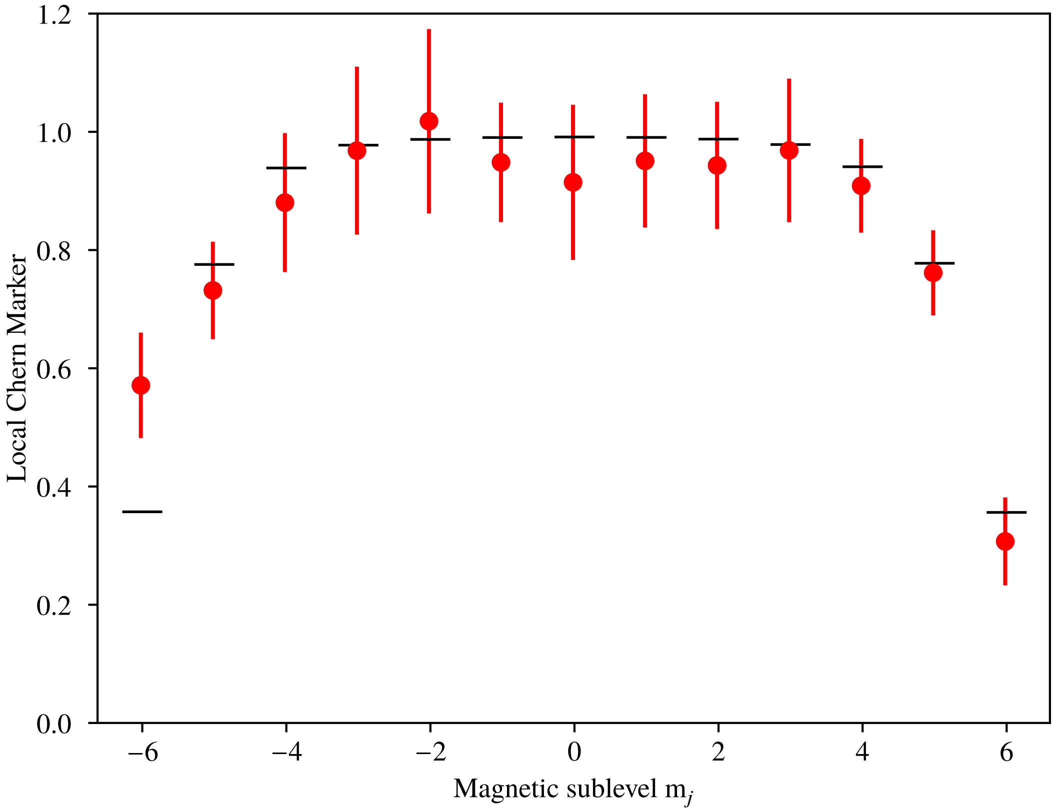

Figure 6.22: Determined value for the Local Chern Marker as function of the magnetic sub level. The experimental data (red marker) is in good agreement with the theoretical expectation (black markers).

Since the experimentally observed behaviour well follows the theoretical expectation, the data is attributed as evidence that the synthetic system indeed has a non trivial topology. In the bulk the LCM has an average value of 0.92 ± 0.12. The bulk region has been determined by determining the magnetisation for which the velocity is smaller than $0.1\,v_{\mathrm{rec}}$. Since these numbers had no integer values the numbers were rounded correspondingly and included all m_j level between -5 to 3. The asymmetry can be explained by the velocity measurement which already shows some asymmetry. For the theoretical bulk region every m_j-level between -4 and 4 was used for the average LCM value and was determined to be 0.98. The LCM being close to one in the bulk shows that the system is (inside the bulk) resembling an electron, infinite Landau system for which the Chern number takes a value of one. By determining the LCM and observing a clear distinguishable behaviour between edge and bulk it has been shown that the system shows quantum Hall like behaviour.

6.10 Chiral edge currents

The above shown orbit measurements have already confirmed chiral edge modes in which the skipping orbits are propagating in different directions depending on the side of the edge. Those skipping orbits were observed in distinct measurements. In order to observe chiral edge currents another experimental routine had to be implemented as to provide excitations simultaneously at both upper and lower system edges. First measurements aiming at showing the general principle and giving first results are presented in the following.

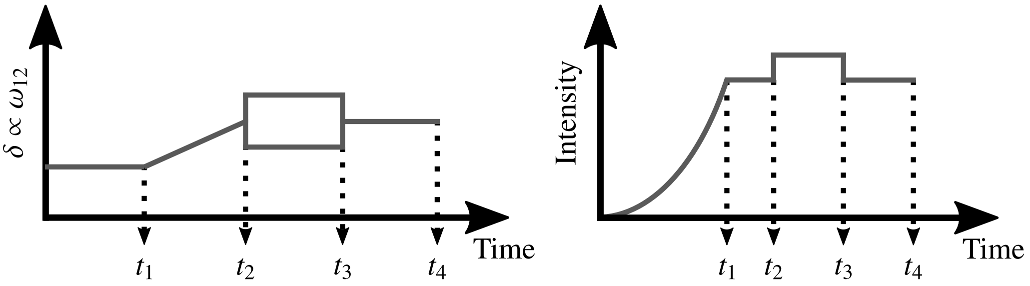

Figure 6.23: Experimental scheme to excite chiral edge currents. From $t = 0$ to t_2 the momentum p_x state $p \approx 0$ is prepared as explained earlier. A frequency and amplitude quench is applied at t_2 and held until t_3. It has been found that a symmetric excitation is realised for holding times of $t_3 - t_2 = 35\,\mu\text{s}$. At t_3 the system is quenched back to the values at t_2 corresponding to the flat dispersion regime and is held until t_4. An absorption image is used to determine the relative number of atoms in $m_j = \pm 6$

After preparing a BEC the sample is prepared in the momentum p_x state $p_x \approx 0$ before it is frequency and intensity quenched. In order to excite orbits in both directions and couple to both edges the sample needs to be quenched with two frequencies, which have the same magnitude but different signs. The quench is chosen to be strong enough to couple to the edges of the system. A holding time after the quench of 35 µs has shown to result in symmetric excitation in both directions. Other holding times resulted in asymmetric excitation. After the holding time of 35 µs the laser frequencies are set back to the values corresponding to a flat dispersion relation and the number of atoms in the $m_j = \pm 6$ is measured as a function of the following holding time $t_h = t_4 - t_3$.

Skipping orbits at both edges are observed simultaneously and the edge currents can be determined. The chiral edge current is approximated as the difference between the two currents defined by the number of atoms in $m_j = \pm 6$. Similar measurements in earlier works have been performed with ^{87}Rb, which provides 3 positions in the synthetic dimension [87] and therefore lack clearly distinguishable bulk and edge modes. For the chiral edge current follows:

$$I_{\text{CEC}} = I_{m_j=-6} - I_{m_j=6} = n_{-6}\langle v_{-6}\rangle - n_6\langle v_6\rangle \tag{6.6}$$

with n_6 and n_{-6} the relative atom populations in the $m_j = 6$ and $m_j = -6$ state and $\langle v_6\rangle$ and $\langle v_{-6}\rangle$ the average velocities of the $m_j = 6$ and $m_j = -6$ states. Figure 6.24 shows a chiral edge current measurement. As expected the current performs an oscillation which is understood by looking at the skipping orbits.

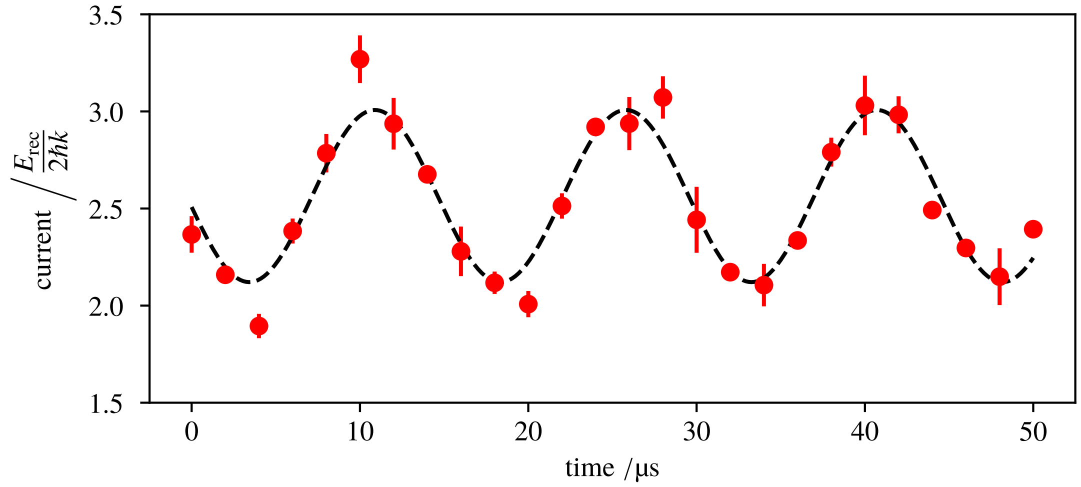

Figure 6.24: Experimentally observed chiral edge current: skipping orbits are excited simultaneously at both edges resulting in currents with approximately the same absolute value but different propagation directions. The difference of both currents defines the chiral edge current and is depicted in the figure (red data points). The black dashed line is a cosine fitted to the experimental data for a better visualisation of the oscillation of the current.

CHAPTER 7

Conclusion and outlook

In this work, a synthetic quantum Hall system with erbium atoms in the lowest Landau level has been experimentally realised. The required two-dimensional system in state space was implemented by one real and one synthetic dimension, the latter being encoded in the internal Zeeman quantum number $m_j = 6, ..., 6$ of erbium ground state atoms. For the first time in a synthetic quantum Hall ribbon with large enough number of Zeeman levels to have distinct bulk and edge behaviour, the chiral edge current has been experimentally determined. For the future it would be extremely interesting to observe the fractional quantum Hall effect in a cold atom system.

Quantum Hall Physics can on the one hand be realised with the synthetic dimension approach investigated in the present work, see [44, 45] for a corresponding proposal. To suppress non-local interactions in internal state space, here a magnetic field gradient is required to spatially separate atoms in different Zeeman levels. Otherwise different positions in the synthetic dimension have the same real space position. Therefore, atoms in different positions in the synthetic dimension (different Zeeman states) can interact with all other position in the synthetic dimension. Applying a real magnetic field gradient as present for the time of flight measurements could separate the different Zeeman states spatially and suppress interaction. Crucially, to realise the fractional quantum Hall regime, much higher filling factors ν are required, which have to be in the order of unity. Specifically, for $\nu = 1/2$ in the bosonic system, it is expected that a fractional quantum Hall liquid emerges for a one-dimensional confinement of cold atoms. Another proposal directly creates a two dimensional system in real space.

To realise a system fully in real space the experimental setup can be extended by a stronger real magnetic field gradient preferably with a strong gradient in one dimension and suppressed gradients along the remaining two dimensions. With such a gradient the scheme used by Lin et al. [42] could be realised. As introduced earlier, this scheme creates a position dependent vector potential by creating a position dependent spin-orbit coupling. The real magnetic field gradient modifies the internal Zeeman states energy levels resulting effectively in a position dependent optical detuning and therefore a changing optical coupling. The needed experimental parameters have been investigated in our group with support from M. Fleischhauer for the here presented experiment and have been published in a paper [93]. The in the paper presented scheme does not rely on a synthetic dimension and therefore observations are done in a two-dimensional real space system. A first step would include a relatively weak artificial magnetic field like in the data presented in [42]. For weak fields, vortices with a core size of the healing length of the Bose-Einstein condensate should be observable. Vortices are objects for which the wave function of the Bose-Einstein condensate vanishes and are therefore regions with an atom density of zero. Stronger artificial magnetic fields would create more vortices. Is the number of vortices comparable to the number of atoms in the Bose-Einstein condensate a filling factor of $\nu = 1/2$ can be realised. This is the region in which fractional quantum Hall behaviour should become dominant.

In a first step vortices would be realised and investigated by means of the dipolar nature of erbium. The density profile of a single vortex should be dependent on the dipole-dipole interactions and thus should be able to be modified by changing the dipole-dipole interaction strength [94]. Theoretical investigations have also shown that dipolar interactions as in the case of erbium should result in modifications in the Abrikosov vortex lattice [94]. Despite many laboratories working with dipolar quantum gases these effects have not been experimentally observed.

Experimental observations regarding fractional quantum Hall physics can be realised by observing a collapse and revival response in the interference pattern of several interfering micro clouds in the far field. The ground state in the strong synthetic magnetic field is then no longer a the Bose-Einstein condensate but a highly correlated state. Therefore a collapse and revival of the far field interference pattern is expected upon reaching and leaving the strongly correlated fractional quantum Hall regime. Further work aims at detecting a quantised dissipative response for circular periodic driving as pointed out in [95]. A periodic driven array of micro clouds should show a quantised dissipative response by means of a variation in the loss rate caused by the periodic driving of the system. The frequency integrated response of the atomic loss rate is expected to show a quantised response between a left and a right handed periodic driving, which can give further evidence for a fractual quantum Hall conductance [96].

Another proposal aims at the observation of parafermionic zero modes. A fractional quantum Hall liquid in a trench embedded into a Bose-Einstein condensate can show parafermionic zero modes at the two ends of the trench [97]. In contrast to other proposal relying on fermionic systems for the fractional quantum Hall liquid here only a single atomic species is required, which can simplify an experimental realisation.

APPENDIX A

Spin orbit coupled Hamiltonian for erbium

The start is a Hamiltonian [89] which describes the atom light interaction:

$$\hat{H} = \hat{H}_0 + \hat{H}_{\text{int}} \tag{A.1}$$

with $\hat{H}_0 = \hat{\boldsymbol{p}}^2/(2m) + \hbar\omega_z \hat{J}_z$ and

$$\hat{H}_{\text{int}} = V_0 \left\{ \alpha_s |\boldsymbol{u}|^2 \, \mathbb{1} - i\alpha_v (\boldsymbol{u}^* \times \boldsymbol{u}) \frac{\hat{\boldsymbol{J}}}{2J} + \alpha_t \frac{3[(\boldsymbol{u}^*\hat{\boldsymbol{J}})(\boldsymbol{u}\hat{\boldsymbol{J}}) + (\boldsymbol{u}\hat{\boldsymbol{J}})(\boldsymbol{u}^*\hat{\boldsymbol{J}})] - 2|\boldsymbol{u}|^2\hat{\boldsymbol{J}}^2}{2J(2J-1)} \right\}. \tag{A.2}$$

$\hat{H}_0$ describes the particle's energy in a magnetic field along the z-direction with $\boldsymbol{p}$ the particle's momentum, m the particle's mass, $\hat{J}_z$ the dimensionless spin projection operator and ω_z the frequency of the corresponding Zeeman splitting. $\hat{H}_{\text{int}}$ describes interaction between the atoms and the external light field. Here α_i are the scalar, vectorial and tensorial polarisation coefficients and $\hat{\boldsymbol{J}}$ is the total angular momentum operator with $J = 6$ in the case of erbium. The vectors $\boldsymbol{u}$ are the position dependent polarisation vectors defined by

$$\boldsymbol{u} = \frac{1}{2} e^{-i\omega_0 t} \left[e^{ikx} (\hat{\boldsymbol{y}} + \hat{\boldsymbol{z}}) + e^{-i(kx + (\omega_z + \delta)t)} (\hat{\boldsymbol{y}} - \hat{\boldsymbol{z}}) \right] \tag{A.3}$$

and the coupling strength V_0 is given by

$$V_0 = \frac{3\pi c^2 \Gamma I}{2\omega_0^3 \Delta_s}. \tag{A.4}$$

Here c is the speed of light, Γ the natural linewidth of the used transition, I the light's intensity and Δ the single photon detuning. Combining eq. A.2 and eq. A.3 eq. A.2 reduces to

$$\hat{H}_{\text{int}} = V_0 \left[\alpha_s \hat{\mathbb{1}} + \alpha_v \sin(\phi) \frac{\hat{J}_x}{2J} + \alpha_t \frac{\hat{\boldsymbol{J}}^2 - 3\hat{J}_x^2 + 3\cos(\phi) \left(\hat{J}_y^2 - \hat{J}_z^2 \right)}{2J(2J-1)} \right] \tag{A.5}$$

with $\phi = 2kx + (\omega_z + \delta)t$. A unitary transformation is applied by replacing $|\psi\rangle$ with

$$|\Psi\rangle = \hat{U} |\psi\rangle = e^{i(\omega_z + \delta)t\hat{J}_z} |\psi\rangle \tag{A.6}$$

to transfer into a system rotating at $\omega_{\mathrm{RWA}} = \omega_z + \delta$. The transfer is done via

$$i\hbar \frac{\mathrm{d}\,|\Psi\rangle}{\mathrm{d}t} = \hat{H}_{\mathrm{RWA}}\,|\Psi\rangle \tag{A.7}$$

and

$$\hat{H}_{\mathrm{RWA}} = i\hbar \frac{\mathrm{d}\hat{U}}{\mathrm{d}t}\hat{U}^{+} + \hat{U}\hat{H}\hat{U}^{+}. \tag{A.8}$$

It follows

$$\begin{aligned} \hat{H}_{\mathrm{RWA},0} &= i\hbar \frac{\mathrm{d}\hat{U}}{\mathrm{d}t}\hat{U}^{+} + \hat{U}\hat{H}_0\hat{U}^{+} \\ &= -\hbar(\omega_z+\delta)\hat{J}_z + e^{i(\omega_z+\delta)t\hat{J}_z}\frac{\hat{p}^2}{2m}e^{-i(\omega_z+\delta)t\hat{J}_z} + e^{i(\omega_z+\delta)t\hat{J}_z}\hbar\omega_z\hat{J}_z e^{-i(\omega_z+\delta)t\hat{J}_z}. \end{aligned}$$

Using the Baker-Hausdorff lemma [1] $\hat{H}_{\mathrm{RWA},0}$ can be expressed as

$$\hat{H}_{\mathrm{RWA},0} = \frac{\hat{\boldsymbol{p}}^2}{2m} - \hbar\delta\hat{J}_z.$$

The unitary transformation acting on $\hat{H}_{\mathrm{int}}$ is not as straightforward. First the ladder operators $\hat{J}_+ = \hat{J}_x + i\hat{J}_y$ and $\hat{J}_- = \hat{J}_x - i\hat{J}_y$ are introduced and $\hat{J}_x$ and $\hat{J}_y$ are replaced

$$\begin{aligned} \hat{H}_{\mathrm{int}} =& V_0\Bigg[\alpha_s\hat{\mathbb{1}} + \alpha_v\sin(\phi)\frac{\hat{J}_+ + \hat{J}_-}{4J} \\ &+ \frac{\alpha_t}{2J(2J-1)}\left(\hat{\boldsymbol{J}}^2 - \frac{3}{4}(\hat{J}_+ + \hat{J}_-)^2 - \frac{3}{4}\cos(\phi)(\hat{J}_+ - \hat{J}_-)^2 - 3\cos(\phi)\hat{J}_z^2\right)\Bigg]. \end{aligned}$$

Together with the Baker-Haussdorff lemma and the exponential function in its series form [2] it can be shown that

$$\hat{U}\hat{J}_\pm\hat{U}^{+} = \hat{U}(\hat{J}_x \pm i\hat{J}_y)\hat{U}^{+} = e^{\pm i(\omega_z+\delta)t}\hat{J}_\pm \tag{A.9}$$

which leads to

$$\hat{H}_{\mathrm{RWA,int}} = V_0\Bigg[\alpha_s\hat{\mathbb{1}} + \alpha_v\sin(\phi)\left(\frac{e^{i(\omega_z+\delta)t}\hat{J}_+ + e^{-i(\omega_z+\delta)t}\hat{J}_-}{4J}\right) \tag{A.10}$$

$$+ \frac{\alpha_t}{2J(2J-1)}\Bigg(\hat{\boldsymbol{J}}^2 - \frac{3}{4}\left(e^{2i(\omega_z+\delta)t}\hat{J}_+^2 + e^{-2i(\omega_z+\delta)t}\hat{J}_-^2 + \hat{J}_+\hat{J}_- + \hat{J}_-\hat{J}_+\right) \tag{A.11}$$

$$- \frac{3}{4}\cos(\phi)\left(e^{2i(\omega_z+\delta)t}\hat{J}_+^2 + e^{-2i(\omega_z+\delta)t}\hat{J}_-^2 - \hat{J}_+\hat{J}_- - \hat{J}_-\hat{J}_+ - 4\hat{J}_z^2\right)\Bigg)\Bigg]. \tag{A.12}$$

The rotating wave approximation (RWA) can be applied by only keeping slowly varying terms. A bit of caution has to be taken for the $\sin(\phi)$ term since ϕ contains a time component. Replacing the sine by its exponential form followed by some algebra leads to

$$\hat{H}_{\mathrm{RWA,int}} = V_0\left[\alpha_s\hat{\mathbb{1}} + \frac{\alpha_v}{i8J}\left(e^{i2kx}\hat{J}_- - e^{-i2kx}\hat{J}_+\right) + \frac{\alpha_t}{2J(2J-1)}\left(\hat{\boldsymbol{J}}^2 - \frac{3}{2}\left(\hat{J}_x^2 + \hat{J}_y^2\right)\right)\right]. \tag{A.13}$$

---

[1] $e^{x\hat{A}}\hat{B}e^{-a\hat{A}} = \hat{B} + \frac{x}{1!}[\hat{A},\hat{B}] + \frac{x^2}{2!}\left[\hat{A},[\hat{A},\hat{B}]\right] + \frac{x^3}{3!}\left[\hat{A},\left[\hat{A},[\hat{A},\hat{B}]\right]\right] + \ldots$

[2] $e^x = \sum_{k=0}^{\infty}\frac{x^k}{k!}$

At this point the SOC can already be seen: A change in the spin projection is associated with a momentum kick of $2k$. To make the momentum change more visible a unitary transformation in position space can be applied:

$$|\Psi\rangle = e^{i2k\hat{x}\hat{J}_z}\,|\psi\rangle\,. \tag{A.14}$$

With $[\hat{x}, J_z] = 0$ and $[\hat{p}_x, J_z] = 0$ it follows for $H_{\mathrm{RWA},0}$

$$\begin{aligned} e^{i2k\hat{x}\hat{J}_z}\frac{\hat{p}^2}{2m}e^{-i2k\hat{x}\hat{J}_z} &= \tfrac{1}{2m}\Big(\hat{p}^2 + i2k[\hat{x}\hat{J}_z,\hat{p}^2] + \tfrac{(i2k)^2}{2!}\left[\hat{x}\hat{J}_z,[\hat{x}\hat{J}_z,\hat{p}^2]\right] && \text{(A.15)}\\ &\quad + \tfrac{(i2k)^3}{3!}\Big[\hat{x}\hat{J}_z,\left[\hat{x}\hat{J}_z,[\hat{x}\hat{J}_z,\hat{p}^2]\right]\Big] + \ldots\Big) && \text{(A.16)}\end{aligned}$$

with

$$\begin{aligned} [\hat{x}\hat{J}_z,\hat{p}^2] &= \hat{x}[\hat{J}_z,\hat{p}^2] + [\hat{x},\hat{p}^2]\hat{J}_z = i2\hbar\hat{p}_x\hat{J}_z && \text{(A.17)}\\ [\hat{J}_z,\hat{p}^2] &= 0 && \text{(A.18)}\\ [\hat{x},\hat{p}^2] &= i2\hbar\hat{p}_x && \text{(A.19)}\end{aligned}$$

and

$$\begin{aligned} \left[\hat{x}\hat{J}_z,[\hat{x}\hat{J}_z,\hat{p}^2]\right] &= i2\hbar[\hat{x}\hat{J}_z,\hat{p}_x\hat{J}_z] && \text{(A.20)}\\ &= i2\hbar\left(\hat{x}[\hat{J}_z,\hat{p}_x]\hat{J}_z + \hat{x}\hat{p}_x[\hat{J}_z,J_z] + [\hat{x},\hat{p}_x]\hat{J}_z\hat{J}_z + \hat{p}_x[\hat{x},\hat{J}_z]\hat{J}_z\right) && \text{(A.21)}\\ &= i2\hbar i\hbar\hat{J}_z^2 = -2\hbar^2\hat{J}_z^2. && \text{(A.22)}\end{aligned}$$

Moreover,

$$\Big[\hat{x}\hat{J}_z,\left[\hat{x}\hat{J}_z,[\hat{x}\hat{J}_z,\hat{p}^2]\right]\Big] = -2\hbar^2[\hat{x}\hat{J}_z,\hat{J}_z^2] = 0, \tag{A.23}$$

therefore it follows

$$\begin{aligned} e^{i2k\hat{x}\hat{J}_z}\frac{\hat{p}^2}{2m}e^{-i2k\hat{x}\hat{J}_z} &= \frac{1}{2m}\left(\hat{p}^2 - 4\hbar k\hat{p}_x\hat{J}_z + 4\hbar^2k^2\hat{J}_z^2\right) && \text{(A.24)}\\ &= \frac{(\hat{p}_y^2 + \hat{p}_z^2 + (\hat{p}_x - 2\hbar k\hat{J}_z))^2}{2m}. && \text{(A.25)}\end{aligned}$$

For the second term of $\hat{H}_{\mathrm{RWA},0}$ it follows

$$e^{i2k\hat{x}\hat{J}_z}\hbar\delta\hat{J}_z e^{-i2k\hat{x}\hat{J}_z} = \hbar\delta\hat{J}_z + 0. \tag{A.26}$$

The first scalar term of $\hat{H}_{\mathrm{RWA,int}}$ is trivial and is unchanged by the unitary transformation. For the vectorial term two terms need to be solved:

$$\begin{aligned} &e^{i2k\hat{x}\hat{J}_z}e^{i2k\hat{x}}\hat{J}_- e^{-i2k\hat{x}\hat{J}_z} && \text{(A.27)}\\ &e^{i2k\hat{x}\hat{J}_z}e^{-i2k\hat{x}}\hat{J}_+ e^{-i2k\hat{x}\hat{J}_z}. && \text{(A.28)}\end{aligned}$$

Going through the algebra and using $[\hat{J}_z, \hat{J}_\pm] = \pm\hat{J}_\pm$:

$$e^{i2k\hat{x}\hat{J}_z} e^{i2k\hat{x}} \hat{J}_- e^{-i2k\hat{x}\hat{J}_z} = e^{i2k\hat{x}} \Big(\frac{(i2k\hat{x})^0}{0!} \hat{J}_- \tag{A.29}$$

$$+ \frac{(i2k\hat{x})^1}{1!} [\hat{J}_z, \hat{J}_-] \tag{A.30}$$

$$+ \frac{(i2k\hat{x})^2}{2!} \big[\hat{J}_z, [\hat{J}_z, \hat{J}_-]\big] \tag{A.31}$$

$$+ \frac{(i2k\hat{x})^3}{3!} \Big[\hat{J}_z, \big[\hat{J}_z, [\hat{J}_z, \hat{J}_-]\big]\Big] \tag{A.32}$$

$$+ \ldots \Big) \tag{A.33}$$

$$= e^{i2k\hat{x}} \Big(\sum_{n=0}^{n=\infty} \frac{(-i2k\hat{x})^n}{n!} \hat{J}_- \Big) \tag{A.34}$$

$$= e^{i2k\hat{x}} e^{-i2k\hat{x}} \hat{J}_- \tag{A.35}$$

$$= \hat{J}_- . \tag{A.36}$$

The second term follows analogously:

$$e^{i2k\hat{x}\hat{J}_z} e^{-i2k\hat{x}} \hat{J}_+ e^{-i2k\hat{x}\hat{J}_z} = \hat{J}_+ \tag{A.37}$$

and finally for the vectorial term in $\hat{H}_{\mathrm{RWA,int}}$

$$\frac{\alpha_v}{i8J} e^{i2k\hat{x}\hat{J}_z} \Big(e^{i2k\hat{x}} \hat{J}_- - e^{-i2k\hat{x}} \hat{J}_+ \Big) e^{-i2k\hat{x}\hat{J}_z} = \frac{\alpha_v}{i8J} \Big(\hat{J}_+ - \hat{J}_- \Big) = -\frac{\alpha_v}{4J} \hat{J}_y . \tag{A.38}$$

The tensorial term can be rewritten to

$$\frac{\alpha_t}{2J(2J-1)} \Big(\hat{\boldsymbol{J}}^2 - \frac{3}{2} \big(\hat{J}_x^2 + \hat{J}_y^2 \big) \Big) = \frac{\alpha_t}{2J(2J-1)} \Big(-\frac{1}{2} \hat{\boldsymbol{J}}^2 + \frac{3}{2} \hat{J}_z^2 \Big) = \frac{\alpha_t}{2J(2J-1)} \Big(\frac{3}{2} \hat{J}_z^2 \Big) \tag{A.39}$$

with the part proportional to $\hat{\boldsymbol{J}}^2$ negligible, since it accounts only for an energy offset. The total Hamiltonian follows to be

$$\hat{H}_{\mathrm{SOC}} = \frac{\hat{p}_y^2 + \hat{p}_z^2}{2m} + \frac{(\hat{p}_x - 2\hbar k \hat{J}_z)^2}{2m} - \hbar\delta\hat{J}_z + V_0 \Big[\alpha_s \mathbb{1} - \frac{\alpha_v}{4J} \hat{J}_y + \frac{\alpha_t}{2J(2J-1)} \frac{3}{2} \hat{J}_z^2 \Big] \tag{A.40}$$

where the trivial dynamics by $\hat{p}_y$ and $\hat{p}_z$ will be dropped in the following.

Equation A.40 can be further simplified by explicitly writing out the polarisabilities. Moreover, $\alpha_s \mathbb{1}$ which accounts for a constants energy offset can be dropped. From [89] α_v and α_t can be determined to be

$$\alpha_v = -\sqrt{\frac{2J}{(J+1)(2J+1)}} \alpha_{(1)} \tag{A.41}$$

$$\alpha_t = -\sqrt{\frac{2J(2J-1)}{3(J+1)(2J+1)(2J+3)}} \alpha_{(2)} \tag{A.42}$$

with

$$\begin{aligned} \alpha_K &= (-1)^{K+J+1}\sqrt{2K+1}\begin{Bmatrix} 1 & K & 1 \\ J & J+1 & J \end{Bmatrix} |\langle n, J+1|\hat{\boldsymbol{d}}|nJ\rangle|^2 && \text{(A.43)} \\ &\times \frac{1}{\hbar}\mathrm{Re}\left(\frac{1}{-\Delta - i\Gamma/2} - \frac{(-1)^K}{\Delta + 2\omega + i\Gamma/2}\right). && \text{(A.44)} \end{aligned}$$

Here Δ is used for the optical detuning, Γ the transition's natural linewidth, ω the light field's angular frequency and the curly brackets $\{\}$ denote the Wigner-6J symbol. Here it was assumed that only the addressed transition dominates the polarisability. Equation part A.44 can be written as $-(\hbar\Delta)^{-1}$ by making the assumption that $|\Delta| \gg \Gamma$. Furthermore using

$$|\langle n, J+1|\hat{\boldsymbol{d}}|nJ\rangle|^2 = \Gamma\frac{3\pi\epsilon_0\hbar c^3}{\omega_0^3}(2J+3) \tag{A.45}$$

it follows

$$\alpha_K = (-1)^{K+J+2}\sqrt{2K+1}\begin{Bmatrix} 1 & K & 1 \\ J & J+1 & J \end{Bmatrix}\Gamma\frac{3\pi\epsilon_0 c^3}{\omega_0^3}(2J+3)\frac{1}{\Delta} \tag{A.46}$$

with ϵ_0 the vacuum permittivity and c the speed of light in vacuum. Hence

$$\begin{aligned} \alpha_v &= \frac{90}{91} && \text{(A.47)} \\ \alpha_t &= -\frac{22}{91} = -\frac{15}{2J+3}\frac{22}{91} && \text{(A.48)} \end{aligned}$$

with $J = 6$ which leads to

$$\begin{aligned} \hat{H}_{\mathrm{SOC}} &= \frac{(\hat{p}_x - 2\hbar k\hat{J}_z)^2}{2m} - \hbar\delta\hat{J}_z + V_0\left[-\frac{15}{364}\hat{J}_y - \frac{1}{2J+3}\frac{15}{364}\hat{J}_z^2\right] && \text{(A.49)} \\ &= \frac{(\hat{p}_x - 2\hbar k\hat{J}_z)^2}{2m} - \hbar\delta\hat{J}_z - \hbar\Omega\left[\hat{J}_y + \frac{1}{2J+3}\hat{J}_z^2\right] && \text{(A.50)} \end{aligned}$$

with $\hbar\Omega = V_0 15/364$.

APPENDIX B

Uncoupled atomic dispersion relation

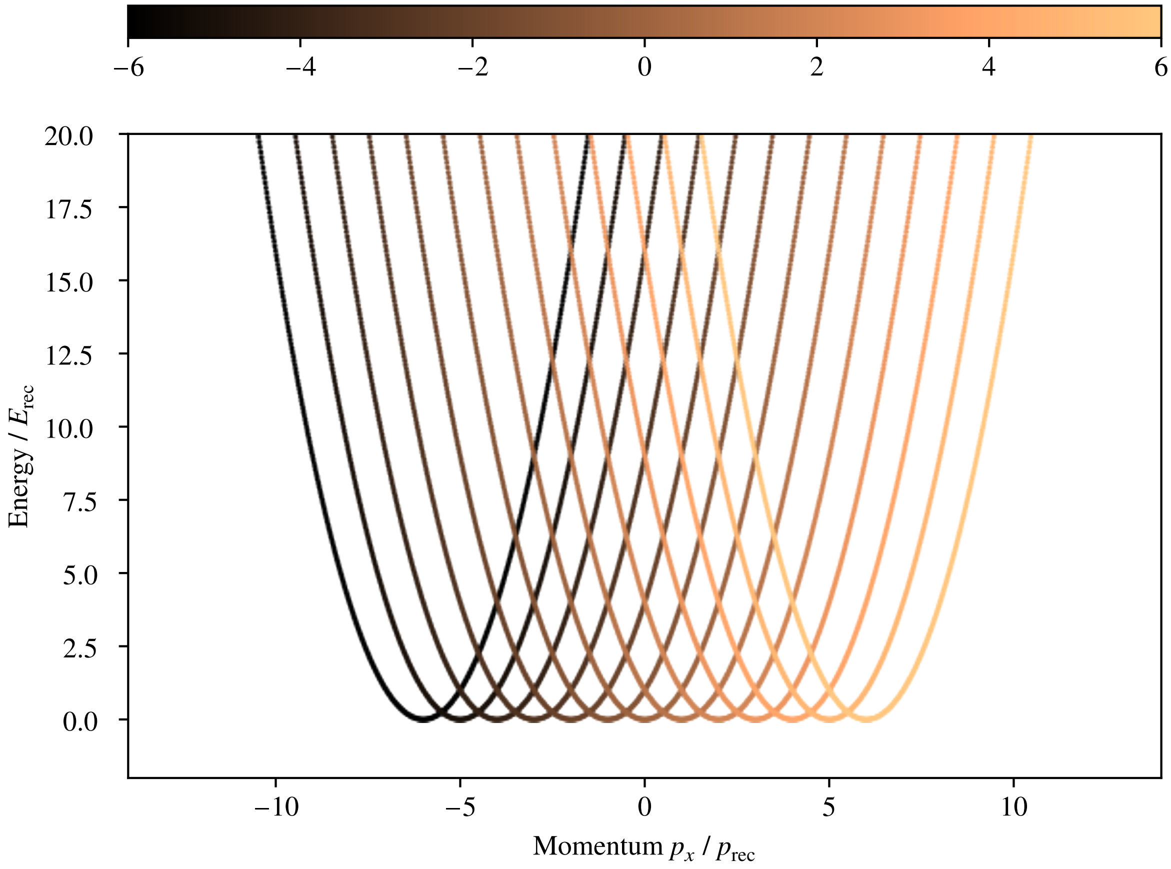

Figure B.1: Dispersion parabolas without effective coupling.

Figure B.1 shows the dispersion relation of the 13 parabolas for the uncoupled case, see chapter 5.3.

APPENDIX C

Velocity filter

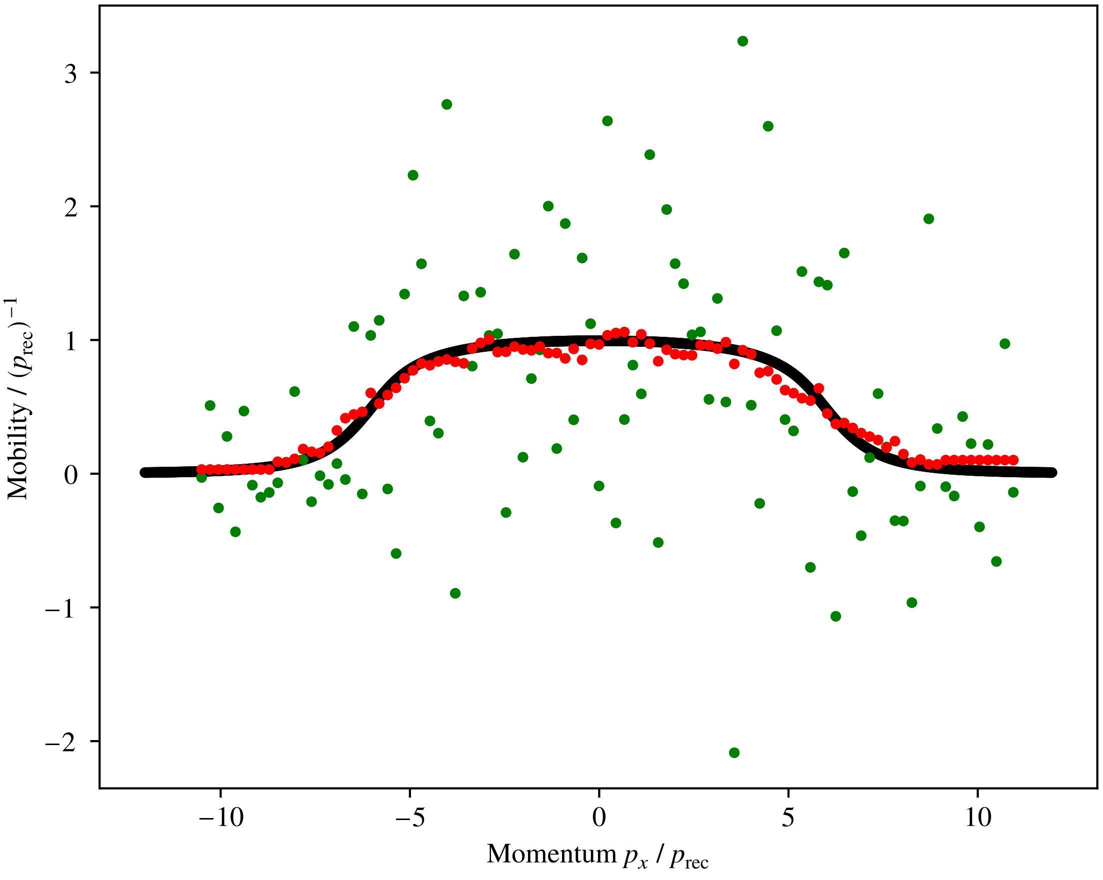

Figure C.1: Comparison between the theoretical expected mobility (black), the mobility using the unfiltered velocity (green) and using the filtered velocity (red).

To extract the mobility (see section 6.8) from the measured dispersion relation a Savitzky-Golay filter was used to flatten the velocity data. Figure C.1 shows the determined mobility using the experimentally determined velocities. It is the same dataset as used in sec. 6.8. The green points show the mobility without applied filter. Only the amplitude of the noise is following the in black shown theoretical expectation. Applying the Savitzky-Golay filter with polynomial order 1 and a filter window of 19 points the red mobility is obtained.

Figure C.2 (top) shows the difference between unfiltered and filtered velocity. In green again the unfiltered data and in red the filtered data. The two graphs in fig. C.2 (bottom) compare the unfiltered and filtered data with the theoretically expected velocity. The difference between theory and experimental data is more prominent in the filtered data. Momenta p_x smaller than 0 better follow the expectation. As already mentioned in section 6.8 such a measurement took around 8 hours and data which was taken later deviates more from the theoretical expectation. Therefore, it is likely caused by drifts in the laboratory. In the unfiltered data this difference is not as clear.

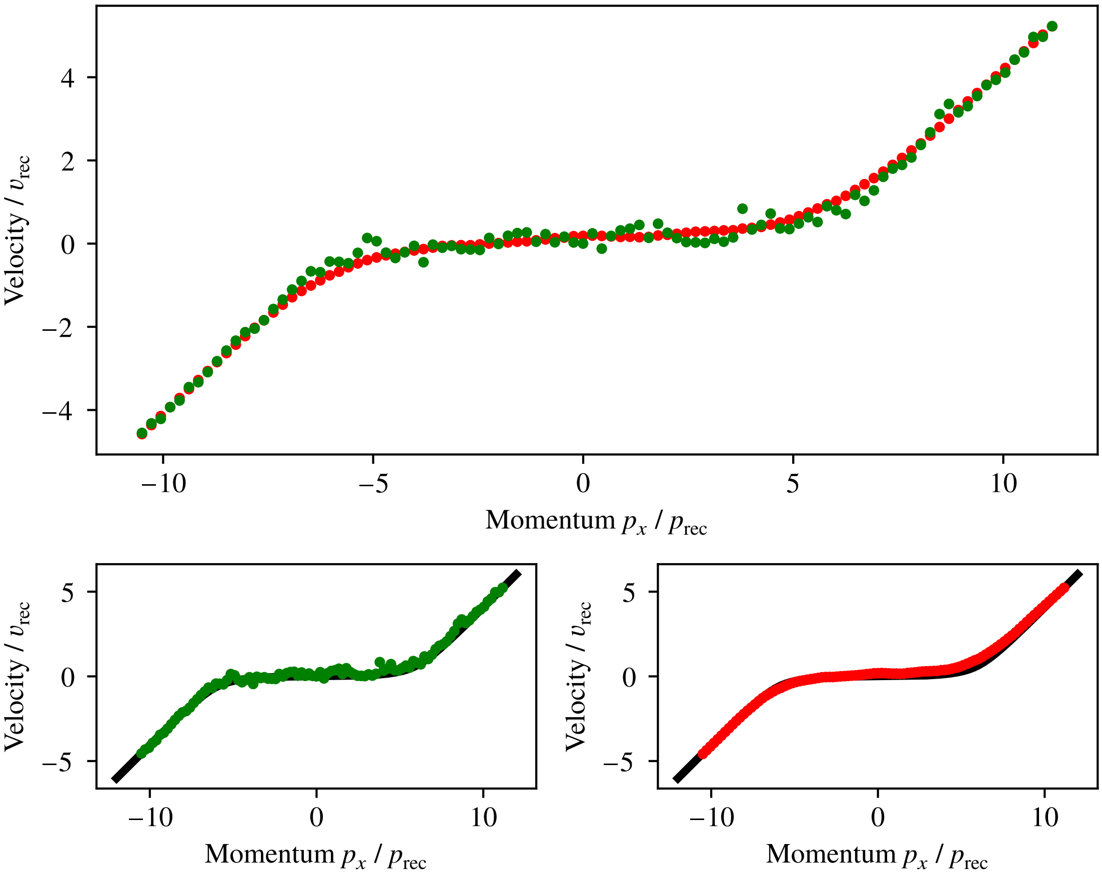

Figure C.2: Top: comparison of unfiltered (green) and filtered (red) velocity using a Savitzky-Golay filter. Bottom: unfiltered (left) and filtered (right) velocities compared to the theoretical velocities. The filtered data shows a clear deviation from the theory for later in the day measured data points.

Bibliography

[1] T. Ando, Y. Matsumoto and Y. Uemura, *Theory of Hall effect in a two-dimensional electron system*, Journal of the Physical Society of Japan **39**, 2 279–288 (1975).

[2] J.-i. Wakabayashi and S. Kawaji, *Hall effect in silicon MOS inversion layers under strong magnetic fields*, Journal of the Physical Society of Japan **44**, 6 1839–1849 (1978).

[3] K. v. Klitzing, G. Dorda and M. Pepper, *New method for high-accuracy determination of the fine-structure constant based on quantized Hall resistance*, Physical review letters **45**, 6 494 (1980).

[4] K. von Klitzing, *Quantum hall effect: discovery and application*, Annual Review of Condensed Matter Physics **8** 13–30 (2017).

[5] https://www.nist.gov/si-redefinition, Accessed June 29, 2022.

[6] D. C. Tsui, H. L. Stormer and A. C. Gossard, *Two-dimensional magnetotransport in the extreme quantum limit*, Physical Review Letters **48**, 22 1559 (1982).

[7] https://www.nobelprize.org/prizes/physics/1998/summary/, Accessed June 29, 2022.

[8] P. J. Ford and G. A. Saunders, *The rise of the superconductors*, CRC press, 2004.

[9] T. H. Maiman et al., *Stimulated optical emission in fluorescent solids. II. Spectroscopy and stimulated emission in ruby*, Physical Review **123**, 4 1151 (1961).

[10] A. Javan, W. R. Bennett Jr and D. R. Herriott, *Population inversion and continuous optical maser oscillation in a gas discharge containing a He-Ne mixture*, Physical Review Letters **6**, 3 106 (1961).

[11] https://www.nobelprize.org/prizes/physics/1997/summary/, Accessed June 29, 2022.

[12] W. D. Phillips, *Nobel Lecture: Laser cooling and trapping of neutral atoms*, Reviews of Modern Physics **70**, 3 721 (1998).

[13] E. L. Raab et al., *Trapping of neutral sodium atoms with radiation pressure*, Physical review letters **59**, 23 2631 (1987).

[14] C. Monroe et al., *Very cold trapped atoms in a vapor cell*, Physical Review Letters **65**, 13 1571 (1990).

[15] J. Bjorkholm et al., *Observation of focusing of neutral atoms by the dipole forces of resonance-radiation pressure*, Physical review letters **41**, 20 1361 (1978).

[16] A. Ashkin, *Acceleration and trapping of particles by radiation pressure*, Physical review letters **24**, 4 156 (1970).

[17] A. Ashkin et al., *Observation of a single-beam gradient force optical trap for dielectric particles*, Optics letters **11**, 5 288–290 (1986).

[18] S. Chu et al., *Experimental observation of optically trapped atoms*, Physical review letters **57**, 3 314 (1986).

[19] M. H. Anderson et al., *Observation of Bose-Einstein condensation in a dilute atomic vapor*, science **269**, 5221 198–201 (1995).

[20] K. B. Davis et al., *Bose-Einstein condensation in a gas of sodium atoms*, Physical review letters **75**, 22 3969 (1995).

[21] B. G. Levi, *Cornell, Ketterle, and Wieman Share Nobel Prize for Bose-Einstein Condensates.*, Physics Today **54**, 12 14–16 (2001).

[22] E. A. Cornell and C. E. Wieman, *Nobel Lecture: Bose-Einstein condensation in a dilute gas, the first 70 years and some recent experiments*, Reviews of Modern Physics **74**, 3 875 (2002).

[23] S. Bose, *Plancks Gesetz und Lichtquantenhypothese Zeitschrift for Physik*, 1924.

[24] A. Einstein, *Quantentheorie des einatomigen idealen gases, sitzungsberichte kgl*, Preuss. Akad. Wiss **261** (1924).

[25] J. Klaers et al., *Bose–Einstein condensation of photons in an optical microcavity*, Nature **468**, 7323 545–548 (2010).

[26] J. Klaers, F. Vewinger and M. Weitz, *Thermalization of a two-dimensional photonic gas in a 'white wall'photon box*, Nature Physics **6**, 7 512–515 (2010).

[27] Y. Aharonov and D. Bohm, *Significance of electromagnetic potentials in the quantum theory*, Physical Review **115**, 3 485 (1959).

[28] K. W. Madison et al., *Vortex formation in a stirred Bose-Einstein condensate*, Physical review letters **84**, 5 806 (2000).

[29] N. R. Cooper, N. K. Wilkin and J. Gunn, *Quantum phases of vortices in rotating Bose-Einstein condensates*, Physical review letters **87**, 12 120405 (2001).

[30] V. Bretin et al., *Fast rotation of a Bose-Einstein condensate*, Physical review letters **92**, 5 050403 (2004).

[31] V. Schweikhard et al., *Rapidly rotating Bose-Einstein condensates in and near the lowest Landau level*, Physical review letters **92**, 4 040404 (2004).

[32] A. Aftalion, X. Blanc and J. Dalibard, *Vortex patterns in a fast rotating Bose-Einstein condensate*, Physical Review A **71**, 2 023611 (2005).

[33] D. Jaksch and P. Zoller, *Creation of effective magnetic fields in optical lattices: the Hofstadter butterfly for cold neutral atoms*, New Journal of Physics **5**, 1 56 (2003).

[34] F. Gerbier and J. Dalibard, *Gauge fields for ultracold atoms in optical superlattices*, New Journal of Physics **12**, 3 033007 (2010).

[35] N. R. Cooper, *Optical flux lattices for ultracold atomic gases*, Physical review letters **106**, 17 175301 (2011).

[36] M. Aidelsburger et al., *Experimental realization of strong effective magnetic fields in an optical lattice*, Physical review letters **107**, 25 255301 (2011).

[37] K. Osterloh et al., *Cold atoms in non-abelian gauge potentials: From the hofstadter" moth" to lattice gauge theory*, Physical review letters **95**, 1 010403 (2005).

[38] D. Jaksch and P. Zoller, *The cold atom Hubbard toolbox*, Annals of physics **315**, 1 52–79 (2005).

[39] M. Aidelsburger et al., *Realization of the Hofstadter Hamiltonian with ultracold atoms in optical lattices*, Physical review letters **111**, 18 185301 (2013).

[40] M. Aidelsburger et al., *Measuring the Chern number of Hofstadter bands with ultracold bosonic atoms*, Nature Physics **11**, 2 162–166 (2015).

[41] J. Wang and J. Gong, *Proposal of a cold-atom realization of quantum maps with Hofstadter's butterfly spectrum*, Physical Review A **77**, 3 031405 (2008).

[42] Y.-J. Lin et al., *Synthetic magnetic fields for ultracold neutral atoms*, Nature **462**, 7273 628–632 (2009).

[43] A. Celi et al., *Synthetic gauge fields in synthetic dimensions*, Physical review letters **112**, 4 043001 (2014).

[44] T. Chalopin et al., *Probing chiral edge dynamics and bulk topology of a synthetic Hall system*, Nature Physics **16**, 10 1017–1021 (2020).

[45] T. Chalopin, *Quantum-enhanced sensing and synthetic Landau levels with ultracold dysprosium atoms*, PhD thesis: Sorbonne Université, 2019.

[46] C. G. Mosander, *XXX. On the new metals, lanthanium and didymium, which are associated with cerium; and on erbium and terbium, new metals associated with yttria*, The London, Edinburgh, and Dublin Philosophical Magazine and Journal of Science **23**, 152 241–254 (1843).

[47] J. Emsley, *Nature's building blocks: an AZ guide to the elements*, Oxford University Press, 2011.

[48] P. M. Becker, A. A. Olsson and J. R. Simpson, *Erbium-doped fiber amplifiers: fundamentals and technology*, Elsevier, 1999.

[49] A. Naji et al., *Review of Erbium-doped fiber amplifier*, International Journal of the Physical Sciences **6**, 20 4674–4689 (2011).

[50] G. Teikemeier and D. J. Goldberg, *Skin resurfacing with the erbium: YAG laser*, Dermatologic surgery **23**, 8 685–687 (1997).

[51] U. Keller and R. Hibst, *Effects of Er: YAG laser in caries treatment: a clinical pilot study*, Lasers in Surgery and Medicine: The Official Journal of the American Society for Laser Medicine and Surgery **20**, 1 32–38 (1997).

[52] A. Frisch, *Dipolar quantum gases of erbium*, PhD thesis: University of Innsbruck, 2014.

[53] https://www.physics.nist.gov/PhysRefData/Handbook/Tables/erbiumtable1.htm, Accessed June 25, 2022.

[54] M. Lu et al., *Strongly dipolar Bose-Einstein condensate of dysprosium*, Physical review letters **107**, 19 190401 (2011).

[55] T. Chalopin et al., *Quantum-enhanced sensing using non-classical spin states of a highly magnetic atom*, Nature communications **9**, 1 1–8 (2018).

[56] E. Lucioni et al., *Dysprosium dipolar Bose-Einstein condensate with broad Feshbach resonances*, Physical Review A **97**, 6 060701 (2018).

[57] M. Rehberger, *Ultracold Erbium Atoms in Far-Detuned Optical Traps - Construction of a Zeeman-Slower*, Master thesis: Rheinische Friedrich-Wilhelms-Universität Bonn, Institut für Angewandte Physik, 2013.

[58] B. G. Wybourne and L. Smentek, *Optical spectroscopy of lanthanides: magnetic and hyperfine interactions*, CRC press, 2007.

[59] Henning Brammer, *Ultrakalte Erbiumatome in einer CO2-Laser Dipolfalle*, PhD thesis: Rheinische Friedrich-Wilhelms-Universität Bonn, Sept. 2016.

[60] J. J. McClelland and J. L. Hanssen, *Laser cooling without repumping: a magneto-optical trap for erbium atoms*, Physical review letters **96**, 14 143005 (2006).

[61] A. Frisch et al., *Narrow-line magneto-optical trap for erbium*, Physical Review A **85**, 5 051401 (2012).

[62] J. Ulitzsch et al., *Bose-Einstein condensation of erbium atoms in a quasielectrostatic optical dipole trap*, Physical Review A **95**, 4 043614 (2017).

[63] J. Lawler, J. Wyart and E. Den Hartog, *Atomic transition probabilities of Er I*, Journal of Physics B: Atomic, Molecular and Optical Physics **43**, 23 235001 (2010).

[64] H. Ban et al., *Laser cooling transitions in atomic erbium*, Optics Express **13**, 8 3185–3195 (2005).

[65] E. Den Hartog, J. Chisholm and J. Lawler, *Radiative lifetimes of neutral erbium*, Journal of Physics B: Atomic, Molecular and Optical Physics **43**, 15 155004 (2010).

[66] K. Aikawa et al., *Bose-Einstein condensation of erbium*, Physical review letters **108**, 21 210401 (2012).

[67] J. Ulitzsch, *Erzeugung eines Bose-Einstein-Kondensats aus Erbiumatomen in einer quasi-elektrostatischen Dipolfalle* (2017).

[68] D. F. Babik, *Bose-Einstein condensation of erbium atoms for fractional quantum Hall physics* (2021).

[69] R. V. Röll, *Ultracold erbium atoms in a quasi-electrostatic optical dipole trap*, Master thesis: Rheinische Friedrich-Wilhelms-Universität Bonn, Institut für Angewandte Physik, 2016.

[70] H. J. Metcalf and P. Van der Straten, *Laser cooling and trapping of neutral atoms*, The Optics Encyclopedia: Basic Foundations and Practical Applications (2007).

[71] C. Pethick and H. Smith, *Bose–Einstein Condensation in Dilute Gases*, Cambridge University Press, 2008, ISBN: 9781139811088.

[72] D. Babik, *Frequency stabilization of a dye laser for narrow-line laser cooling of erbium atoms*, Master thesis: Rheinische Friedrich-Wilhelms-Universität Bonn, Institut für Angewandte Physik, 2014.

[73] T. Lahaye et al., *d-wave collapse and explosion of a dipolar Bose-Einstein condensate*, Physical review letters **101**, 8 080401 (2008).

[74] D. Yoshioka, *The quantum Hall effect*, vol. 133, Springer Science & Business Media, 2002.

[75] D. Tong, *Lectures on the quantum Hall effect*, arXiv preprint arXiv:1606.06687 (2016).

[76] M. V. Berry, *Quantal phase factors accompanying adiabatic changes*, Proceedings of the Royal Society of London. A. Mathematical and Physical Sciences **392**, 1802 45–57 (1984).

[77] D. J. Thouless et al., *Quantized Hall conductance in a two-dimensional periodic potential*, Physical review letters **49**, 6 405 (1982).

[78] R. Bianco and R. Resta, *Mapping topological order in coordinate space*, Physical Review B **84**, 24 241106 (2011).

[79] M. Leder et al., *Real-space imaging of a topologically protected edge state with ultracold atoms in an amplitude-chirped optical lattice*, Nature communications **7**, 1 1–8 (2016).

[80] B. A. Bernevig and S.-C. Zhang, *Quantum spin Hall effect*, Physical review letters **96**, 10 106802 (2006).

[81] Y. Hatsugai, *Chern number and edge states in the integer quantum Hall effect*, Physical review letters **71**, 22 3697 (1993).

[82] R. Ashoori et al., *Edge magnetoplasmons in the time domain*, Physical Review B **45**, 7 3894 (1992).

[83] N. Cooper, J. Dalibard and I. Spielman, *Topological bands for ultracold atoms*, Reviews of modern physics **91**, 1 015005 (2019).

[84] M. Z. Hasan and C. L. Kane, *Colloquium: topological insulators*, Reviews of modern physics **82**, 4 3045 (2010).

[85] J. Dalibard et al., *Colloquium: Artificial gauge potentials for neutral atoms*, Reviews of Modern Physics **83**, 4 1523 (2011).

[86] M. Mancini et al., *Observation of chiral edge states with neutral fermions in synthetic Hall ribbons*, Science **349**, 6255 1510–1513 (2015).

[87] B. Stuhl et al., *Visualizing edge states with an atomic Bose gas in the quantum Hall regime*, Science **349**, 6255 1514–1518 (2015).

[88] Y.-J. Lin, K. Jiménez-García and I. B. Spielman, *Spin–orbit-coupled Bose–Einstein condensates*, Nature **471**, 7336 83–86 (2011).

[89] F. Le Kien, P. Schneeweiss and A. Rauschenbeutel, *Dynamical polarizability of atoms in arbitrary light fields: general theory and application to cesium*, The European Physical Journal D **67**, 5 1–16 (2013).

[90] D. Helten, *Bragg scattering of ultracold erbium atoms off a one-dimensional optical lattice potential*, Master thesis: Universität Bonn, Institut für Angewandte Physik, 2019.

[91] R. Lipert and S. Lee, *Isotope shifts and hyperfine structure of erbium, dysprosium, and gadolinium by atomic-beam diode-laser spectroscopy*, Applied Physics B **57**, 6 373–379 (1993).

[92] A. Savitzky and M. J. Golay, *Smoothing and differentiation of data by simplified least squares procedures.*, Analytical chemistry **36**, 8 1627–1639 (1964).

[93] D. Babik et al., *Synthetic magnetic fields for cold erbium atoms*, Physical Review A **101**, 5 053603 (2020).

[94] A. Martin et al., *Vortices and vortex lattices in quantum ferrofluids*, Journal of Physics: Condensed Matter **29**, 10 103004 (2017).

[95] D. T. Tran, N. R. Cooper and N. Goldman, *Quantized Rabi oscillations and circular dichroism in quantum Hall systems*, Physical Review A **97**, 6 061602 (2018).

[96] C. Repellin and N. Goldman, *Detecting fractional Chern insulators through circular dichroism*, Physical review letters **122**, 16 166801 (2019).

[97] M. F. Maghrebi et al., *Parafermionic zero modes in ultracold bosonic systems*, Physical Review Letters **115**, 6 065301 (2015).